Manipulation of Ga_2O_3 Nanocrystals for the Design of Functional Phosphors

by

Paul Christopher Stanish

A thesis
presented to the University of Waterloo
in fulfilment of the degree of
Doctor of Philosophy
in
Chemistry

Waterloo, Ontario, Canada, 2020

Examining Committee Membership

The following served on the Examining Committee for this thesis. The decision of the Examining Committee is by majority vote.

External Examiner | Jonathan Veinot
Dr.

Supervisor | Pavle V. Radovanovic
Dr.

Internal Member | Vivek Maheshwari
Dr.

Internal Member | Abdelaziz Houmam
Dr.

Internal Member | Eric Prouzet
Dr.

Internal-external Member | Hany Aziz
Dr.

Author Declaration

I hereby declare that I am the sole author of this thesis. This is a true copy of the thesis, including any required final revisions, as accepted by my examiners.

I understand that my thesis may be made electronically available to the public.

Abstract

Transparent conducting oxides are of great interest in semiconductor research and industry. Their ability to carry electricity while remaining transparent allows them to be used for different applications including photovoltaics, lighting, and photocatalysis. Among transparent conducting oxides, Ga_2O_3 has the widest band gap and is characterized by a strong broad-band blue-green afterglow emission, making it attractive for various lighting applications. The main motivation of this thesis is to use these unique properties of Ga_2O_3 to design new phosphors with targeted optical properties. The research described in this thesis specifically focuses on generating white light by non-radiative energy transfer between Ga_2O_3 nanocrystals, as energy donors, and orange-red emitting semiconductor quantum dots, as energy acceptors, and using dopant-induced trap states to extend afterglow emission.

Solution phase conjugation of colloidal nanocrystals allows for short-range energy transfer processes to occur with high probability, which is valuable for sensing and lighting. The first part of this thesis demonstrates the conjugation and electronic coupling of Ga_2O_3 nanocrystals with CdSe/CdS core/shell quantum dots. The introduction of a bifunctional organic ligand to the suspension mixture of these nanocrystals allows for their conjugation. The resulting Förster resonance energy transfer leads to quenching of Ga_2O_3 emission and an increase in the emission of CdSe/CdS quantum dots. As the ratio of CdSe/CdS quantum dots to Ga_2O_3 nanocrystals increases, so does the quenching of Ga_2O_3 emission and the CdSe/CdS photoluminescence intensity. The increase in quenching of Ga_2O_3 emission was successfully modelled assuming a Poisson distribution of CdSe/CdS quantum dots bound to Ga_2O_3 nanocrystals. Owing to the good emission colour complementarity of these materials, white light was observed for optimal nanoconjugate composition.

Next, we demonstrated that the same phenomenon can be achieved without the organic linker by a careful deposition of the colloidal mixture on the glass substrate to remove the empty space between nanocrystals. This approach enables a surface-mediated Förster resonance energy transfer that allows for a design of all-inorganic white light emitting phosphors. The resulting films were highly luminescent and were tuned to give CIE coordinates of 0.31, 0.28.

Gallium oxide also has a long luminescence lifetime, compared to other nanoparticles with similar emission strengths, enabled by its donor-acceptor pair recombination. This phenomenon makes Ga_2O_3 nanocrystals a prime candidate for attempting to design persistent afterglow nanophosphors through doping nanocrystals with selected trivalent rare earth metals. These rare earth elements provide a mechanism for trapping excited free carriers because relaxation within these dopant ions is Laporte forbidden. As a result of doping Ga_2O_3 with Dy^{3+}, the emission of Ga_2O_3 nanocrystals becomes significantly longer at room temperature. More interestingly, the temperature-dependent emission of Ga_2O_3 nanocrystals doped with Dy^{3+} for doping levels between 3 and 13 % increased between 50 K and 200 K, where typical semiconducting nanocrystals show strong quenching. We attribute this anomalous behavior to the carriers trapped in Dy^{3+} excited states, that are thermally reactivated and subsequently relax to Ga_2O_3 native traps states. This assignment was validated by a kinetic Monte Carlo simulation, which was in good agreement with experimental results.

As the importance of luminescence materials, particularly persistent phosphors, increases it is imperative that undergraduate students in chemistry and materials science become familiar with their properties and fabrication. A new laboratory exercise encompassing the combustion synthesis, processing, and characterization of $SrAl_2O_4$:(Eu^{2+}, Dy^{3+}) has been adopted by NE 320L course in the Nanotechnology Engineering program at the University of Waterloo. In this laboratory, students produced crude strontium aluminate containing Eu^{3+} which was subsequently annealed under hydrogen gas, resulting in the red europium emission. This emission becomes green upon reduction of Eu^{3+} to Eu^{2+}. Students performed XRD showing a dramatic increase in crystallinity after annealing, while their SEM measurements did not show a significant change in morphology. Mechanoluminescence was observed using a ballistic setup and found to show a linear dependence on the projectile velocity.

In this thesis I demonstrated the extrinsic (external functionalization) and intrinsic (doping) manipulation of the electronic structure of gallium oxide nanocrystals. The obtained results allow for technological application of the resulting materials (e.g., to generate white light and extend afterglow emission), and provide a framework to enrich upper-year undergraduate curriculum in materials science and nanotechnology.

Acknowledgments

First and foremost, I need to thank my mom and dad for always being there when things got tough. The time that I have spent at the University of Waterloo has been the toughest of my life, and without their consistent support the completion of this thesis would not have been possible. I also need to thank my sister, Clare, for being a good friend and always being willing to share a laugh.

I would like to thank my supervisor, Dr. Pavle Radovanovic, without his leadership, I wouldn't be here today. My committee members, Dr. Eric Prouzet, Dr. Vivek Maheshwari, and Dr. Abdelaziz Houmam, have all provided me with valuable insights and I appreciate them very much. I would also like to thank my external committee members, Dr. Hany Aziz and Dr. Jonathan Veinot for being part of my committee and reading my thesis.

I would also like to thank Dr. Howard Siu for taking a chance when I said that I thought we could make a better experiment for NE 320L. Over the years, Howard has been helpful in all aspects of my life and I feel lucky to have worked with him.

I was blessed with many amazing group members over the course of this PhD, but there are a few that have stood out as most influential to me. I want to extend a very special thank you to Vahid, Arunasish, Matt, Terry, Natalie, Nathaniel, Walker, Mahdieh and Archi for all your help, guidance, and support.

Finally, I would like to thank all the friends that I have made along the way, for everything that they have done to make this thesis possible.

Table of Contents

Table of Figures

List of Abbreviations

CCT	Correlated color temperature
CIE	Commission internationale de l'éclairage associer
CRI	Color rendering index
DAP	Donor acceptor pair recombination
EDX	Energy dispersive X-ray spectroscopy
EXAFS	Extended X-ray absorption fine structure
FRET	Förster resonance energy transfer
LED	Light emitting diode
NC	Nanocrystal
PL	Photoluminescence
PLE	Photoluminescent excitation
QD	Quantum dot
STEM	Scanning transmission electron microscopy
SSL	Solid state lighting
SEM	Scanning electron microscopy
SAED	$SrAl_2O_4:Eu^{2+},Dy^{3+}$
TEM	Transmission electron microscopy
TGA	Thioglycolic acid
THF	Tetrahydrofuran
TOP	n-Trioctylphosphine
TOPO	n-Trioctylphosphine oxide
UV	Ultraviolet
XRD	X-ray diffraction spectroscopy
XANES	X-ray absorption near edge spectroscopy

Chapter 1. Introduction

1.1. Lighting

As the world attempts to reduce its energy consumption and production of greenhouse gasses, improving lighting efficiency is a priority.[1] Lighting has accounted for as much as 19 % of worldwide electricity consumption,[2] however, increasing the efficiency of lighting options with functional materials is seen as an appealing way to curb our usage. There have been many advances in solid state lighting (SSL) because of its versatility compared to traditional light sources.[3] Incandescent light bulbs have very low energy efficiency, while fluorescent light bulbs have reasonable efficiency but produce poor quality of light. This trade-off between efficiency and color quality occurs with both fluorescent lighting and SSL.[4] However SSL devices can now be manufactured to produce light twice as efficiently as fluorescent bulbs.[5,6] Decreasing the lifetime cost to operate lights has the greatest impact on the adoption of new lighting technologies, and this has typically been achieved by increasing luminous efficacy.[1]

1.1.1. Color Space

To be commercially viable, white light emitting devices must produce high color quality. The most intuitive way to visualize this is the 1931 commission internationale de l'éclairage's (CIE) CIE diagram (Figure 1.1), where the outer black line is individual wavelength and colors on the inside can be made by combining light of different wavelengths.[7] The CIE coordinates of a light source can be calculated in two steps:

$$X = \int_\lambda \mathrm{L}_{e,\Omega,\lambda}(\lambda)\bar{x}(\lambda)d\lambda \qquad\qquad 1.1$$

where ($\bar{x}$) is one of three color matching functions (performed for x, y, and z coordinates, with the corresponding spectra shown in Figure 1.2) and ($L_{e,\Omega,\lambda}$) is the emission spectrum of the source. The (x) coordinate in the CIE diagram is the relative (X) contribution:

$$x = \frac{X}{X + Y + Z} \qquad\qquad 1.2$$

On the CIE diagram in Figure 1.1, pure white light is defined with 0.333, 0.333 coordinates, however, our eyes do not have the spectral sensitivity to resolve minute differences in the color of a light source. Humans eyes have adapted to function in light ranging from slightly blue to slightly red, meaning that the socially acceptable range for commercial lighting devices is quite large, generally falling along the Planckian locus (the black curve in Figure 1.1, indicating the chromaticity of black-body radiation).
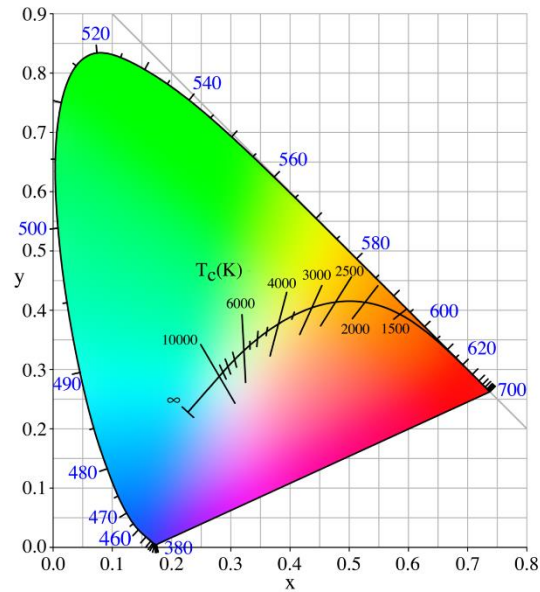
Figure 1.1 CIE 1931 colorimetry diagram, showing single wavelengths (in nm) around the curved boundary and the emission color of idealized Planckian radiators along the line labeled $T_C(K)$.
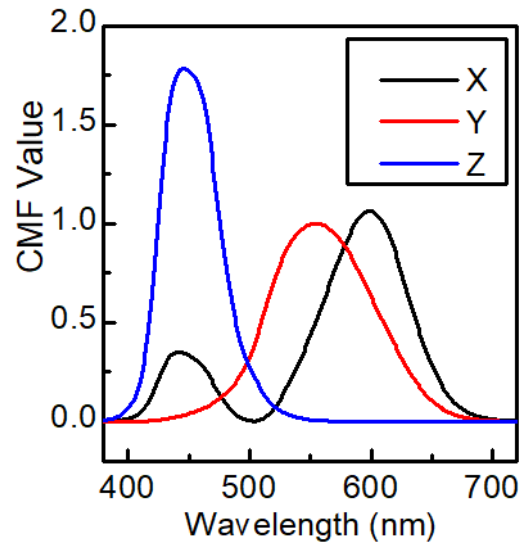
Figure 1.2 CIE 1931 color matching functions for X, Y, and Z.

1.1.2. Correlated Color Temperature

The correlated color temperature (CCT) of a light source is the temperature, measured in Kelvin, of the Planckian radiator (black line in Figure 1.1) with the most similar chromaticity. Not all light sources that are assigned a CCT lie on the Planckian locus, however, the further the chromaticity is from that of black-body emission, the less valuable CCT becomes as a descriptor. Correlated color temperature is commonly referred to in disciplines such as lighting, photography, manufacturing and publishing for its ability to describe the color produced by a light source.[8] A low CCT (2700 K to 3500 K, Figure 1.3 left) light source will appear yellow, a lamp with a high CCT (above 4500 K) will appear blue, while a lamp with a CCT between 3500 K and 4500 K will appear a neutral white (Figure 1.3 right). Lower CCTs have been shown to be more comfortable for humans,[9] while higher CCTs are associated with higher productivity.[10] For these reasons, it is incredibly important to consider CCT in the design of light sources.

Figure 1.3 The same cat illuminated under two different commercial lights with different CCTs. Left: incandescent, CCT ~2700 K. Right: compact fluorescent, CCT ~4100 K.

1.1.3 Color Rendering Index

The color rendering index (CRI) of a light source is a quantitative description of the ability for a light source to faithfully show the color of illuminated objects when compared to an ideal light source. The ideal light source used in the determination of CRI is the black body radiator with the equivalent CCT under 5000 K or a phase of daylight if the CCT of the light source is above 5000 K.[11] The unfaithful display of objects under different light sources with the same chromaticity (shown in Figure 1.4) is caused by the ability of different spectra to have the same chromaticity. When light from one region of the spectrum is present in one light source (e.g., red), but not the other, an observer will only be able to perceive the red in the pigment when illuminated by the light source with red. To determine CRI, the chromaticity of 8 or 12 standards is measured under the illumination of the test and standard light source, and the difference is subtracted from the maximum score of 100. In addition to unfaithful color display, light sources with a low CRI (under 80)[12] cause various negative health effects such as seasonal affective disorder,[13] sleep problems,[14] and depression.[15,16]

Figure 1.4. An example of metamerism. Two panels are shown under three different light sources. Left: daylight with a CCT of 6500 K, middle: an incandescent lamp with a CCT of 2856 K, right: a fluorescent tube light with a CCT of 4100 K.[17]

1.2. Defects in Semiconductors

Using defects to manipulate the properties of materials has been performed since antiquity. Egyptians made brilliantly colored glasses by adding small amounts of transition metals and metallurgists incorporated trace amounts of tin into copper to make an alloy (bronze) with a lower melting temperature, that was much harder.[18] The chemical and physical properties of semiconductors, especially conductivity and carrier lifetime, can be manipulated by the introduction of small amounts of defects such as dopants of vacancies.[19] The research in this thesis makes use of defects, both intrinsic (e.g., oxygen vacancies) and extrinsic (e.g., Dy^{3+}), to design functional materials.

1.2.1. Gallium Oxide

Gallium oxide is a wide bandgap semiconductor (~4.9 eV), which has long been known to have an easily manipulated electronic structure.[20] When synthesized under reducing conditions, Ga_2O_3 NCs will be an intrinsic n-type semiconductor, owing to low lying oxygen vacancies (0.03 - 0.05 eV binding energy),[21,22] giving Ga_2O_3 an anomalously high conductivity for such a large bandgap.[23,24] Thanks to these unique properties, Ga_2O_3 has been studied for applications in spintronics,[25] lighting,[26–28] photodetection,[29] and photocatalysis.[30,31]

In ambient conditions, bulk Ga_2O_3 is stable in β-phase (monoclinic), however, in colloidal NCs under approximately 6 nm metastable γ-phase (cubic) Ga_2O_3 can be synthesized.[24] The cubic phase has a defective spinel structure (shown in Figure 1.5) with 2 Ga^{3+} vacancies per 18 gallium sites.[32] Ga^{3+} can occupy either tetrahedral or octahedral cationic sites, where the relative occupancy of each is governed by the method of preparation and crystal size.[33] At smaller crystallite sizes the likelihood of gallium ions occupying tetrahedral sites is increased.[34] At sizes relevant to this thesis (ca. 5 nm NCs), γ-Ga_2O_3 will have approximately 40 % of its cations in four-coordinate sites.[35] While both tetrahedral and octahedral sites are defective, octahedral sites exhibit more local disorder.[35]
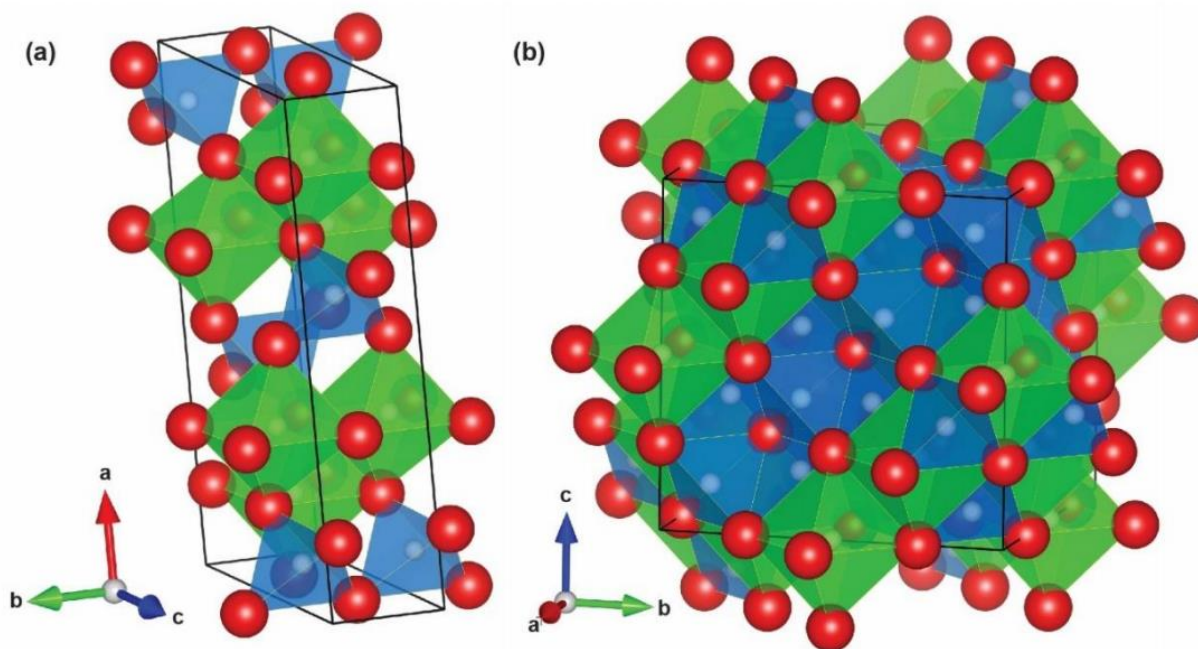
Figure 1.5 Crystal structure of (a) monoclinic Ga_2O_3 and (b) cubic Ga_2O_3. Ga^{3+} and O^{2-} ions are indicated by white and red spheres, respectively. The green and blue polyhedra illustrate six and four coordinated Ga^{3+} sites, respectively.[36]

There have been three different types of emission associated with Ga_2O_3: UV emission from a self-trapped hole,[21] blue emission only observed in conductive samples,[37,38] and green emission that is observed in the presence of a variety of dopants.[21] The blue emission of these γ-Ga_2O_3 NCs was originally asserted to be from a quantum-confined exciton (covered in depth in Chapter 1.3)[39] because of the strong size-dependence of the emission. However, the absorption of these nanoparticles is not accompanied by a blue shift of absorption (and excitation) energies, meaning the bandgap is not size-dependent, proving there is no confinement. Instead, the size-

dependent emission comes from a change in the donor-acceptor trap state separation as a function of particle size.[24,40] The blue emission occurs through a process called donor-acceptor pair recombination (DAP) (schematics shown in Figure 1.6) where an electron and hole will become bound to a donor (oxygen vacancy) and acceptor trapping state (gallium-oxygen vacancy pair), respectively. Given a strong electrostatic interaction, the electron will tunnel from the donor to the acceptor (this is the rate-limiting step), where it will relax and release a visible photon.[21] The energy of the emitted photon (E_{DAP}) can be expressed as:

$$E_{DAP} = E_g - (E_D + E_A) + \frac{e^2}{4\pi\varepsilon r} \pm nE_{phonon} \qquad \text{1.3}$$

where E_g is the bandgap energy, E_D and E_A are binding energies of the donor and acceptor states respectively. The third term represents the electrostatic attraction between two sites (donor and acceptor) with the elementary charge (e) in a material with dielectric constant (ε) separated by a distance (r), and (E_{phonon}) is the energy of phonons involved in radiative transitions.
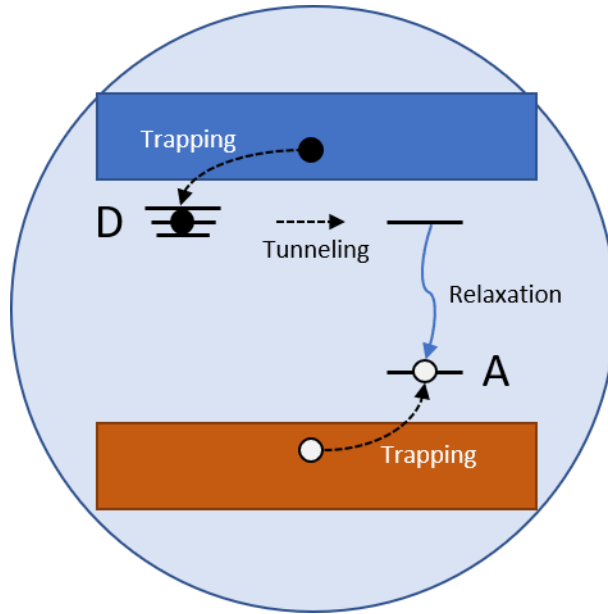
Figure 1.6 Scheme of DAP where excited electrons relax to donor sites (D), holes relax to acceptor sites (A), the electron tunnels from D to an A site where radiative recombination occurs.

There are many donor states per NC, resulting in the formation of a small defect band just below the conduction band.[21] While donor states are simply an oxygen vacancy, acceptor states require an oxygen vacancy and a gallium vacancy adjacent to one another. Since Ga_2O_3 is an n-

type semiconductor, it is common to treat Ga_2O_3 NCs as having a single acceptor with multiple donors.[41,42] Furthermore, the acceptor state is much deeper than the donor state.[21]

The kinetics of this DAP are governed by electron transfer dynamics between the randomly distributed donor and acceptor sites, so the lifetime is non-exponential. The separation between donor states and acceptors states is reduced in smaller Ga_2O_3 NCs resulting in a shorter fluorescence lifetime.[41] The extent of this shortening is described by:

$$W(r) = W_{max} \exp\left(-\frac{2r}{R_D}\right) \qquad 1.4$$

where (W_{max}) is the maximum decay rate which is a constant, and (R_D) is the Bohr radius of the donor.[40] In addition to the distribution of NC sizes, the distribution of donor-acceptor separations within a single nanoparticle means that the lifetime of Ga_2O_3 does not follow an exponential decay.[41]

Multiple studies of Ga_2O_3 lifetimes have reported that defects most likely reside on the surface,[41,42] which is in agreement with equilibrium vacancy concentration;[43] this suggests that NCs are often too small to consistently form defects in their core.[44] Additionally, because of the increased complexity of forming acceptor defects, it is likely that they are highly outnumbered, with as few as a single acceptor per emissive nanoparticle.

1.2.2. Persistent Luminescence

The Chinese have observed persistent luminescence since antiquity, while the Europeans produced the first scientific explanation of persistent luminescence in the 1640.[45] In the 1900s, ZnS doped with Cu, and later co-doped with Co, was used as the persistent luminescent material of choice in many commercial products, but the lifetimes achieved were shorter than desired for many purposes.[46] Strontium aluminate doped with Eu^{2+} had been known to have luminescence comparable to ZnS:Cu,[47] however in 1996 Matsuzawa et al.[48] codoped Eu^{2+}:$SrAl_2O_4$ with Dy^{3+}, allowing it to achieve much higher initial emission intensity, as well as a dramatic increase in lifetime. The co-doping of $Sr_xAl_yO_z$ ushered in a new era of interest in persistent luminescent phosphors.[46]

Despite Eu doped $Ca_XAl_YO_Z$ and $Sr_XAl_YO_Z$ being frequently co-doped with trivalent rare earth metal ions such as Dy^{3+}, Nd^{3+}, and Ce^{3+} to induce long thermoluminescent (TL) lifetimes,[29,48,49] there has been some disagreement about the nature of trap states in these systems. Nevertheless, it is accepted that the main carrier trapped is electrons.[48,50–52] The common quality among all materials that experience persistent luminescence is they are able to stably trap free carriers in excited states only to be freed again through thermal excitation (a schematics for persistent luminescence of $SrAl_2O_4$ is shown in Figure 1.7. based on the Dorenbos model).[53] The rate-limiting step can be from the thermal reactivation of an electron (Dy^{3+} site and process F in Figure 1.7.) or a hole (not shown). In either case, the binding energy of the trap must be overcome by the thermal energy available to the material. Once the carriers are excited back into their respective bands, they must be able to relax radiatively (depicted by Eu^{2+} emission in processes C and H). The rate-limiting step for this process is the thermal excitation of trapped electrons, where the lifetime (τ) can be well described by a modified Arrhenius equation:

$$\tau(T) = s^{-1}e^{-\frac{E_A}{kT}} \qquad\qquad \textit{1.5}$$

where s is the frequency factor or the frequency with which trapped carriers attempt to escape their trapping site, E is the binding energy of the trapping state and kT is the thermal energy. To determine the values of the frequency factor and activation energy under first-order kinetics, one needs to simply perform lifetime analysis at a handful of temperatures and fit with Equation 1.5 using $\ln(\tau)$ vs $1/T$.[54] If the decay is not the first order, the thermoluminescent intensity is measured as the temperature is increased after an excitation and the fit to a model is dependent on the kinetic order of the detrapping.[55]
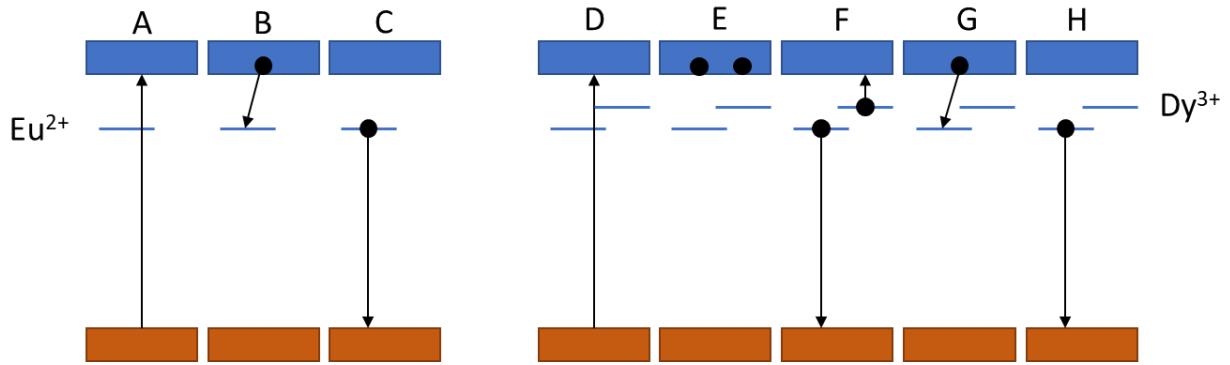
Figure 1.7 The Dorenbos model for the mechanism of Eu^{2+} emission (A-C) in $Sr_2Al_3O_4$ and the mechanism of lifetime extension by way of thermal reactivation (D-H).[53]

Very shallow traps may only hold carriers for a short time, while extremely deep traps require additional heating above room temperature for reactivation to occur.[53,56] Extremely deep traps are ideal for stress sensors or radiation detectors because detrapping events are more likely to occur from physical stress or radiation than ambient conditions.[56,57] The $SrAl_2O_4$:Eu^{2+},Dy^{3+} system is considered to be an ideal phosphor, because of its high quantum yield and intensity.[48]

1.2.3. Thermal Effects in Semiconductors

In a similar way to thermoluminescence, a carrier trapped in an excited state in a luminescent material may be thermally excited to the band edge. In case that the trap is a part of the luminescence mechanism, thermal reactivation of these trapped carriers allows an additional opportunity for non-radiative quenching. As the temperature is increased, the increased quenching behavior becomes more prominent and there is an overall decrease in quantum yield. This is modeled by the following equation:[58]

$$I(T) = \frac{I(0)}{1 - A \exp\left(-\frac{\Delta E}{kT}\right)} \qquad 1.6$$

where A is a preexponential fitting factor and ΔE if the trap depth.

Additionally, the emission of semiconductors is typically red-shifted with increasing temperatures following Varshi's empirical formula:[59]

$$E(T) = E(0) - \frac{\alpha T^2}{\beta + T}$$ *1.7*

where α and β are both constants that describe the shift. The origin of the shift is thought to come from either temperature-dependent lattice dilatations or a shift in the relative position of the conduction and valence band from temperature-dependent electron-lattice interactions.[59]

1.2.4. Dysprosium Emission

Dysprosium can have two strong emissions originating from f-f transitions, one from the electric dipole ($^4F_{9/2}$ - $^6H_{13/2}$) occurring at around 580 nm, and one from the magnetic dipole ($^4F_{9/2}$ - $^6H_{15/2}$) occurring at around 480 nm.[60] Additionally, there are also observable peaks from ($^4F_{9/2}$ - $^6H_{11/2}$) and ($^4F_{9/2}$ - $^6H_{9/2}$) transitions deeper into the red end of the spectrum, however, these transitions are much weaker then the previous two. Being parity forbidden, the electronic dipole emission is much more sensitive to the local environment, meaning that in order to observe emission from the transition, the Dy^{3+} cannot inhabit a centrosymmetric site.[61] In commercial $SrAl_xO_x$, these transitions cannot be observed because the lattice allows the retention of symmetry.[62] However, in Ga_2O_3 the smaller non-symmetric octahedral sites break this symmetry and render these transitions at least partially allowed. As the host lattice of Dy^{3+} distorts the f orbitals more, there is an increase in emission from the electric dipole transition, making it possible to assess local symmetry from the branching ratio of the observed Dy^{3+} peaks.[63]

1.3. Cadmium-Based Quantum Dots

Quantum dots have been an active area of research for many years, with different materials allowing the probing of different regions of the spectrum.[64–67] Quantum dots are of interest in lighting,[68] sensitizing solar cells,[69,70] and biological sensing.[71] They are relatively easy to make and manipulate, while also having amazing tunability across the visible spectrum.[68]

Quantum dots can also be made to have incredibly high QYs, typically achieved by the preparation of core/shell QDs.[72]

Semiconductor NCs smaller than the Bohr radius of its free excitons is called a quantum dot because it effectively exists in 0-dimensions and exhibits strong quantum confinement.[73] The confinement energy of a QD is well described by the particle-in-a-box model,[74] for a QD with a radius R. The bandgap energy of the QD E_G^* is greater than the bandgap energy of the bulk material (E_g).[75,76] The masses of the electron (m_e) and hole (m_h) are treated as the effective mass.

$$E_G^* = E_g + \frac{\hbar^2 \pi^2}{2R^2}\left[\frac{1}{m_e} + \frac{1}{m_h}\right] - \frac{1.8e^2}{\varepsilon R} \qquad 1.8$$

The second term of Equation 1.8 accounts for the particle in a box model used and the third term represents the Coulomb attraction between the free electron and hole.[77] The effective mass approximation breaks down for very small QDs.[77,78] Equation 1.8 is frequently used to determine the size of QDs, however, researchers typically use an empirically derived equation developed by Peng *et al.*[79] to determine the diameter of Cd-based quantum dots (D, in nm) based on the wavelength of the lowest energy absorption maximum (λ, in nm). The equation for CdSe is given as:

$$D = 1.6122 \times 10^{-9} \lambda^4 - 2.6575 \times 10^{-6} \lambda^3$$
$$+ 16242 \times 10^{-3}\lambda^2 - 0.4277\lambda + 41.57 \qquad 1.9$$

The extinction coefficient (ε, in mol·L^{-1}cm^{-1}) of QDs examine by Peng *et. al.* increases proportionally to approximately the power of 3 of the diameter (D, in nm) of a nanoparticle. In the case of CdSe, this relationship is:[79]

$$\varepsilon = 5857D^{2.65} \qquad 1.10$$

Quantum dots have a reduced number of energy levels and are unable to form continuous valence or conduction bands. Instead, their "bands" exist as discrete energy levels with the same center of mass as the bulk, as shown in Figure 1.8.[73,80] For this reason, QDs are often referred to

as artificial atoms.[81] Because of the discrete nature of QD bands, the absorption of the transition between a pair of states appears as a δ-functions. This holds true for the band-edge transition as well as interband transitions from states within the bands, which results in QDs having structured absorption spectra above their bandgap energy, not typically seen in bulk semiconductors.[82] The width of a single QD transition is approximately 5 meV, and if the emission or absorption of a QD is wider than 5 meV it is generally due to the population distribution.[83] Quantum dot emission spectra do not show secondary peaks at high energy because intraband relaxation is a much faster process than interband recombination.[82]
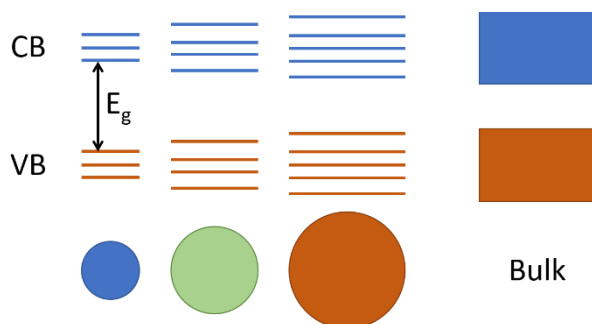
Figure 1.8 Size dependence of semiconductor bandgap.

A QD with a diameter of 5 nm will have ca. 15 % of its atoms on the surface, resulting in a strong surface influence on free carriers in the QD.[84] The surfaces of NCs have a high defect concentration that results in the formation of energy levels that will typically reside within the bandgap and can act as traps. These trap states often lead to nonradiative relaxation, a decrease in conductivity, and oxidation or reduction of the QD.[81,85] To reduce the negative effects of these surface defects, two approaches to passivation have been used. Passivation of the surface can be achieved using organic ligands such as phosphenes, phosphonic acids, and thiols. These ligands are preferred because they can be adsorbed during synthesis, protect the surface, and allow for the colloidal suspension of QDs in a variety of solvents.[72,86] Unfortunately, these organic ligands are larger than individual atoms, and a particular ligand cannot passivate both cations and anions, meaning some dangling bonds will always be present.[81]

Alternatively, passivation can be achieved through the growth of additional layers of a heterogeneous semiconductor, typically with a larger bandgap (band diagrams shown in Figure 1.9).[81] The shell should have the same crystal structure to that of the QD so that its growth does not introduce new defects at the interface.[72] When this condition is satisfied with a material with

a larger bandgap, exciton confinement in the core will be maintained, resulting in a dramatic increase in quantum yield and a small red-shift from strain induced by a lattice mismatch that occurs to a greater degree at larger shell thicknesses.[87] For optimal emission of CdSe-based QDs, the shell should be limited to 2 monolayers[81,87] or additional strain can cause a reduction in efficiency and the emission to be further red-shifted.[87] The simplest and most popular approach is to use smaller elements of the same groups for the shell. In the case of CdSe QDs: ZnS,[88] CdS,[89] and $Zn_{0.5}Cd_{0.5}S$[90] are some of the most common shell compositions, boasting QYs to greater than 0.95.[89]
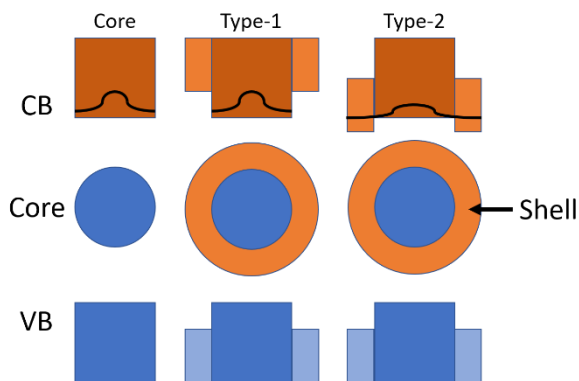
Figure 1.9. Illustration of the core, type-1 core/shell, and type-2 core/shell quantum dots with accompanying band structures and electron wave functions.

A small Stokes' shift is observed in CdSe QDs which increases with the growth of a small shell.[87] Large shells have been observed to create a large Stokes' shift in Type-1 core/shell QDs because a large amount of absorption occurs in the shell, excited carrier then relax in the core, where all of the emission occurs.[91,92] Using QDs with larger shells, it is possible to engineer the absorption spectrum of a QD sample so far as to make the QD appear transparent[93] or to improve spectral overlap for Förster resonance energy transfer.

1.4. Förster Resonance Energy Transfer

Förster resonance energy transfer (FRET) is a nonradiative form of energy transfer that is caused by the interaction of transition dipoles of a donor and an acceptor species.[94] The interaction of dipoles is highly distance dependent, but unlike many other types of quenching, it does not require contact, and can often occur over relatively large distances (5-10 nm), compared

to the chemical bond distance.[95] In order for a FRET donor and acceptor to be compatible, their transitions must occur at similar energies, their transition dipoles must have some level of alignment, and they must be close enough spatially so that their dipoles can interact.[96] FRET has been useful in many of different disciplines because it allows for the measurement of molecular-scale distances based on changes in fluorescence,[97] including the measurement of molecular concentrations,[98] binding interactions[99], and catalytic activity.[100]

The efficiency of FRET (η_{FRET}) between a single donor and acceptor pair separated by a distance R, is modeled by:

$$\eta_{FRET} = \frac{R_0^6}{R_0^6 + R^6} \qquad\qquad 1.11$$

where R_0 is the Förster radius, the separation at which 50 % of energy is transferred from the donor to the acceptor, and can be determined mathematically:

$$R_0 = \sqrt[6]{\frac{9000 \ln 10 \; \kappa^2 Q_D}{128 \; \pi^5 N_{Av} n^4} J(\lambda)} \qquad\qquad 1.12$$

where κ is the alignment between the donor and the acceptor (sometimes referred to as orientation factor), Q_D is the quantum yield of the donor, N_{Av} is Avogadro's number, (n) is the index of refraction of the medium between the donor and acceptor, and $J(\lambda)$ is the spectral overlap integral of the active species (depicted in Figure 1.10). Since η_{FRET} decreases with a sixth power dependence with R_0, $2R_0$ will be considered the limit for the purpose of this thesis, beyond which η_{FRET} is less than 1.5 %.
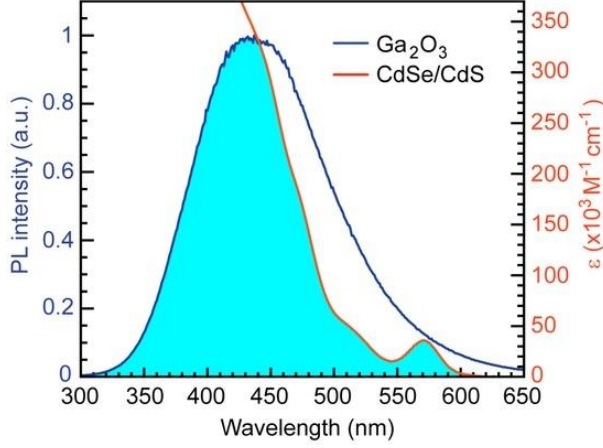
Figure 1.10. Absorption spectrum of CdSe/CdS NCs (orange line) and PL spectrum of Ga₂O₃ NCs (blue line). Shaded area indicates a spectral overlap, as an essential requirement for Förster resonance energy transfer (FRET).

The spectral overlap between donors and acceptors has the biggest impact on R_0 because it can produce the largest magnitude of change. Spectral overlap can be calculated as follows:

$$J(\lambda) = \int_\lambda f_D(\lambda)\varepsilon_A(\lambda)\lambda^4 d\lambda \qquad 1.13$$

where f_D is the donor emission spectrum with the integrated intensity normalized to unity and ε_A is the extinction spectrum of the acceptor.

The alignment of the donor and acceptor transition dipoles is:

$$\kappa^2 = (2\cos\theta_D \cos\theta_A - \sin\theta_D \sin\theta_A \cos\phi)^2 \qquad 1.14$$

where φ is the angle between the two dipoles, θ_D is angle from the midplane to the donor dipole plane, and θ_A is the angle from the midplane to the plane of the acceptor. This notation is shown visually in Figure 1.11. Molecular species that rotate relative to one another at a speed on par with their emission lifetime have essentially random alignment, allowing for an average 2/3 to be used. Larger species, like proteins, that are unable to rotate at the same speed, may have a κ^2 that diverges from 2/3, which can lead to a higher[101] or lower[102] η_{FRET} than would otherwise be expected. Most nanoparticles are large enough that their rotation will be slower than their

fluorescent lifetime, but the assumption that $\kappa^2 = 2/3$ has been shown to hold for species with many possible binding sites and a large degree of symmetry.[103]
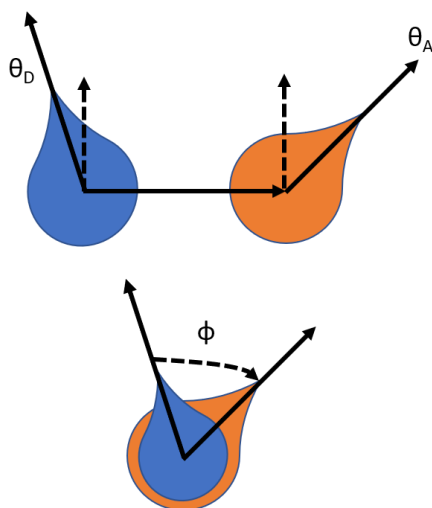
Figure 1.11. A representation of the donor (blue) and acceptor (red) transition dipoles with appropriate notation for determination of κ^2 term using Equation 1.14.

The most reliable method for the determination of η_{FRET} is by lifetime shortening:

$$\eta_{FRET} = 1 - \frac{\tau_{DA}}{\tau_D} \qquad 1.15$$

where (τ_{DA}) and (τ_D) are the lifetimes of the donor with and without an acceptor present, respectively. The rate of energy transfer is given by:

$$k_T(r) = \frac{1}{\tau_D}\left(\frac{R_0}{r}\right)^6 \qquad 1.16$$

FRET occurs on the same time scale as the lifetime of the donor, and contrary to other types of quenching, will not fully quench a fluorophore with an extremely long lifetime, the FRET efficiency only depends on the proximity of acceptors and the Förster radius. If the fluorescent acceptor has longer lifetime than the donor there should be no effect on the acceptor's lifetime, however, if the lifetimes of the donor is longer than the lifetime of the acceptor, the observed lifetime of the acceptor should increase as a result of delayed excitation events

produced by FRET.[26] When the quantum yield of the acceptor is close to 1, the shortening of the donor lifetime can result in FRET complex being more efficient than the donor alone. [104]

When energy is transferred from a donor to an acceptor the emission intensity of the donor is quenched. The extent of this quenching can be used to determine the η_{FRET} from steady-state luminescent data:

$$\eta_{FRET} = 1 - \frac{F_{DA}}{F_D} \qquad 1.17$$

where F_{DA} is the emission of the donor when coupled to the acceptor, and F_D is the emission of the donor alone.[96] If the acceptor is emissive, it is possible to use this same approach to calculate the η_{FRET} from the increase in the acceptor emission by taking the quantum yield of the acceptor into account. In this thesis, η_{FRET} is calculated from quenching of the luminescent lifetime of Ga_2O_3, and the emission increase for CdSe/CdS QDs was used as a qualitative confirmation of the values found using Equation 1.15. In a system with an emissive acceptor, energy received by the acceptor may be emitted. If the donor and acceptor are complementary, they can produce white light solely by exciting the donor, effectively making quasi-single chromophore white light mediated by FRET.[27,105,106]

Original FRET experiments were carried out with molecules that had one binding site,[94] however, NCs have many possible binding sites, and NC films allow the interaction of many acceptors with a single donor. The population of FRET donors of acceptors has been shown to follow a Poisson distribution,[107,108] which can be modeled using a modified form of Equation 1.11:

$$\eta(\xi, R) = \sum_{n=0}^{\infty} \frac{\xi^n e^{-\xi}}{n!} \left(\frac{nR_0^6}{R_{DA}^6 + nR_0^6} \right) \qquad 1.18$$

where ξ is the average number of acceptors per donor, and (n) is the whole number of acceptors a specific donor can interact with.

Confirming the presence of FRET requires an agreement between all observable methods of quantification. In the case of two emissive nanocrystals, this means that we are looking for a decrease in donor emission, an increase in acceptor emission, a shortening of the donor lifetime.

1.5. Purpose and Scope of Thesis

The main motivation of the research discussed in this thesis is to manipulate the unique properties of Ga_2O_3 to design new phosphors with targeted optical properties for potential lighting applications, and the design of a new class of persistent luminescent phosphors of reduced dimensions.

In Chapter 2, colloidal Ga_2O_3 NCs were used as a blue source and attached to CdSe/CdS QDs using an organic linker. Functionalization allowed for FRET to excite the QDs, activating a new single white-light-emitting nanoconjugate. Emissive properties were measured to determine the efficiency of the energy transfer and to demonstrate the good chromaticity achieved with this approach.

In Chapter 3, Ga_2O_3 was co-deposited on a substrate with CdSe/CdS QDs, and FRET was observed. The deposition simplified the approach used in Chapter 2 and allowed for producing a brighter sample. It was shown that this hybrid nanoparticle approach allowed the generation of single-fluorophore white light.

In Chapter 4, colloidal Ga_2O_3 NCs were doped with Dy^{3+}. Dysprosium is believed to occupy octahedral sites on the surface of Ga_2O_3 NCs. The introduction of Dy^{3+} resulted in the extension of the room temperature fluorescent lifetime of Ga_2O_3 NCs as well as an increase in luminescent intensity between 50 K and 200 K. These results provide a guidline for the design of afterglow phosphor in reduced dimensions.

In Chapter 5, we applied the expertise gained in other sections of this thesis to create an upper-level undergraduate lab experiment. In this experiment, students used combustion synthesis to create $SrAl_2O_4$ particles doped with Eu^{3+} and Dy^{3+}. The students then anneal the particles resulting in a green luminescence from newly reduced Eu^{2+}, and a prolonged luminescence when the excitation source is removed. Students then performed SEM and XRD

measurements, which confirmed the synthesis and morphology of $SrAl_2O_4$. Finally, students measured the mechanoluminescence of their samples with a ballistic apparatus and observed a linear dependence between mechanoluminescence and the impact velocity of a projectile.

Chapter 2. Energy Transfer between Conjugated Colloidal Ga$_2$O$_3$ and CdSe/CdS Core/Shell Nanocrystals for White Light Emitting Applications[1]

Developing solid state materials capable of generating homogeneous white light in an energy efficient and resource-sustainable way is central to the design of new and improved devices for various lighting applications. Most currently-used phosphors depend on strategically important rare earth elements, and rely on a multicomponent approach, which produces sub-optimal quality white light. Here, we report the design and preparation of a colloidal white-light emitting nanocrystal conjugate. This conjugate is obtained by linking colloidal Ga$_2$O$_3$ and II–VI nanocrystals in the solution phase with a short bifunctional organic molecule (thioglycolic acid). The two types of nanocrystals are electronically coupled by Förster resonance energy transfer owing to the short separation between Ga$_2$O$_3$ (energy donor) and core/shell CdSe/CdS (energy acceptor) nanocrystals, and the spectral overlap between the photoluminescence of the donor and the absorption of the acceptor. Using steady state and time-resolved photoluminescence spectroscopies, we quantified the contribution of the energy transfer to the photoluminescence spectral power distribution and the corresponding chromaticity of this nanocrystal conjugate. Quantitative understanding of this new system allows for tuning of the emission color and the design of quasi-single white light-emitting inorganic phosphors without the use of rare-earth elements.

2.1. Introduction

Colloidal nanocrystals (NCs) offer a substantial promise for the design and fabrication of solid state structures and devices. Size-tunable electronic structure and optical properties render this class of materials attractive for various applications in photonics, optoelectronics, and

---

[1] The results of this chapter have been published:
Reprint (adapted) under the Creative Common Attribution 4.0 Licence from (**Stanish, P**.; Radovanovic, P. Energy Transfer between Conjugated Colloidal Ga$_2$O$_3$ and CdSe/CdS Core/Shell Nanocrystals for White Light Emitting Applications. *Nanomaterials* **2016**, *6*, 32). Copyright 2016 MDPI (Basel, Switzerland) *Unless otherwise stated, all of the work reported in this chapter was performed and analyzed by the candidate.*

sensors.[109] The size and shape of colloidal NCs can be controlled in situ by adjusting the synthesis conditions,[110] allowing for the exploitation of quantum confinement to manipulate their optical properties. Furthermore, colloidal NCs can be modified post-synthetically by functionalization and conjugation with organic or biomolecules,[111] or by forming a composite with polymers or other nanostructures.[112,113] This ability to combine solid state-like optical and mechanical properties of NCs with the opportunities for their chemical modifications in solution opens a number of possibilities to use them as building blocks in optical and photonic devices.

With increasing concerns about the global energy supply and sustainable use of natural resources, the search for new low-cost materials for energy efficient lighting has intensified in recent years.[114] The total amount of electrical energy used for lighting is near 20% at the global level, with residential and commercial sectors being responsible for the majority of lighting electricity consumption.[115] Light-emitting diodes (LEDs) have emerged as a long-term alternative to traditional incandescent light bulbs, owing to their efficiency, durability, and reliability.[116] The most promising approach to white LEDs has been to combine GaN blue LED with remote phosphors, most notably yellow-emitting yttrium aluminum garnet doped with cerium (Ce:YAG).[117] However, the adoption of such white LEDs for general lighting applications has been rather slow because of the high manufacturing cost, and non-optimal characteristics of light (low color rendering index and high correlated color temperature).[118] The deficiencies of the spectral properties have been addressed by the addition of other rare earth element-based phosphors to augment the spectral density in the red region of the spectrum,[119,120] further increasing the complexity and cost of the final devices and making it difficult to obtain homogeneous white light in a reproducible manner. Colloidal II–VI NCs with selected average sizes have also been used in combination with remote phosphors to generate 'warm' white light.[121]

We have recently demonstrated the ability to produce white light and tune its chromaticity by conjugating transparent metal oxide NCs with organic fluorophores (dyes) emitting in the complementary spectral range.[27,105] The core of this phenomenon is a defect-based photoluminescence of these metal oxide NCs. In the case of colloidal γ-Ga_2O_3 NCs the emission is based on electron donor-acceptor pair (DAP) recombination.[24] It arises from the recombination of an electron trapped on an oxygen vacancy forming localized electron donor

states with a hole trapped on a gallium–oxygen vacancy pair acting as an electron acceptor.[122,123] A range of distances between electron donor and acceptor sites, as well as coupling of the electronic transition with lattice phonons are likely reasons for significant broadening of this emission band.[122,124] Owing to the proximity of the NC surface-bound organic fluorophore to the DAP recombination sites, and the overlap of its absorption spectrum with the DAP photoluminescence (PL) band, the photoexcited Ga_2O_3 NCs can transfer the excitation energy to the conjugated dye molecules via the Förster resonance energy transfer (FRET) mechanism.[106] This approach has allowed us to obtain a hybrid nanoconjugate acting as a single white light-emitting fluorophore.[119,120]

In this work, we demonstrate the design and preparation of new colloidal white light-emitting nanocomposite obtained by controlled conjugation of II–VI and γ-Ga_2O_3 NCs using a simple molecular linker. The ability to manipulate the PL spectra of CdSe/CdS (core/shell) NCs by changing the core size and/or shell thickness allows for fine tuning of the red side of the nanocomposite emission to generate white light with the desired chromaticity. The spectral overlap between the PL of the energy donor (Ga_2O_3 NCs) and the absorption of the energy acceptor (core/shell CdSe/CdS NCs) enables their electronic coupling by FRET. Using the PL quenching of the energy donor determined from the steady-state and time-resolved PL measurements, we quantified the contributions of the direct excitation and energy transfer to the emission of CdSe/CdS NCs. The nanocomposite demonstrated in this work represents an important step toward single-phased all-inorganic rare earth element-free white light-emitting phosphor.

2.2. Materials and Methods

2.2.1. Materials

All materials are commercially available, and were used as received. Gallium acetylacetonate ($Ga(acac)_3$ 99.99 %) was purchased from Strem Chemicals (Newburyport, MA, USA). Cadmium oxide (99.99 %), selenium (99.99 %), dodecanethiol (98 %), 1-octadecene (90 %), trioctylphosphine (TOP), oleylamine (70 %), oleic acid (OA, 90 %), thioglycolic acid (TGA), trioctylphospine oxide (TOPO, 90 %), tetradecylphosphonic acid (97 %), and tetrahydrofuran (THF, 90 %) were all purchased from Sigma Aldrich (St. Louis, MO, USA).

2.2.2. Synthesis of Ga₂O₃ NCs

The synthesis of Ga_2O_3 NCs was carried out according to previously reported method.[24] Briefly, 0.5 g of Ga(acac)₃ and 14 g of oleylamine were loaded into a 100 mL three-neck round bottom flask. The reaction flask was filled with argon and heated to 300 °C over the course of an hour. The reaction mixture was held at this temperature for an hour, and then the heating mantle was and the was left to cool to room temperature. The obtained product was suspended in 20 mL of ethanol and centrifuged at 3000 rpm. The washing procedure was repeated three more times. The NCs were finally capped with TOPO, as previously described.[24] The capped NCs were dispersed in THF.

2.2.3. Synthesis of CdSe NCs

The synthesis of CdSe QDs was carried out according to previously reported method.[125] CdO (60 mg), tetradecylphosphonic acid (210 mg), and TOPO (3 g) were combined in a 100 mL three-neck round bottom flask. The flask was degassed at 150 °C for 1 h, then back filled with argon. The reaction mixture was brought to 320 °C and 1 mL of TOP-Se, prepared separately by dissolving 60 mg Se in 1 mL TOP, was injected rapidly. The reaction was allowed to proceed until the desired NC size is achieved, then cooled using compressed air. When the temperature reached 80 °C methanol was injected, and the precipitated NCs were isolated by centrifugation at 3000 rpm. The NCs were then dispersed in hexane, and their concentration was determined from the absorption spectra.[79]

2.2.4. CdS Shell Growth

The growth of CdS shell was performed by a previously reported method.[89] In summary, as-synthesized suspension of CdSe NC cores (ca. 100 nmol) was placed in a three-neck round bottom flask containing 3 mL oleylamine and 3 mL 1-octadecene. The reaction flask was held under vacuum for 1 h and subsequently purged with nitrogen. The shell was grown from cadmium oleate and dodecanethiol as precursors. Cd(OA)₂ was prepared by dissolving 1 part CdO in 4 parts oleic acid at 230 °C, while dodecanethiol was dissolved in 1-octadecene. The temperature of the flask containing NC cores was increased to 320 °C, and the dropwise injection of 6 mL Cd(OA)₂ and dodecanethiol solutions started at 240 °C. The addition was carried out for 3 h, after which 3 mL of oleic acid was injected and the colloidal mixture was further heated for

1 h. The reaction mixture was cooled, suspended in acetone, centrifuged at 3000 rpm and the precipitate was dissolved in THF.

2.2.5. Functionalization of CdSe/CdS NCs with TGA

The capping of CdSe/CdS NCs with TGA was carried out by combining 1 mL of 5 µM CdSe/CdS NCs in hexanes, 1 mL acetone, and 0.2 mL TGA in a 25 mL scintillator vial under a nitrogen atmosphere, and stirring for 30 min. 0.5 mL ethanol was added to the vial and the mixture was stirred for another 15 min. The product was isolated by centrifuging at 3000 rpm. The precipitate was washed again in ethanol, and the supernatant liquid was collected. This process was repeated once more, and the resulting TGA-capped NCs were dispersed in THF. The amount of unbound TGA linker in the supernatant was determined by absorption spectroscopy, using a calibration curve established by measuring the absorbance of TGA solutions of known concentrations.

2.2.6. Preparation of the Nanoconjugate

One milliliter of stock suspension (4.45 µM) of Ga_2O_3 NCs in THF was placed in a 25 mL vial. Varying amounts of TGA-bound CdSe/CdS NCs (0.2, 0.4, 0.6, 0.8, and 1.0 mL stock suspension) were added to these vials, and the mixture was diluted with additional THF to the final volume of 2 mL. These suspensions were left for 4 h and then characterized spectroscopically.

2.2.7. Spectroscopic Measurements

Absorption spectroscopy measurements were performed with a Varian Cary 5000 UV-vis-NIR spectrophotometer (Agilent Technologies, Santa Clara, CA, USA) using standard 1 cm path length quartz cuvettes, 1 nm bandpass, scanning at 120 nm/min. Photoluminescence spectra were collected with a Varian Cary Eclipse fluorescence spectrometer with 5 nm excitation and emission bandpass, and λ_{ex} = 250 nm. Time-resolved PL measurements were performed with a Horiba Jobin Yvon iHR320 time-correlated single photon counting spectrometer (Edison, NJ, USA) using a 249 nm NanoLED and a Horiba Jobin Yvon TBX picosecond detector.

2.2.8. Nanocrystal Characterization

The phase of Ga_2O_3 NC was determined by X-ray diffraction (XRD) measurements. XRD patterns were collected with an INEL powder diffractometer featuring a position-sensitive detector and copper Kα source ($\lambda = 1.5418$ Å).

Size, morphology, and composition of the NCs were determined using JEOL-2010F transmission electron microscope operating at 200 kV. The specimens for transmission electron microscopy (TEM) imaging were prepared by dropping a hexane suspension of NCs on a copper grid containing carbon support film (Ted Pella, Inc). Energy dispersive X-ray spectroscopy (EDX) was used to map Ga and Cd.

2.3. Results and Discussion

The average size and morphology of colloidal Ga_2O_3 NCs used in this study were determined by transmission electron microscopy (TEM). The NCs are generally quasi-spherical and have an average diameter of ca. 5.5 nm (Figure 2.1a). The X-ray diffraction (XRD) pattern confirms that these NCs exhibit cubic crystal structure characteristic for the γ-Ga_2O_3 (Figure 2.1b). We chose CdSe/CdS core/shell NCs as a complementary solid-state emitter because they possess a strong size-tunable red emission, which could allow for the generation of white light when coupled with the Ga_2O_3 DAP PL. A typical TEM image of CdSe/CdS NCs is shown in Figure 2.1c. As-synthesized CdSe NC cores have an average size of ca. 2.2 nm, as determined from the band gap absorption energy.[79] From the comparison of the average NC sizes before and after the shell growth, the average thickness of the shell was estimated to be ca. 2.3 nm, consistent with the core/shell NCs prepared under similar conditions.[89] These estimates were confirmed using the corresponding band edge absorption energy (Figure 2.1d).

Phase and purity of $Dy^{3+}:Ga_2O_3$ NC products were confirmed by X-ray diffraction (XRD) measurements. XRD patterns were collected with an INEL powder diffractometer featuring a position-sensitive detector and copper Kα source (λ = 1.5418 Å).

Size, morphology, and composition of the NCs were determined using JEOL-2010F transmission electron microscope operating at 200 kV. The specimens for transmission electron microscopy (TEM) imaging were prepared by dropping a hexane suspension of NCs on a copper grid containing carbon support film (Ted Pella, Inc). Energy dispersive X-ray spectroscopy (EDX) was used to characterize the elemental composition of the samples.

Figure 2.1. (a) Overview transmission electron microscopy (TEM) image of γ-Ga₂O₃ nanocrystals (NCs) having an average dimeter of ca. 5.5 nm; (b) X-ray diffraction (XRD) pattern of the same NCs; vertical black lines represent a reference XRD pattern of bulk γ-phase Ga₂O₃; (c) Overview TEM image of ca. 6.8 nm CdSe/CdS core/shell NCs; (d) Absorption (red) and photoluminescence (PL) (blue) spectra of CdSe/CdS NCs (solid lines), and the absorption spectrum of the corresponding CdSe NC cores (red dashed line).

To facilitate the conjugation of Ga_2O_3 and CdSe/CdS NCs we used thioglycolic acid (TGA), which can bind to NC surfaces through both thiol and carboxylic acid functional groups.[126] Thiols are known to bind strongly to the CdSe or CdS quantum dot surfaces,[127,128] and in our previous studies we showed that carboxylic acid group reacts with the surface of Ga_2O_3 NCs.[105,106] An overview TEM image of the CdSe/CdS-conjugated γ-Ga_2O_3 NCs is shown in Figure 2.2a. There was no segregation observed between Ga_2O_3 NCs and CdSe/CdS Qds. Figure 2.2b shows a high-resolution TEM image of conjugated NC, these nanocrystals aggregated and were identified by measuring their lattice spacing. The close proximity of Ga_2O_3 and CdSe/CdS NCs shown in Figure 2.2b indicates that there is no mutual NC segregation and suggests that the two types of NCs may be conjugated. To determine the overall homogeneity of the colloidal NC conjugate we performed energy-dispersive X-ray spectroscopy (EDX) elemental mapping in the scanning transmission electron microscopy (STEM) mode. A STEM image and the corresponding maps of Ga and Cd are shown in Figure 2.2c–e, respectively. The Ga and Cd maps are well correlated, indicating homogeneous distribution of both types of NCs within the aggregate.

CdSe/CdS NCs are excellent FRET acceptors because their absorption spectrum strongly overlaps with the emission spectrum of Ga_2O_3 NCs (Figure 2.3), providing a basis for the FRET mechanism. Furthermore, the quantum yield of these NCs is very high, in some cases reaching over 90%.[129] The spectral overlap is calculated as:

$$J(\lambda) = \int_0^\infty F_D(\lambda)\varepsilon_A(\lambda)\lambda^2 d\lambda \qquad 2.1$$

where ($F_D(\lambda)$) is the emission of the FRET donor with an integrated intensity normalized to unity, and ($\varepsilon_A(\lambda)$) is the molar extinction coefficient of the acceptor at wavelength λ. Spectral overlap is the key parameter determining the critical radius (R_0), also known as the Förster radius, which is defined as the separation at which the energy transfer efficiency is 50%.

$$R_0 = \left(\frac{9000(\log 10)\kappa^2 Q_0}{128\pi^5 N_A n_T^4} J(\lambda)\right)^{\frac{1}{6}} \qquad 2.2$$

In this expression (Q_0) is the donor quantum yield in absence of the acceptor, (n_T) is the index of refraction of the solvent, N_A is the Avogadro's number and (κ^2) is the dipole alignment factor which we define as 2/3. This value is appropriate when donor and acceptor dipole orientations are random and experience no ordering.[103,106,130] In the case of Ga_2O_3 and CdSe/CdS NCs, the Förster radius was calculated to be 7.13 nm. In order to observe FRET in colloidal suspension, Ga_2O_3 and CdSe/CdS NCs must be within 21.4 nm ($3R_0$). This distance is much smaller than the average separation of free standing NCs in solution phase, which was estimated to be over 250 nm even for the highest NC concentrations used. To induce FRET in solution, the NCs were conjugated with a bifunctional TGA linker, as described in the Experimental Section. Based on the TEM images, the average sizes of Ga_2O_3 and CdSe/CdS NCs are ca. 5.5 and 6.8 nm, respectively. Assuming the length of TGA of 0.5 nm, the center-to-center separation between NCs should be ca. 6.7 nm, well within the limit of 21.4 nm.
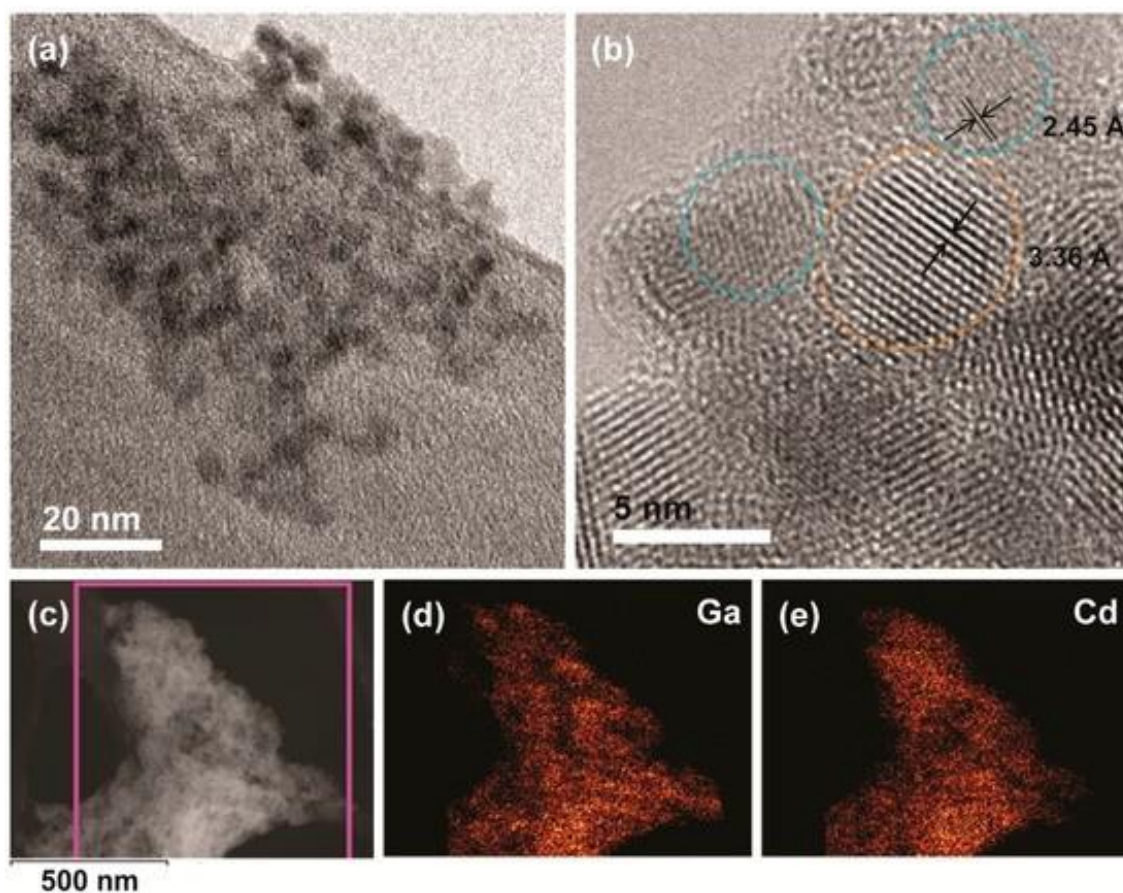
Figure 2.2. (a) TEM image of a cluster of Ga_2O_3-CdSe/CdS NC conjugate obtained using NCs shown in Figure 2.1; (b) High resolution TEM image of the same sample. Orange and blue circles indicate CdSe/CdS and Ga_2O_3 NCs, respectively; the lattice spacings shown correspond to {002} and {311} planes

of CdS and Ga₂O₃, respectively; (c–e) Scanning transmission electron microscopy (STEM) image of the nanocrystal conjugate (c); and the corresponding Ga (d) and Cd (e) energy-dispersive X-ray spectroscopy (EDX) elemental maps.
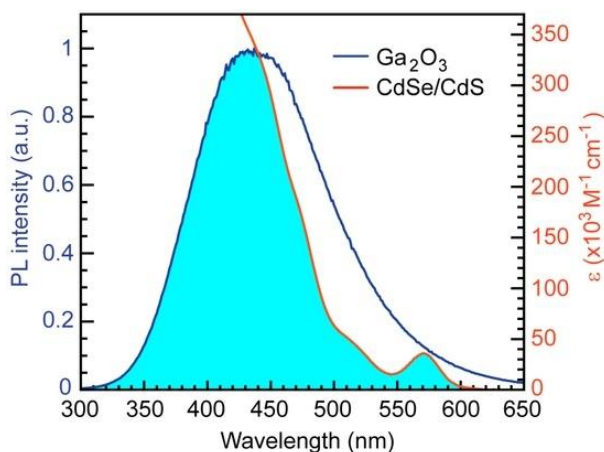
Figure 2.3. Absorption spectrum of CdSe/CdS NCs (orange line) and PL spectrum of Ga₂O₃ NCs (blue line). Excitation wavelength for Ga₂O₃ NCs is 250 nm. Shaded area indicates a spectral overlap, as an essential requirement for Förster resonance energy transfer (FRET).

Figure 2.4a shows PL spectra of Ga₂O₃-CdSe/CdS NC conjugates having different CdSe/CdS to Ga₂O₃ NC concentration ratio, upon excitation at 250 nm (corresponding to the Ga₂O₃ band edge). The concentration of CdSe NC cores was determined from the absorption spectrum using the extinction coefficient (ε) value reported for the samples prepared under similar conditions,[79] which allowed us to estimate the concentration of CdSe/CdS NCs as FRET acceptors by assuming quantitative extraction and uniform coating of the cores with CdS shell. The relative concentrations of Ga₂O₃ NCs in the conjugate samples were inferred from EDX elemental analysis, accounting for an average NC volume. The emission intensity of Ga₂O₃ NCs is quenched up to ca. 40% concurrently with an increase in CdSe/CdS NC emission. Deconvoluted spectra of CdSe/CdS NCs in the nanocrystal conjugates are shown in Figure A.1 (Supplementary Materials). This observation is consistent with the FRET coupling of the two components. However, CdSe/CdS NCs also emit light upon excitation at 250 nm. The PL spectra of CdSe/CdS NCs, treated exactly as in the preparation of NC conjugates but without Ga₂O₃ NCs, are shown with dashed lines in Figure 2.4a. Higher PL intensity of CdSe/CdS NCs in the conjugated form attests to FRET between Ga₂O₃ and CdSe/CdS NCs (Figure A.1, Supplementary Materials). In contrast to the NC conjugate, a suspension containing the same concentrations of Ga₂O₃ and CdSe/CdS NCs without the linker exhibits only about a 10% decrease in Ga₂O₃ DAP emission intensity (Figure 2.4b). This reduction in the DAP emission

occurs because of the direct excitation of CdSe/CdS NCs by a fraction of the excitation source, and is an unavoidable phenomenon when studying FRET between nanoparticles. Similarly, a solution containing Ga_2O_3 NCs and the relevant amount of TGA linker (vide infra) leads to only a 7.5% reduction in the DAP emission. To determine the concentration of TGA bound to the surface of CdSe/CdS NCs, the absorbance of TGA in the supernatant obtained upon precipitation of TGA-bound NCs was measured. After the initial wash ca. 94.5% of TGA remained in the supernatant. Additional washing resulted in further removal of the TGA loosely adsorbed on the NC surfaces, suggesting that only ca. 0.3% of the original amount of TGA is actually bound to CdSe/CdS NCs. Hereafter, the concentration of TGA is given in terms of the equivalents of CdSe/CdS NCs added to Ga_2O_3 NCs (i.e., the amount of TGA corresponding to certain acceptor to donor concentration ratio). It is evident that some of the reduction in Ga_2O_3 PL intensity also comes from competitive light absorption and/or quenching by the TGA linker (Figure A.2, Supplementary Materials), but the extent to which Ga_2O_3 NC emission is quenched by energy transfer is far greater (Figure 2.4c). The existence of FRET is also evident from the excitation spectrum of CdSe/CdS acceptor in the NC conjugate (Figure A.3, Supplementary Materials).
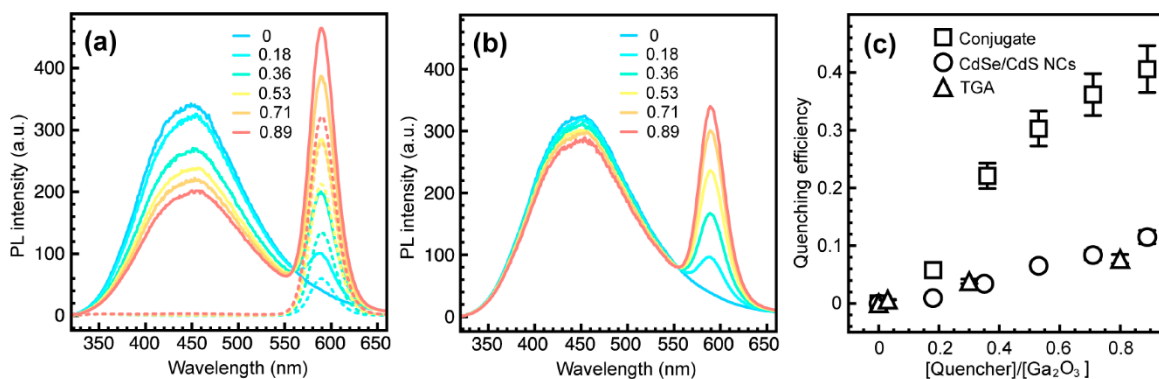
Figure 2.4. (a) PL spectra of colloidal Ga_2O_3-CdSe/CdS NC conjugates (solid lines) having different CdSe/CdS to Ga_2O_3 NC concentration ratio, as indicated in the graph. PL spectra of thioglycolic acid (TGA)-bound CdSe/CdS NC suspensions having the same concentration as in the NC conjugate are shown with dashed lines (λexc = 250 nm); (b) PL spectra of the mixtures of Ga_2O_3 and CdSe/CdS NCs prepared in the same way as the NC conjugate but without the TGA linker; (c) Quenching efficiency of the donor-acceptor pair (DAP) emission of Ga_2O_3 NCs in the conjugate (squares), mixed with CdSe/CdS NCs (circles), and mixed with TGA but without CdSe/CdS NCs (triangles).

The energy transfer efficiency is defined by the Förster theory as:

$$\eta = \frac{nR_0^6}{nR_0^6 + nR_{DA}^6} \qquad\qquad 2.3$$

31

where (R_{DA}) is the average separation between donors and acceptors, and n is the acceptor to donor ratio. FRET efficiency (η) can also be determined experimentally by measuring the donor lifetime shortening in the presence of the acceptors:

$$\eta = 1 - \frac{\tau_{DA}}{\tau_D} \qquad\qquad 2.4$$

where (τ_D) and (τ_{DA}) are the lifetimes of the donor alone and in the presence of the acceptors, respectively. Since DAP emission does not follow a simple exponential time decay,[41] the integrated lifetimes were used to calculate η, instead of the time components obtained as the fitting parameters. The ligands bound to the Ga_2O_3 NC surface can compete with native defects for trapping of the photogenerated free carriers.[24] Therefore, the DAP emission can also be affected by the molecules bound to the surface of the NCs. When TGA replaces TOPO on Ga_2O_3 NCs in the amount equivalent to that used to conjugate CdSe/CdS NCs, the DAP emission experiences a negligible reduction in lifetime (Figure 2.5a). The original DAP PL lifetime is decreased by maximum of ca. 3% for the amount of TGA corresponding to the highest CdSe/CdS to Ga_2O_3 NC ratio explored in this study (aqua blue trace). On the other hand, Figure 2.4b shows progressive shortening of the Ga_2O_3 NC PL lifetime with increasing concentration of TGA-bound CdSe/CdS NCs, confirming that FRET is the dominant quenching mechanism. Figure 2.5c compares the quenching efficiency (η) of Ga_2O_3 NCs conjugated with CdSe/CdS NCs via TGA with that of Ga_2O_3 NCs capped with TGA, for different concentrations of the corresponding quencher, calculated using Equation 2.4. CdSe/CdS-conjugated Ga_2O_3 NCs show significantly higher efficiency for all quencher concentrations confirming the FRET from Ga_2O_3 donor to CdSe/CdS acceptor NCs.
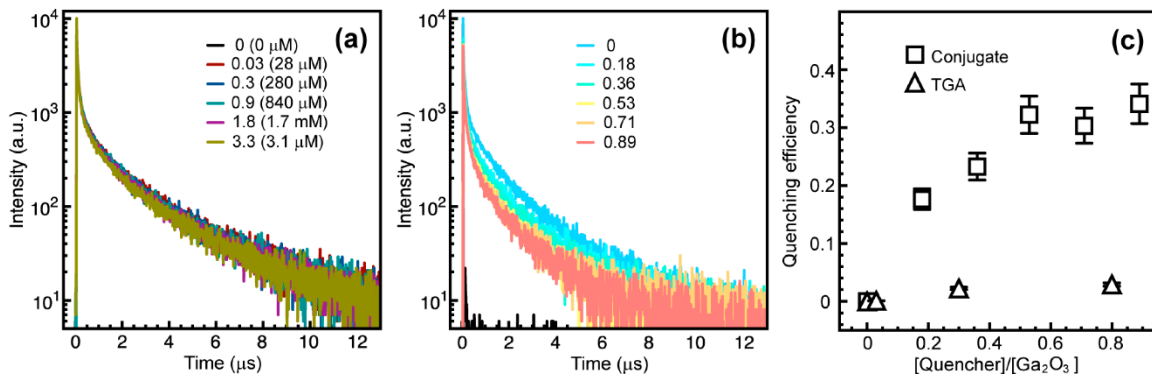
Figure 2.5. (a) Time-resolved DAP PL decay of Ga₂O₃ NCs containing different amounts of surface-bound TGA without CdSe/CdS NCs. TGA equivalents and absolute concentrations (in parentheses) in Ga₂O₃ NC suspensions are indicated in the graph (aqua blue trace (0.84 mM) represents TGA concentration for the highest acceptor to donor ratio); (b) Time-resolved DAP PL decay of Ga₂O₃ NCs in the NC conjugates having different CdSe/CdS to Ga₂O₃ NC concentration ratio, as indicated in the graph; (c) Quenching efficiency of the DAP PL of Ga₂O₃ NCs in the NC conjugate (squares) and with bound TGA (triangles).

Förster resonance energy transfer efficiency between Ga₂O₃ and CdSe/CdS NCs, calculated using Equation 2.4, was corrected for possible quenching of the donor emission by TGA (triangle symbols in Figure 5c), and displayed in Figure 2.6 as a function of the acceptor to donor ratio (n). The acceptor to donor ratio was determined to be 0.9 when 1 mL of CdSe/CdS NC suspension (the largest amount) was added to 1 mL of Ga₂O₃ NC stock suspension. The expression for FRET efficiency (Equation 2.3) is an average approximation when the majority of binding sites are occupied or the stoichiometric ratio of the donor and acceptor can be controlled.[103,106,131] The colloidal NCs generally have a large surface area, leading to a large number of possible binding sites, some of which are unoccupied, invalidating this basic model. Instead, the distribution of the acceptors per donor will obey Poissonian statistical model when most binding sites are unoccupied:[107,108]

$$\eta(\xi, R) = \sum_{n=0}^{\infty} \frac{\xi^n e^{-\xi}}{n!} \left[\frac{nR_0^6}{R_{DA}^6 + nR_0^6} \right] \qquad 2.5$$

where (ξ) is an average number of acceptors per donor, while n is a whole-number acceptor to donor ratio. The FRET efficiency data in Figure 2.6 were fit using Equation 2.5 (dashed line). The fit is of a reasonable quality, with an R^2 value of 0.87. The Poissonian fit in Figure 2.6 is

distinctly different from the energy transfer efficiency predicted by the Förster theory (Equation 2.3) using the R_0 and R_{DA} values of 7.13 and 6.7 nm, respectively (solid line).

The ability to control FRET efficiency in Ga_2O_3-CdSe/CdS NC conjugates by adjusting the acceptor to donor ratio can be used to control the overall chromaticity of the emitted light. Figure 2.7 shows an International Commission on Illumination 1931 (CIE 1931) color space diagram of the NC conjugates consisting of different average number of acceptors per donor. The photographs of the colloidal suspensions of the conjugates corresponding to the symbols labeled in the graph are shown as insets. The non-conjugated Ga_2O_3 NCs emit blue light (inset 1). The addition of CdSe/CdS NCs increases the orange-red contribution to the spectral power distribution, owing to both energy transfer and direct excitation. For an optimal ratio of CdSe/CdS to Ga_2O_3 NCs the colloidal NC conjugate suspension has color coordinates in the white light emitting region (0.345, 0.282) (inset 2). The orange-red contribution becomes dominant for high concentration of the CdSe/CdS NCs (inset 3), reaching bright orange color for pure CdSe/CdS NC suspension (inset 4). The CIE 1931 diagram for the mixtures of Ga_2O_3 and CdSe/CdS NCs is shown in Figure A.4 (Supplementary Materials) for comparison. These results demonstrate the promise of using inorganic building blocks to generate tunable white light with characteristic spectral and color properties.
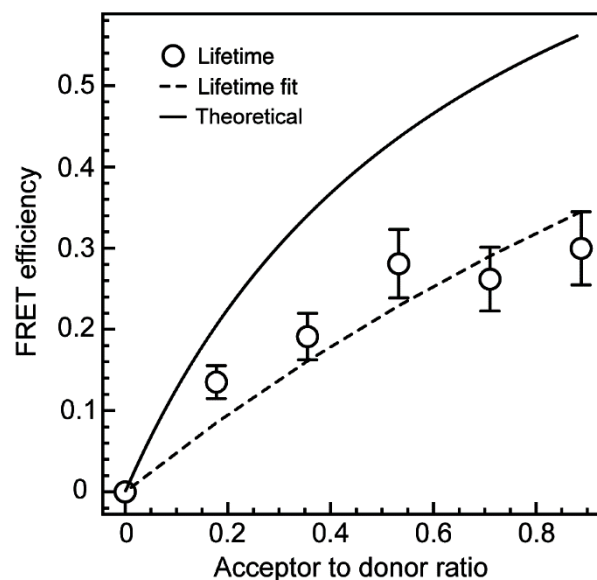
Figure 2.6. FRET efficiency in Ga₂O₃-CdSe/CdS NC conjugate (circles) determined from the DAP PL lifetime data corrected for the lifetime shortening due to TGA binding. The experimental data were fit using Equation 2.5 (dashed line). Solid line is the FRET efficiency predicted by the Förster theory (Equation 2.3).
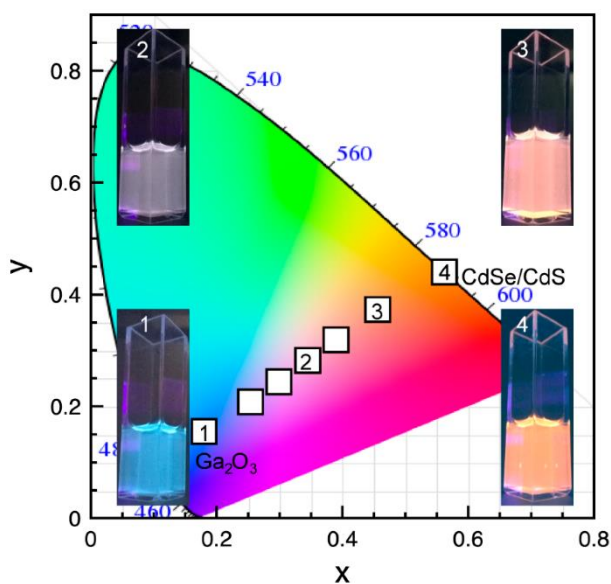
Figure 2.7. International Commission on Illumination 1931 (CIE 1931) color coordinate diagram for Ga₂O₃-CdSe/CdS NC conjugate having different acceptor to donor ratio. The photographs of the colloidal nanoconjugates corresponding to data points labeled in the graph are shown as insets.

2.4. Conclusions

In summary, we demonstrated a new white light-emitting colloidal NC conjugate consisting of CdSe/CdS core/shell NCs connected to γ-Ga₂O₃ NCs via TGA. Owing to the short

chain of TGA molecule, the NC conjugate is a donor-acceptor system undergoing FRET, where Ga_2O_3 NCs act as energy donors and CdSe/CdS NCs as energy acceptors. In spite of the direct excitation of the acceptor NCs, the FRET mechanism is evident through quenching of the donor PL, shortening of the donor emission lifetime, and an increase in the acceptor emission. The control of the CdSe/CdS NC excitation by simultaneous light absorption and energy transfer from Ga_2O_3 NCs allows for the control of the overall emission chromaticity of the NC conjugate, including the generation of the white light. The results of this work represent a step toward the design of all-inorganic white light emitting phosphors for various lighting applications.

2.5. Supplementary Materials

The following are available in Appendix A. Figure A.1: deconvoluted PL spectra of CdSe/CdS NCs, Figure A.2: absorption spectrum of TGA, Figure A.3: excitation spectra of CdSe/CdS NCs in the NC conjugate, Figure A.4: CIE 1931 color space diagram for mixtures of non-linked CdSe/CdS and Ga_2O_3 NCs.

Chapter 3. Surface-Enabled Energy Transfer in Ga₂O₃– CdSe/CdS Nanocrystal Composite Films: Tunable All-Inorganic Rare Earth Element-Free White-Emitting Phosphor[2]

Development of inorganic phosphors capable of generating white light in a homogeneous and reproducible fashion without the use of rare earth elements can lead to an efficient, long-lasting, and sustainable solid state lighting. The design of such phosphors requires that different inorganic components emitting in complementary spectral ranges are electronically coupled to avoid the challenges associated with a multicomponent approach, such as inhomogeneity, poor chromaticity control, and low color rendering index. Here, we demonstrate coupling between electronically excited blue-emitting Ga_2O_3 and orange-red-emitting CdSe/CdS core/shell nanocrystals by surface-enabled Förster resonance energy transfer. This energy transfer process is evident from quenching of Ga_2O_3 (donor) and an enhancement of CdSe/CdS (acceptor) nanocrystal emission and is further confirmed through the diminished lifetime of Ga_2O_3 and significantly extended lifetime of CdSe/CdS nanocrystals in the composite films. Controlling the energy transfer efficiency by adjusting the separation and distribution of codeposited CdSe/CdS and Ga_2O_3 nanocrystals allows for tuning of the emission color. White light is reproducibly generated for [CdSe/CdS]:[Ga_2O_3] ≈ 0.5 by tuning energy transfer efficiency to be ca. 25% using 4.5 ± 0.3 nm Ga_2O_3 and 6.4 ± 0.3 nm CdSe/CdS nanocrystals. The main goal of this work is to quantitatively explore the energy transfer coupling between heterogeneous nanocrystals having complementary optical properties, anchored without the application of organic linkers. These broadly relevant results are applied to demonstrate a path to all-inorganic rare earth element-free nanocrystal phosphors for potential application in white light-emitting diodes and other light-emitting devices.

3.1. Introduction

Solid state lighting (SSL) has gradually matured into a mainstream technology, with the prospect to fully replace incandescent and fluorescent lamps for general lighting applications in the near future. This paradigm shift is motivated by the necessity for a reduction in the global electrical power consumption, of which ca. 20% is used for lighting.[116] Inorganic semiconductor light-emitting diodes (LEDs), as the most prominent SSL technology, have a number of other advantages over incandescent light bulbs, including small size, mechanical durability, and long lifetime.[116,132] These characteristics make LEDs suitable for a host of other applications, including automotive industry, architectural lighting, and displays. On the basis of the United States Department of Energy (DOE) estimates, projected conversion to LEDs by 2030 would reduce annual electricity consumption by ca. 300 TWh and carbon emission by 210 million metric tons.[133]

However, the design of white LEDs (WLEDs) remains challenging and their adoption by consumers relatively slow. The generation of white light by WLEDs is generally based on combined emissions from multiple independent components,[134] which leads to inhomogeneous and inconsistent output. The RGB approach involves combining three separate diodes emitting primary colors, red (R), blue (B), and green (G), in a single light bulb.[134] This approach proved to be complex and costly owing to the challenges in fabricating devices with the optimal balance of the primary colors necessary to obtain white light with desired characteristics. In an alternative strategy, light emitted by blue or ultraviolet (UV) LEDs is partially downconverted using a selected phosphor or a combination of phosphors.[132,135] White light is then generated by combining the emissions from LED and/or remote phosphors.[118,132,134–136] The most common remote phosphor in commercially available WLEDs is yellow-emitting Ce^{3+}-doped yttrium aluminum garnet (Ce^{3+}:YAG).[118] In this case, WLEDs are fabricated by incorporation of Ce^{3+}:YAG into a blue InGaN/GaN LED. The combination of the LED and phosphor emissions approximates a white light, although with a low color rendering index (CRI) and high correlated color temperature (CCT). The main reason for low CRI and high CCT is the lack of sufficient spectral density in red,[136] necessitating the addition of suitable red-emitting phosphors, usually containing europium ions.[119,120] Although the phosphor-converting LEDs are easier to manufacture than RGB diodes, they depend on rare earth elements, which are critical for a

variety of civilian and military technologies, including renewable energy, electronics, telecommunication, and advanced defense systems.[137] In addition, rare earth phosphor-converting WLEDs lack the consistency of the generated light, due to challenges of matching the emissions of multiple components.

In recent years a number of approaches to inorganic phosphor-converted WLEDs without the use of rare earth elements have been demonstrated. Examples of white light-emitting phosphors include mixtures of semiconductor nanocrystals (NCs) of varying sizes and compositions,[124,138–140] II–VI NCs that combine excitonic and surface defect emissions,[141,142] Mn^{2+}-doped II–VI quantum dots exhibiting surface defect and dopant intraionic emissions,[143] and codoped ZnSe quantum dots which combine excitonic emission with luminescence of multiple dopant centers.[144] Although these examples represent significant steps toward rare earth metal-free LEDs, they require sensitive control of the surface states and dopant incorporation and speciation and generally yield only specific emission chromaticity values.

Continuous tuning of the emission color has been achieved by hybrid organic–inorganic nanostructures obtained by conjugating luminescent colloidal metal oxide nanocrystals with organic fluorophores emitting in the complementary spectral range.[27,105] We developed a facile procedure for binding of the selected organic dye molecules to NC surface sites via carboxylic functional groups.[144] This procedure relies on the transport of organic fluorophores from aqueous solution to a nonpolar solvent containing suspended NCs. Using functionalized colloidal metal oxide NCs, we were able to expand the PL range of the defect-based NC emission via Förster resonance energy transfer (FRET),[106] thereby creating an efficient white light-emitting phosphor. The obtained hybrid material acts as a single illumination entity, rather than a mixture, and provides a homogeneous and uniform white light emission.[27] Emission chromaticity tuning has been achieved by controlling the average NC size and the type and number density of surface-bound molecules. A potential drawback of this system is the presence of organic molecules, which may be sensitive to thermal and photodegradation during LED operation. In relation to the above considerations, exploring the design of tunable, fully inorganic white light-emitting phosphors consisting of coupled, rather than separate, components that do not contain rare earth metals could lead to the new paradigm in the fabrication of lighting devices.

We have recently shown that CdSe/CdS core/shell NCs can be bonded to Ga_2O_3 NCs using an organic linker and undergo excitation by FRET analogously to dye-conjugated Ga_2O_3 NCs.[145] The ability to tune PL energy of colloidal semiconductor NCs by changing both the core size and the shell thickness[146] or composition[147] makes them ideally suited for the design of light-emitting phosphors. Here, we demonstrate substrate-enabled FRET between codeposited Ga_2O_3 and CdSe/CdS NCs, which allows for generation of tunable white light in a reproducible manner without the use of an organic linker or fluorophore. While FRET between the same type of molecularly linked NCs having different sizes has been studied extensively, the coupling of different types of NCs can lead to unique functional properties and targeted applications.[148] The results of this work demonstrate a path to all-inorganic rare earth element-free NC composite for potential application in WLEDs.

3.2. Expirimental Section

3.2.1. Chemicals

All chemicals are commercially available and used as received. Gallium acetylacetonate ($Ga(acac)_3$) (99.99%) was purchased from Strem Chemicals. Cadmium oxide powder (99.99%), selenium powder (99.99%), 1-octadecene (90%), 1-dodecanethiol (98%), oleylamine (70%), oleic acid (90%), tributylphosphine (TBP) (92%), tetradecylphosphonic acid (TDPA) (97%), and trioctylphosphine oxide (TOPO) (90%) were purchased from Sigma-Aldrich.

3.2.2. Synthesis of Ga_2O_3 Nanocrystals

Gallium oxide NCs were synthesized using the previously reported procedure.[24] Briefly, 0.5 g of $Ga(acac)_3$ was placed in a 100 mL three-neck round-bottom flask with 14 g of oleylamine. The flask was purged with argon and heated to 250 °C over the period of an hour. The reaction was held at this temperature for 1 h; then the flask was cooled naturally to room temperature. The product was precipitated with 20 mL ethanol and centrifuged at 3000 rpm. Washing with ethanol was repeated three more times. The NCs were then capped with TOPO by submersion in 4 g of molten TOPO at 90 °C and then precipitated and washed with ethanol two more times to remove excess TOPO. TOPO-capped Ga_2O_3 NCs were finally suspended in hexane.

3.2.3. Synthesis of CdSe/CdS Core/Shell Nanocrystals

CdSe NCs were synthesized using a reported method.[79] Briefly, 60 mg of CdO, 210 mg of TDPA, and 3 g of TOPO were placed in a 100 mL three-neck round-bottom flask. The reaction vessel was heated to 150 °C, degassed for 1 h, and then backfilled with argon. The reaction flask was then brought to 320 °C, and 1 mL of TBP–Se solution (prepared separately by combining 1 mL of TBP and 60 mg of Se in a degassed container) was rapidly injected. The flask was held at 320 °C until the desired NC size was achieved and then cooled using compressed air. When the temperature reached 80 °C, methanol was injected and the product was centrifuged at 3000 rpm and then suspended in hexane.

For CdS shell growth,[89] 100 nmol of synthesized CdSe NCs was placed in a 100 mL three-neck round-bottom flask containing 3 mL of each oleylamine and 1-octadecene. The flask was degassed under vacuum for 1 h and purged with argon. The temperature was then increased to 320 °C. Meanwhile, a dropwise injection of $Cd(OAc)_2$ (prepared separately by heating a 1:4 molar ratio of CdO to oleic acid in 6 mL of octadecene to 220 °C in an oxygen-free container) and dodecanethiol was started at 240 °C and carried out for 3 h. A 3 mL amount of oleic acid was then added, and the reaction mixture was left at the designated temperature for an additional hour. The obtained reaction product was cooled to room temperature using compressed air, washed with acetone, and centrifuged at 3000 rpm before dispersing in hexane.

3.2.4. Preparation of Composite Films

0.5 mL of 5 μM Ga_2O_3 NC stock suspension was placed in a vial, a different volume of CdSe/CdS NC suspension (5 μM) was added, and the volume of the total suspension was brought to 1.0 mL. Glass substrates, having a surface area of approximately 7×7 mm, were cleaned with ethanol. Three 100 μL aliquots of a NC suspension mixture were gradually dropped on the substrate and allowed to dry.

3.2.5. Sample Characterization

The size and morphology of colloidal NCs were characterized by transmission electron microscopy (TEM) imaging using a JEOL-2010F microscope operating at 200 kV. The specimens were prepared by depositing NCs from dilute colloidal suspensions on copper grids with lacey Formvar/carbon support film purchased from Ted Pella, Inc.

The crystal structure was confirmed by X-ray diffraction (XRD) performed with an INEL diffractometer equipped with a position-sensitive detector and monochromatic Cu Kα1 radiation source (λ = 1.5418 Å).

The composite NC films were examined by scanning electron microscopy (SEM). SEM imaging and energy-dispersive X-ray spectroscopy (EDX) elemental mapping were performed with a LEO 1530 microscope. The macroscopic film thickness and its variation were estimated by scratching the film at different regions and scanning with a KLA Tencor P-6 profilometer.

3.2.6. Spectroscopic Measurements and Analysis

Absorption spectra were recorded with a Varian Cary 5000 UV-vis-NIR spectrophotometer with 1 nm bandpass. Steady-state PL spectroscopy measurements were performed using a Varian Cary Eclipse fluorescence spectrometer. Unless stated otherwise, the PL spectra were collected upon excitation at 256 nm (corresponding to band edge of γ- Ga_2O_3 NCs). Time-resolved PL measurements were performed with a Horiba Jobin Yvon iHR320 time-correlated single-photon counting (TCSPC) spectrometer equipped with a 249 nm NanoLED excitation source (1.2 ns fwhm pulse width, 100 kHz repetition rate) and a Horiba Jobin Yvon TBX picosecond detector. Three-dimensional (3D) TCPSC maps were constructed by collecting the PL time decay profiles at wavelengths from 320 to 600 nm in 5 nm steps with a 540 s integration time.

3.3. Results and Discussion

Resonance energy transfer involves a nonradiative coupling of the electronic transition moments of the donor and acceptor species, which is analogous to coupling of the electronic oscillators.[96] For weakly coupled fluorophores, the energy transfer requires proximity of the donor and acceptor, as shown schematically in Figure 3.1a for Ga_2O_3 as the donor (blue sphere) and CdSe/CdS as the acceptor (red sphere) NCs. This energy transfer process is effectively described by Förster theory,[94] which allows for quantitative analysis of the electronic coupling and the extraction of geometric parameters of the donor–acceptor pairs using steady-state and time-resolved spectroscopic data. In colloidal NC suspensions, the average separation between donors and acceptors is generally too large (>250 nm) for any appreciable energy transfer between NCs acting as donors and acceptors to occur (Figure 3.1b, top left).[145] However, linking

Ga$_2$O$_3$ and II–VI NCs with a short bifunctional ligand can lead to FRET between the two types of NCs (Figure 3.1b, top right).[145] Owing to the possibility of tuning the blue-green and orange-red emission by adjusting the size of Ga$_2$O$_3$ and CdSe/CdS NCs, respectively, this NC conjugate can in principle be used to generate white light with desired chromaticity. This approach to generating white light still involves organic linkers, which may be sensitive to degradation by heating and UV exposure. Furthermore, it results in a low concentration limit of the FRET pairs in the final suspension as well as a significant probability of donor–donor and acceptor–acceptor binding, which reduces the effectiveness of FRET. Our goal in this work was to explore the possibility of inducing and controlling FRET between metal oxide donor and II–VI acceptor NCs to obtain tunable white light emission without the use of organic molecules or rare earth elements. Surprisingly, simple codeposition of Ga$_2$O$_3$ and CdSe/CdS NCs on a transparent substrate allows for tight packing of the NCs with the controlled ratio of the energy acceptors and donors (Figure 3.1b, bottom), enabling the generation of homogeneous white light with high brightness and desired characteristics.
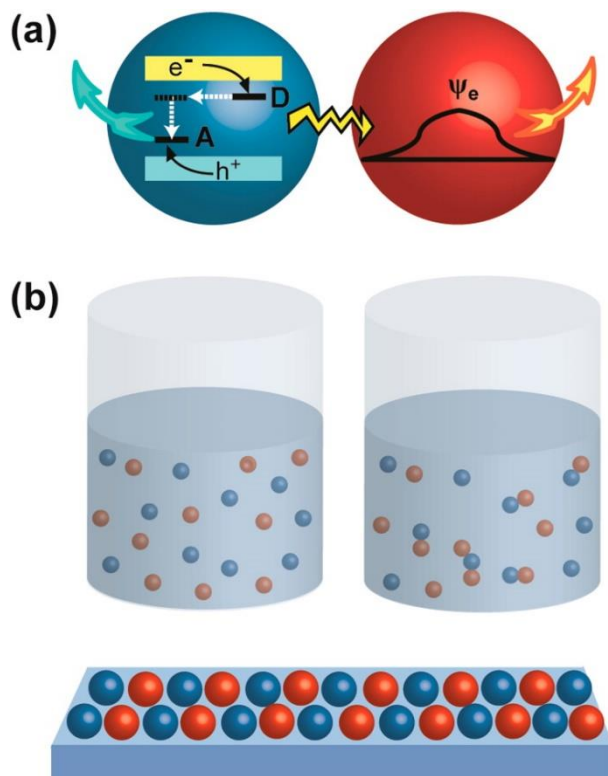
Figure 3.1. (a) Schematic representation of the resonance energy transfer between Ga$_2$O$_3$ and CdSe/CdS core/shell NCs. (b) Schematic representation of the spatial correlation between free-standing (left), molecularly linked (right), and substrate codeposited (bottom) donor (blue) and acceptor (red) NCs.

TEM images of Ga_2O_3 and CdSe/CdS NCs used in this study are shown in Figure 3.2a and 3.2b, respectively. Spherical Ga_2O_3 NCs have an average diameter of 4.5 ± 0.3 nm and cubic crystal structure characteristic for γ-phase Ga_2O_3 (Figure B.1). Core/shell CdSe/CdS NCs, acting as energy acceptors, have an average size of 6.4 ± 0.3 nm, with a core size of ca. 1.8 nm (Figure B.2). A typical SEM image of a composite white light-emitting film obtained by codeposition of γ- Ga_2O_3 and CdSe/CdS NCs (vide infra) is shown in Figure 3.2c. The substrate is relatively evenly coated with some microscopic roughness and voids formed during the drying process. A representative profile of the film cross section is shown in Figure 3.2d, indicating a film thickness of ca. 30 μm. Additional profilometry measurements in different regions on the substrate suggest a uniform topology of the film (Figure B.3). SEM-EDX elemental mapping demonstrates homogeneous distribution of Ga_2O_3 and CdSe/CdS NCs within the film (Figure 3.2and 3.2f), confirming the proximity of the donor and acceptor NCs.
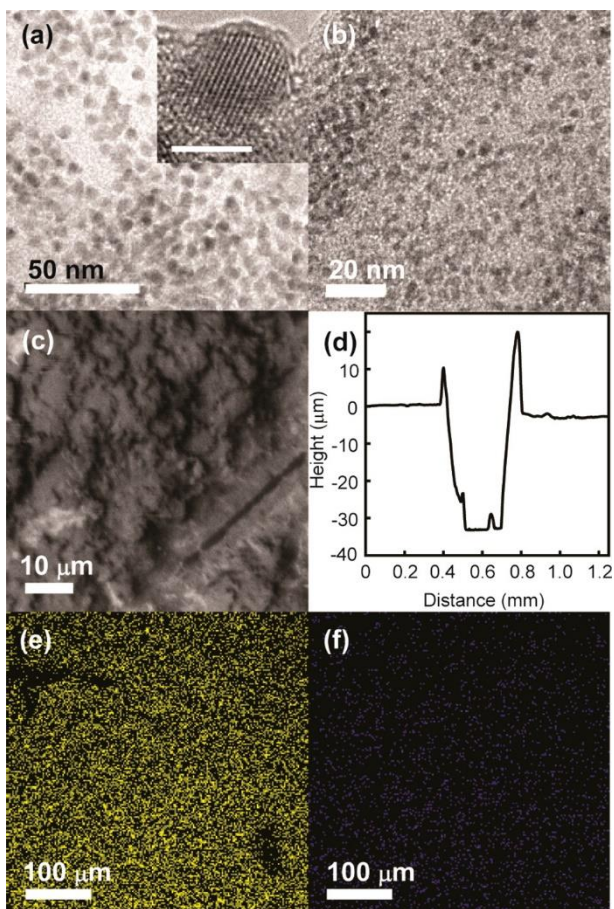
Figure 3.2. (a) TEM image of CdSe/CdS NCs. (Inset) Lattice-resolved TEM image of a single NC (scale bar, 5 nm). (b) TEM image of Ga₂O₃ NCs. (c) SEM image of a composite white light-emitting film prepared from colloidal CdSe/CdS and Ga₂O₃ NC mixture. (d) Thickness profile of a typical NC composite film. SEM-EDX elemental maps of the white light-emitting NC composite film for (e) Ga and (f) Cd.

We previously reported the generation of white light by dye-conjugated metal oxide NCs, enabled by FRET from electronically excited NCs to organic fluorophores bound to NC surfaces.[143,144] The ability to control blue emission by controlling the size of metal oxide NCs and the orange-red emission by selecting a dye molecule with optimal PL spectrum allows for the design of homogeneous quasi-single white light-emitting phosphor. Quantum dots based on CdSe have size-tunable PL throughout the visible range and can also be excited by a FRET mechanism,[149,150] making them an attractive material for the design of composite inorganic white light-emitting phosphors. In this work we used Ga_2O_3 NCs as a blue emitter.[21,27] These NCs display a broad PL band in blue-green (Figure 3.3a, blue trace), which arises from the recombination involving defect-induced electron donor and acceptor states within the NC band gap.[122,123] Significant broadening of this donor–acceptor pair (DAP) recombination band is

45

associated with a range of separations between donor (oxygen vacancy) and acceptor (gallium–oxygen vacancy pair) sites, which defines the Coulomb interactions among them.[122] We chose CdSe/CdS core/shell NCs as a secondary solid-state emitter because they possess a strong orange-red emission that can be tuned by controlling the NC core diameter and shell thickness (Figure 3.3a, red dashed trace). These dimensional parameters were optimized to allow for the generation of white light when CdSe/CdS PL is combined with the DAP emission of Ga_2O_3 (vide infra). Furthermore, the PL band of Ga_2O_3 NCs strongly overlaps with the absorption spectrum of CdSe/CdS NCs (Figure 3.3a, red trace), enabling their excitation by FRET mechanism.[96]
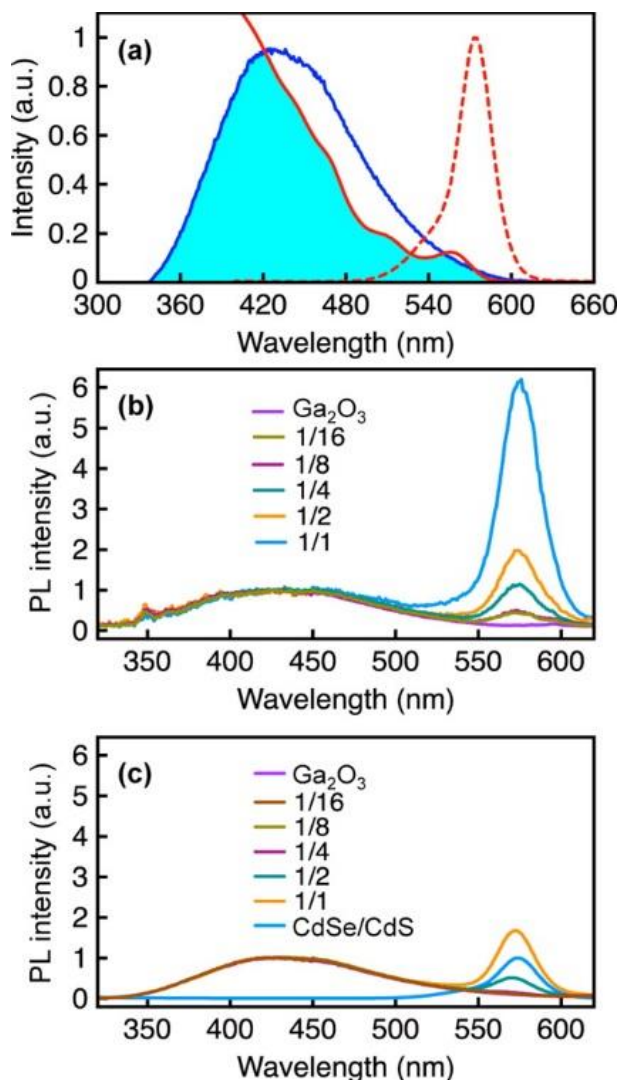
Figure 3.3. (a) PL spectrum of Ga_2O_3 NCs (blue line), and absorption (solid red line) and PL (dashed red line) spectra of CdSe/CdS NCs deposited on glass substrates. Shaded area indicates spectral overlap as an essential requirement for FRET. PL spectra of (b) composite NC films and (c) colloidal mixtures containing different acceptor to donor ratios upon excitation into the Ga_2O_3 band gap. Spectra are

PL spectra of the composite NC films containing different ratios of CdSe/CdS to Ga$_2$O$_3$ NCs upon excitation into the Ga$_2$O$_3$ band gap are shown in Figure 3.3b. Although increasing concentration of CdSe/CdS NCs results in quenching of Ga$_2$O$_3$ emission (see Figure B.4), the spectra in Figure 3.3b are normalized at the Ga$_2$O$_3$ DAP PL band to emphasize the relative increase in CdSe/CdS NC emission intensity. In addition to FRET, CdSe/CdS NCs are also a subject to direct excitation and reabsorption of light emitted by Ga$_2$O$_3$ NCs. To elucidate the effect of FRET in the composite films we collected the PL spectra of colloidal mixtures used for preparing the NC films (Figure 3.3c). In contrast to codeposited NCs, these spectra exhibit a smaller decrease in Ga$_2$O$_3$ PL intensity and a smaller increase in the CdSe/CdS emission intensity (see also Figure B.4). A decrease in Ga$_2$O$_3$ PL intensity is mostly due to competitive absorption by CdSe/CdS NCs and possibly occasional collisions of Ga$_2$O$_3$ NCs due to Brownian motion in a suspension. Similarly, an increase in CdSe/CdS emission intensity arises from direct excitation at ca. 250 nm and to much smaller degree reabsorption of blue light emitted by Ga$_2$O$_3$ NCs. Consequently, both Ga$_2$O$_3$ PL quenching and an increase in the CdSe/CdS NC emission in the composite films are consistent with FRET.

An important manifestation of FRET is diminishing of the donor excited state lifetime in the presence of acceptors.[96] Figure 3.4a shows the PL intensity time decay of the Ga$_2$O$_3$ NCs for different concentrations of CdSe/CdS NCs in the composite films. As expected, with increasing amount of acceptor NCs, the rate of the DAP emission decay increases, consistent with FRET coupling. FRET efficiency (η) can be calculated from the reduction in the lifetime of the donor excited state in the presence of the acceptors as

$$\eta = \frac{\tau_{DA}}{\tau_D} \qquad\qquad 3.1$$

where (τ_D) and (τ_{DA}) are the lifetimes of the donor alone and in the presence of the acceptors, respectively. The DAP emission time decay does not follow a typical exponential or hyperbolic form;[21,38,41] hence, integrated lifetimes were used to calculate η. The FRET efficiency, calculated using Equation 3.1, as a function of the relative amount of CdSe/CdS NCs

is shown in Figure 3.4b. According to the Förster theory, the energy transfer efficiency can be expressed as

$$\eta = \frac{nR_0^6}{nR_0^6 + nR_{DA}^6}$$

where (R_{DA}) is the average separation between donors and acceptors, n is the acceptor to donor ratio, and (R_0) is the critical (Förster) radius. The Förster radius is defined as the donor–acceptor separation corresponding to $\eta = 0.5$

$$R_0 = \left(\frac{9000(\log 10)\kappa^2 Q_0}{128\pi^5 N_A n_r^4} J(\lambda) \right)^{1/6}$$

3.3

where (Q_0)is the donor quantum yield in the absence of the acceptor, nr is the index of refraction of the surrounding medium, NA is Avogadro's number, ($J(\lambda)$) is the spectral overlap integral, and (κ^2) is the dipole alignment factor which we assumed to be 2/3 based on random orientation of the acceptor NCs.[103,130] Equation 3.2 is found to be valid when the ratio of the donor and acceptor can be accurately controlled or if all donor binding sites are fully occupied.[103,131] These conditions are satisfied only in a limited number of cases. More often the distribution of acceptors per donor follows the Poissonian statistics,[107,108] for which the FRET efficiency attains the form

$$\eta(\xi, R) = \sum_0^\infty \frac{\xi^n e^{-\xi}}{n!} \left[\frac{nR_0^6}{nR_{DA}^6 + nR_0^6} \right]$$

3.4

where (ξ) is an average number of acceptors per donor while n is a whole-number acceptor to donor ratio. The best fit to the experimentally determined η using Equation 3.4 for R_0 = 6.65 nm is shown in Figure 3.4b (dashed line), where R_{DA} is the fitting parameter. The resulting value of R_{DA} is 6.8 nm, which is very reasonable given the sizes of donor and acceptor NCs and their random packing. This R_{DA} value was used to calculate η in Equation 3.2 for different acceptor to donor ratios (solid line in Figure 3.4b). Förster theory (Equation 3.2)

provides a better match to the experimental data at low acceptor to donor ratios. However, due to the absence of specific binding sites and well-defined number of acceptors per donor, the Poissonian fit (Equation 3.4) shows significantly better agreement with the experimental data at high acceptor to donor ratios. The overall discrepancy between the two functions and the experimental data is likely due to a wide range of R_{DA} values associated with the nature of the system and sample preparation.
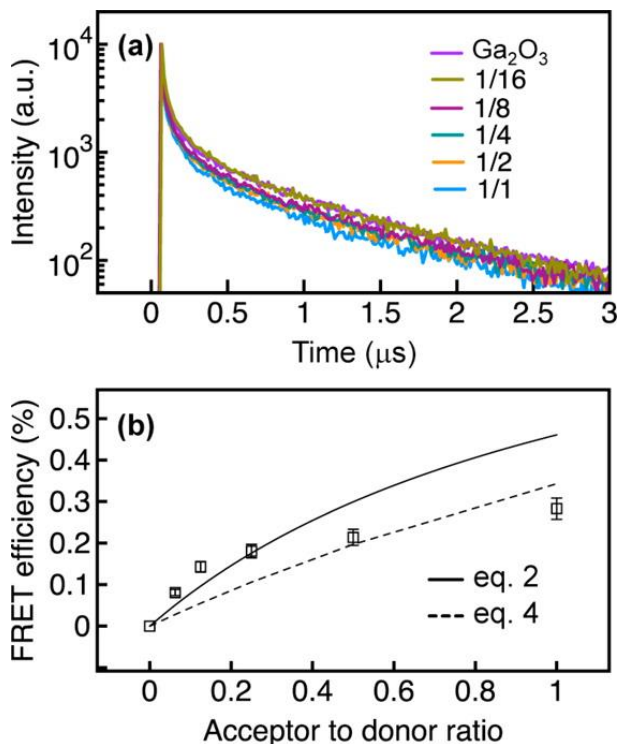
Figure 3.4. Normalized time-resolved PL data of the composite NC films measured at 425 nm (the maximum of the Ga$_2$O$_3$ DAP PL band) upon excitation at 249 nm. Acceptor to donor concentration ratios ([CdSe/CdS]/[Ga$_2$O$_3$]) are indicated in the graph. (b) FRET efficiency as a function of [CdSe/CdS]/[Ga$_2$O$_3$] NC ratio. Solid and dashed lines are best fits to Equations 3.2 and 3.4, respectively.

Figure 3.5a shows time-resolved PL decays of composite NC films monitored at 575 nm (CdSe/CdS NC emission maximum) upon excitation at 249 nm for increasing CdSe/CdS to Ga$_2$O$_3$ NC ratio (direction of the arrow in Figure 3.5a). Unlike DAP emission of Ga$_2$O$_3$ NCs, which has a lifetime of several microseconds, CdSe/CdS NCs have an average excited state lifetime of ca. 16 ns, up to 103 times shorter than Ga$_2$O$_3$ NCs. In addition to shortening of the lifetime of the Ga$_2$O$_3$ DAP emission, FRET should also lead to the elongation of the CdSe/CdS NC PL lifetime. The energy transfer adopts the dynamics of the Ga$_2$O$_3$ NC PL decay, effectively extending the apparent lifetime of the CdSe/CdS NC emission, upon excitation into Ga$_2$O$_3$ band

gap. To separate the effect of FRET from the residual DAP PL at 575 nm, we constructed delayed PL spectra by recording decay curves at different emission wavelengths. Figure 3.5b compares the spectra corresponding to 2.8 μs delay for pure Ga_2O_3 (purple line), pure CdSe/CdS (orange line), and composite NC films (blue line). CdSe/CdS NCs, solely deposited on a glass substrate, show no observable emission intensity 2.8 μs after excitation, while afterglow of Ga_2O_3 NCs remains strong. However, in the composite film, a significant emission intensity of CdSe/CdS NCs persists at ca. 575 nm upon excitation at 249 nm (blue line). The maps of the PL decay dynamics as a function of wavelength for Ga_2O_3 and composite NC films are shown in Figure 3.5c and 3.5d, respectively. The PL intensity of CdSe/CdS NCs clearly follows that of Ga_2O_3 NCs. This result serves as another evidence that the excitation of CdSe/CdS NCs occurs by FRET, allowing for convenient control of the chromaticity of the emitted light.
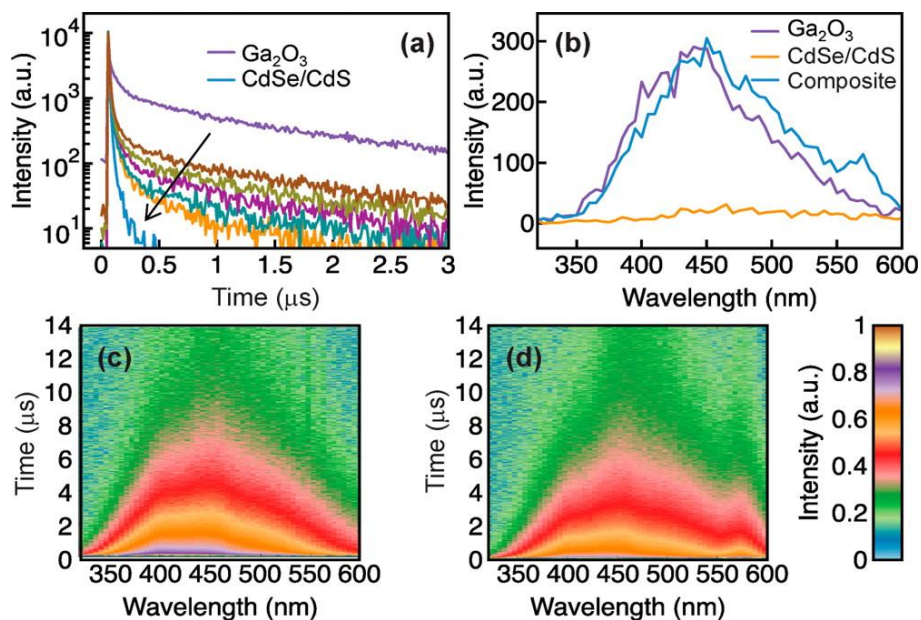
Figure 3.5. (a) Normalized time-resolved PL data of the NC films measured at 575 nm upon excitation at 249 nm for different acceptor to donor ratios (arrow indicates an increase in the relative amount of CdSe/CdS NCs). (b) Delayed PL spectra constructed by collecting the decay curves at different wavelengths (delay time, 2.8 μs). Maps of the PL decay dynamics as a function of wavelength for (c) Ga₂O₃ NC films and (d) composite NC films deposited on a glass substrate.

The ability to control FRET in composite films fabricated by simple codeposition of NC building blocks emitting in complementary spectral regions paves the way for a convenient fabrication of all-inorganic white light-emitting structures and devices with tunable lighting characteristics. To demonstrate the flexibility of this approach, we plotted the CIE 1931 diagram

color coordinates for a series of composite films containing different Ga_2O_3 to CdSe/CdS NC ratio (Figure 3.6a) with the ratio of Ga_2O_3 to CdSe/CdS NCs indicated in the inset. The color coordinates of the colloidal mixtures used for preparing the films are shown in Figure 3.6b. The comparison of the two diagrams reveals a significant difference in the chromaticity of the composite films and analogous colloidal mixtures. The photographs showing the emission of these colloidal mixtures and the corresponding composite films are compared in Figure 3.6c. The visual difference in PL chromaticity is a direct consequence of FRET, enabled by anchoring NCs on a solid substrate. The composite film prepared with the NC concentration ratio $[Ga_2O_3]/[CdSe/CdS] = 2$ emits white light with the color coordinates (0.31, 0.28), based on the optimized energy transfer parameters. Determination of the relative quantum yield of this film is complicated by the fact that the samples are not in the solution phase, which makes it difficult to consistently measure and compare their absorbance and integrated PL intensity to those of a reference fluorophore solution. Furthermore, the PL efficiency is impacted by the fact that there is a relatively significant direct excitation of CdSe/CdS NCs in the composite films, together with some reabsorption of the Ga_2O_3 NC emission, as described above. However, the overall quantum yield can be estimated based on the FRET efficiency and the ratio of acceptors and donors in the composite films. Although defect-originated trap emissions are generally less efficient than the PL arising from exciton transitions, the DAP emission of Ga_2O_3 nanocrystals is determined to be up to ca. 30%,[123] which is an appreciable value with a prospect for some practical applications. By introducing an energy acceptor with a superior quantum yield relative to the donor, an increase in the overall quantum yield can be achieved via FRET. This is indeed the case for our system, given that the quantum yield of CdSe/CdS NCs can be as high as 90%, depending on the NC core size and shell thickness. On the basis of the determined FRET efficiency (25%) and the estimated fraction of the incident radiation used for the Ga_2O_3 NC excitation (ca. 65%), routinely achieved quantum yield of 50% for CdSe/CdS NCs results in the overall efficiency of the white light-emitting composite films of 40%. The quantum yield of the analogous colloidal NC mixture is estimated to be ca. 37%, suggesting that FRET increases the emission efficiency of the composite white light-emitting film by ca. 10% relative to the colloidal mixture, in addition to tuning its chromaticity. Surface-enabled FRET allows for seamless integration of NCs as a remote phosphor into LEDs and other optical devices by simple spin coating of colloidal suspensions. Fabrication of practical LEDs using this approach would

51

require further development, including investigation of the optimal phosphor configuration (i.e., codeposition vs layer-by-layer deposition of Ga_2O_3 and CdSe/CdS NCs on LED chips) and the design of donor NCs absorbing in the near-UV region. Importantly, it is expected that these results are transferable to other composite multifunctional materials requiring electronic coupling between NCs having complementary properties.
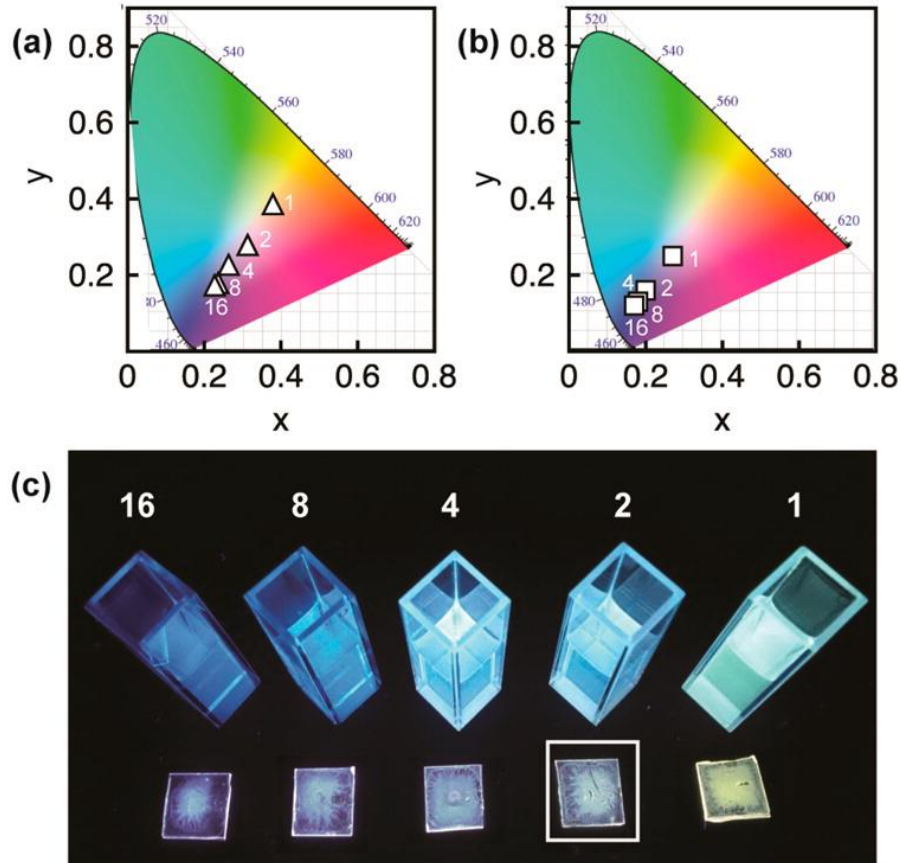
Figure 3.6. CIE 1931 diagrams for (a) composite films prepared by depositing colloidal Ga_2O_3 and CdSe/CdS NC mixtures on a glass substrate and (b) corresponding Ga_2O_3 and CdSe/CdS colloidal NC mixtures. (c) Photographs of the samples in the colloidal form and deposited on glass substrates. Numbers indicated on the graphs represent [Ga_2O_3]/[CdSe/CdS] NC concentration ratios. White light-emitting composite film corresponding to [Ga_2O_3]/[CdSe/CdS] = 2 is indicated in c.

3.4. Conclusions

In summary, we demonstrated a new approach to all-inorganic tunable white light-emitting phosphor based on surface-enabled FRET between codeposited Ga_2O_3 and CdSe/CdS core/shell NCs. The emission of Ga_2O_3 NCs arises from recombination of an electron trapped in a shallow defect-originated electron donor state with a hole trapped in an electron acceptor state.

This DAP emission band is strongly broadened due to the large surface area and a range of separations between participating defect sites, necessitating only a small additional spectral density in the orange-red to produce white light. The ability to control the emission energy and optimize the quantum yield of core/shell II–VI NCs by controlling the core size and shell thickness renders these materials very promising candidates for energy acceptors. In this work we demonstrated the generation of tunable white light by composite films consisting of Ga_2O_3 and CdSe/CdS core/shell NCs. Fabrication of composite films by simple codeposition of Ga_2O_3 and CdSe/CdS NCs allows for a control of the NC distribution and separation without the use of an organic linker. The proximity of the constituent NCs enables their coupling by FRET. The electronic coupling between two complementary color-emitting NCs allows for the design of homogeneous and tunable white phosphor by controlling the CdSe/CdS to Ga_2O_3 NC ratio. The results of this work demonstrate a path to all-inorganic rare earth element-free NC composite for potential application in WLEDs and more broadly multifunctional inorganic materials requiring electronic coupling of heterogeneous NCs.

Chapter 4. Extending Afterglow Emission of Ga$_2$O$_3$ Nanocrystals by Dy^{3+} Dopant-Induced Carrier Trapping

Design and preparation of persistently luminescent nanostructured phosphors is of a significant interest in lighting, photonic, and photovoltaic technologies. Among other applications, this class of materials could enable seamless integration with the next generation of nanocrystal solar cells and photocatalysts, where they could provide a light source in the absence of natural lighting. However, afterglow generally occurs in bulk phosphors synthesized by high-temperature solid-state reactions. Here we report the synthesis of colloidal Dy^{3+}-doped Ga$_2$O$_3$ nanocrystals and demonstrate an extension of the nanocrystal afterglow, arising from native-defect-based donor-acceptor pair recombination, relative to undoped Ga$_2$O$_3$ nanocrystals. Using temperature-dependent steady-state and time-resolved photoluminescence measurements we show that Dy^{3+} dopants reside in the vicinity of NC surfaces and generate trap states that are significantly shallower than donor states originated by the presence of oxygen vacancies in Ga$_2$O$_3$ nanocrystals. This defect configuration allows for thermal reactivation of kinetically trapped electrons in Dy^{3+} excited states, resulting in an increase in the nanocrystal emission intensity and an extension of the afterglow lifetime with temperature. These results are supported by kinetic Monte Carlo simulation based on the probability of different electron transfer processes. The results of this work demonstrate a pathway to extending afterglow emission and designing long-persistent phosphors of reduced dimensions.

4.1. Introduction

One of the intriguing properties of inorganic solid-state phosphors is a long-lasting luminescence, often referred to as afterglow, which persists for a long time (microseconds to hours) after the excitation source had been switched off.[151] Such long-lived emission allows for a slow release of the accumulated excitation energy in the form of light, making the afterglow phosphors an important component of various decoration products and electronic displays,[152] emergency and traffic signs,[153,154] as well as the platforms for optical imaging,[155,156] medical diagnostics,[157–159] and sensing,[160,161] to name a few. Another emerging application of this class of materials is to use stored energy to provide radiative excitation in photovoltaic devices and photocatalytic systems in the absence of the sunlight or other external lighting sources.[162] The

possibility to use delayed luminescence in the next generation of nanocrystal (NC) solar cells and photocatalysts largely rests upon the ability to design persistently luminescent nanostructured phosphors that can be integrated with NC structures and devices. Design and synthesis of afterglow phosphors in colloidal NC form and understanding their afterglow mechanisms is therefore of significant fundamental and practical importance for new energy-conversion technologies.

A variety of inorganic persistent phosphors having different chemical nature and composition[163] (e.g., oxides,[48] nitrides,[164] sulfides,[165] halides,[166] etc.), luminescence properties (e.g., emission energy and lifetime),[167] and type of excitation (e.g., photoluminescence, cathodoluminescence, thermoluminescence, mechanoluminescence, chemiluminescence, etc.) have been developed over the past few decades. The common characteristics of all phosphors exhibiting persistent luminescence is the coexistence of activators (usually luminescent dopant ions that act as emission centers) and carrier traps (impurity sites responsible for storage and slow release of the excitation energy).[55] The prototype material for persistent luminescence applications is strontium aluminate codoped with Eu^{2+} and Dy^{3+} (Eu^{2+}, Dy^{3+}: $SrAl_2O_4$),[48] where Eu^{2+} ions act as emission centers due to strong interconfigurational parity allowed $4f^65d^1 \rightarrow 4f^7$ transitions, while Dy^{3+} sites provide trap states for energy storage (for details, see Figure C.1).[48,53,151,168] However, the solid state reactions typically used for the synthesis of oxide-based inorganic phosphors require a prolonged high temperature treatment, resulting in an average particle size in the micrometer range, significant particle agglomeration, as well as heterogeneity in particle size and morphology,[151,163] making these phosphors incompatible with various nanophotonic structures and devices.[46,169–173]

We have previously demonstrated a size- and composition-tunable afterglow of colloidal Ga_2O_3 NCs containing both donor and acceptor impurities,[24,122,124,174] where likely donors are positively charged oxygen vacancies ($V_O^{\bullet}$) and possible acceptors are negatively charges gallium-oxygen vacancy pairs [$(V_O,V_{Ga})'$].[21,37,38] When optically excited above the NC band edge, electrons and holes can be bound forming neutral donors (V_O^x) and acceptors ($(V_O,V_{Ga})^x$), respectively, which recombine giving rise to donor-acceptor pair (DAP) emission:

$$\left(V_O,V_{Ga}\right)^x + V_O^x \rightarrow \left(V_O,V_{Ga}\right)' + V_O^{\bullet} + h\nu \text{ (PL)} \qquad \textit{4.1}$$
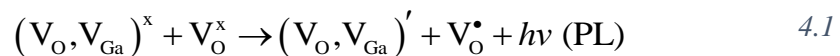
The energy of a photon emitted through DAP recombination can be defined as:

$$E_{DAP} = E_g - (E_D + E_A) + \frac{e^2}{4\pi\varepsilon r} \qquad 4.2$$

where r is the separation between the given donor and acceptor sites in NCs, ε is the dielectric constant, and E_g, E_D, and E_A are the band gap, donor, and acceptor binding energies, respectively. The last term represents stabilizing Coulomb interaction, which is responsible for a perturbation of the ionized donor and acceptor levels toward the conduction and valence band edges, respectively. Consequently, the emission energy varies as $1/r$, enabling a blue shift of DAP PL band with decreasing NC size. The DAP recombination involves a tunnel transfer of an electron from a donor to an acceptor, as the rate determining step, and is also responsible for persistent luminescence of colloidal Ga_2O_3 NCs and for size-dependent decay dynamics.[21,41,42,122] The temperature dependence of the DAP tunnel transfer can be viewed analogously to the thermal component of the tunnel current density in insulating film between two closely-spaced metal electrodes:[175]

$$J_{VT} = J_{V_0}\left(1 + \frac{6\times10^{-9}\, s\varphi T^2}{V^2}\right) \qquad 4.3$$

where J_{V_0} is the current density of tunneling at 0 K, s is the electrode separation (analogous to r in DAP recombination mechanism), φ is the height of a symmetric barrier that an electron must tunnel through, T is the temperature, and V is the potential across the barrier. In case of a single excited electron, J_{V_0} is related to the probability of a tunneling event occurring.

The fact that Ga_2O_3 NCs contain native defects as afterglow activators that can be controlled via reaction conditions[123] implies that only the dopants responsible for energy storage need to be externally introduced to design a longer lasting nanophosphor based on Ga_2O_3. This is particularly important given the well-documented challenges associated with doping colloidal NCs,[176–178] and the possibility of mutual exclusion of different types of dopants. In light of Dy^{3+} acting as an electron trap in Eu^{2+}, Dy^{3+}:$SrAl_2O_4$, we sought to exploit its role in Ga_2O_3 NCs.

Delayed PL spectra of Dy^{3+} ions allowed us to assess the change in dopant speciation with respect to the doping concentration. Using variable-temperature steady-state and time-resolved PL measurements we demonstrated that Dy^{3+} indeed forms trap states in Ga_2O_3 NCs, and established the correlation between the doping concentration and the electronic structure of trap states. Importantly, the formation of these trap states leads to an increase in the DAP PL intensity, and an extension of the DAP emission lifetime at room temperature. The results of this work demonstrate the possibility of compositional manipulation of afterglow in colloidal NC systems, and provides a guideline for the design and preparation of persistent nanostructured phosphors.

4.2. Experimental and Theoretical Methods

4.2.1. Materials

All chemicals are commercially available and used as received. Dysprosium nitrate hydrate $(Dy(NO_3)_3 \cdot nH_2O)$ (99.9 %), oleylamine (70 %) and trioctylphosphine oxide (TOPO)(90%) were purchased from Sigma-Aldrich. Gallium acetylacetonate $(Ga(acac)_3)$(99.99 %) was purchased from STREM Chemical. All chemicals were used as received.

4.2.2. Synthesis of Dy^{3+}:Ga_2O_3 NCs

Dy^{3+}:Ga_2O_3 NCs were synthesized according to previously reported method.[24,179,180] Briefly, 500 mg of $Ga(acac)_3$ and a desired amount of $Dy(NO_3)_3$ were dissolved in a 3 neck round bottom flask and heated to a desired temperature over the course of 1 hour. Once the final temperature was achieved, the reaction was allowed to proceed at this temperature for 1 hour. The flask was then removed from heat and allowed to cool down. The product was flocculated by the addition of ~40 mL of ethanol and the precipitate was collected by centrifuging at 3000 rpm for 10 min; this procedure was performed 5 times to ensure high purity of the colloidal NCs. The isolated product was then added to molten TOPO at 90 °C for 1 hour to remove loosely-bound Dy^{3+} and replace coordinated oleylamine from NC surfaces. The final product was washed with ethanol additional 2 times before being dissolved in hexane.

4.2.3. Nanocrystal Characterization

Phase and purity of Dy^{3+}:Ga_2O_3 NC products were confirmed by X-ray diffraction (XRD) measurements. XRD patterns were collected with an INEL powder diffractometer featuring a position-sensitive detector and copper Kα source ($\lambda = 1.5418$ Å).

Size, morphology, and composition of the NCs were determined using JEOL-2010F transmission electron microscope operating at 200 kV. The specimens for transmission electron microscopy (TEM) imaging were prepared by dropping a hexane suspension of NCs on a copper grid containing carbon support film (Ted Pella, Inc). Energy dispersive X-ray spectroscopy (EDX) was used to characterize the elemental composition of the samples.

X-ray absorption spectra were collected at the Advanced Photon Source (APS) using 20-BM beamline. All dysprosium L_3-edge spectra were recorded in the fluorescence mode employing a Si (111) monochromator and a germanium detector. A rhodium-coated harmonic rejection mirror was set at 6 mrad, and the monochromator was detuned 15% CCW at 7708.9 eV. A mixture of 50 % N_2 and 50 % He gas was used as an ionization gas in the ion chamber I_0. Ultrahigh purity N_2 gas was used as an ionization gas in ion chambers I_t and I_{ref}. A cobalt metal foil was measured simultaneously in standard transmission geometry between the I_t and I_{ref} chambers which were used for energy calibration. Samples weighing ca. 30 mg were prepared by pressing the powder into Teflon washer which was then sealed with a Kapton tape. Fluorescence data was measured in a standard geometry with the samples at 45° to the incident X-ray beam, using a 13-element liquid-nitrogen-cooled germanium detector which was position 90° with respect to the incident X-ray beam.

4.2.4. Photoluminescence Measurements

PL emission spectra were recorded with a Cary Eclipse fluorescence spectrometer by exciting NC samples into the Ga_2O_3 band gap at 230 nm. For time-gated PL spectra the measurement delay time was set to 0.2 ms, detection window (gate time) to 5 ms, and the total decay window to 20 ms. PL lifetime measurements were performed using a 40 µs delay, with a gate time of 1 µs for Ga_2O_3 DAP emission and 5 µs for Dy^{3+} emission. Low temperature measurements were performed using an Oxford Instruments Optistat CF cryostat cooled with liquid helium and controlled by an Oxford Instruments ITC 5035 controller.

4.2.5. Monte Carlo Simulation

Monte Carlo simulation was performed using a sample size of 1 million excited NCs with a single excited electron per NC. This configuration was chosen to avoid the effects associated with electron interactions, which has been shown to provide a good model in the past.[36] Electrons in the conduction band could be trapped by an oxygen vacancy or Dy^{3+} dopant site, forming dysprosium excited state (Dy*), or undergo nonradiative recombination with a hole in the valence band. Electrons trapped in the aforementioned sub-band-gap states could be excited back to the conduction band, relax radiatively (characteristic DAP or Dy^{3+} intra-4f emission), or just remain trapped. Probabilities of these processes were first tuned manually to match measured temperature-dependent PL spectra and lifetime data for undoped Ga_2O_3 NCs (without Dy^{3+} trapping). Once a good agreement for undoped NC sample was achieved, the likelihood of electron trapping on Dy^{3+} site was introduced and the simulated DAP PL intensity compared to the analogous experimental data for 3.6 % Dy^{3+}:Ga_2O_3 NC sample for different temperatures. Full description of the simulation is given in Appendix C.

4.3. Results and Discussion

We prepared a series of Dy^{3+}:Ga_2O_3 NCs samples having different doping concentrations (0, 3.6, 9.2, and 13.3 %). Typical XRD patterns of colloidal Ga_2O_3 and Dy^{3+}:Ga_2O_3 NCs are shown in Figure 4.1a. Unlike bulk samples, that have monoclinic crystal structure (β phase) at room temperature, colloidal Ga_2O_3 NCs (gray trace in Figure 4.1a) are stabilized in the γ phase and exhibit a defective spinel-type structure ($Fd\overline{3}m$).[181] Detailed structural analysis and modeling have revealed that metastable γ-Ga_2O_3 has a complex structure in which Ga^{3+} cations partially occupy two pairs of octahedral (O_h) and tetrahedral (T_d) sites in the total ratio $Ga^{3+}(O_h)/Ga^{3+}(T_d) \approx$ 1.35:1.[181,35] Upon doping with Dy^{3+}, the XRD peaks broaden significantly. This broadening is mostly attributed to an increased structural disorder in the presence of dopant impurities. Under the given synthesis conditions in this work, an average size of undoped Ga_2O_3 NCs is ca. 5.5±0.4 nm (Figure 4.1b). The size of NCs decreased upon introducing Dy^{3+} to the reaction mixture (Figure 4.1c and Table C.2). The actual doping concentration for the sample in Figure 4.1c was determined to be 9.2±1.1 % using EDX elemental analysis. The doping efficiency remains similar for low to intermediate Dy^{3+} precursor concentrations, but begins to saturate at high starting concentrations of Dy^{3+} (Table C.1).
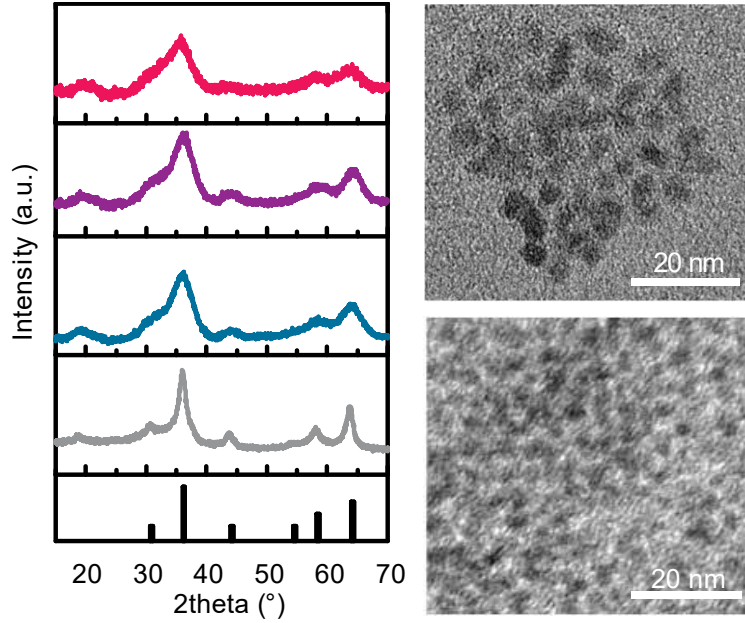
Figure 4.1. (a) XRD patterns of Dy^{3+}:Ga_2O_3 NCs having different doping concentrations as indicated in the graph. (b,c) TEM image of (b) undoped Ga_2O_3 and (c) 9.2 % Dy^{3+}:Ga_2O_3 NCs.

Figure 4.2a shows PL spectra of Dy^{3+}:Ga_2O_3 NCs having different doping concentrations, together with a spectrum of undoped Ga_2O_3 NCs, upon excitation at 230 nm (NC band edge excitation). With an increase in doping concentration the DAP emission band shifts to higher energies, suggesting a decrease in the average donor-acceptor separation.[123] This decrease in the distance between donors and acceptors is associated with an increase in the number density of oxygen vacancies with increasing Dy^{3+} doping concentration. As we discussed elsewhere,[180] the formation of oxygen vacancies can be stimulated by substitutional doping of an ion having lower ionization potential relative to the Ga^{3+},[182] which is indeed the case for Dy^{3+}. At high doping levels a weak narrow band is observed at ca. 580 nm, arising from Dy^{3+} $^4F_{9/2} \rightarrow {}^6H_{13/2}$ intra-ionic f-f transitions. Photoluminescence excitation (PLE) spectra of Dy^{3+}:Ga_2O_3 NCs are shown in Figure 4.2. The excitation spectra corresponding to Ga_2O_3 NC DAP (430 nm) and the delayed excitation spectra Dy^{3+} $^4F_{9/2} \rightarrow {}^6H_{13/2}$ (580 nm) emission are in excellent agreement, confirming a sensitization of Dy^{3+} emission by the NC host lattice. The lifetime of the DAP emission is significantly shorter than that of Dy^{3+} emission (Figure 4.2c). This difference in the PL lifetime allows for using time-gated PL spectroscopy to characterize the Dy^{3+} dopant speciation. Figure 4.2d shows time-gated PL spectra of Dy^{3+}:Ga_2O_3 NCs from Figure 4.2a, collected 0.2 ms upon termination of the excitation pulse. In addition to the strongest Dy^{3+} $^4F_{9/2} \rightarrow {}^6H_{13/2}$ peak, two other features

60

characteristic for Dy^{3+} are observed at ca. 480 nm and 675 nm which are assigned to $^4F_{9/2}{\rightarrow}^6H_{15/2}$ and $^4F_{9/2}{\rightarrow}^6H_{11/2}$ transitions, respectively. In contrast to electric-dipole $^4F_{9/2}{\rightarrow}^6H_{13/2}$ transition, $^4F_{9/2}{\rightarrow}^6H_{15/2}$ transition in magnetic dipole allowed, and its intensity is independent of the local crystal field. Hence, the branching ratio of $^4F_{9/2}{\rightarrow}^6H_{13/2}$ to $^4F_{9/2}{\rightarrow}^6H_{15/2}$ intensities can be used to gauge the Dy^{3+} site symmetry, where the dominance of the $^4F_{9/2}{\rightarrow}^6H_{13/2}$ band generally suggests a low site symmetry. This type of spectroscopic analysis for Eu-doped Ga_2O_3 NCs has demonstrated that a significant fraction of Eu^{3+} dopants substitute for octahedral Ga^{3+} sites on NC surfaces,[180] which have higher symmetry compared to bulk Ga^{3+} (O_h) sites. Given the comparable intensities of $^4F_{9/2}{\rightarrow}^6H_{13/2}$ and $^4F_{9/2}{\rightarrow}^6H_{15/2}$ bands, in the ratio that does not change significantly with increasing doping concentration, it is likely that the same phenomenon holds for Dy^{3+} dopants. The presence of Dy^{3+} in the immediate vicinity of NC surfaces is also consistent with a large discrepancy between ionic radii of Ga^{3+} (0.62 Å) and Dy^{3+} (0.91 Å).
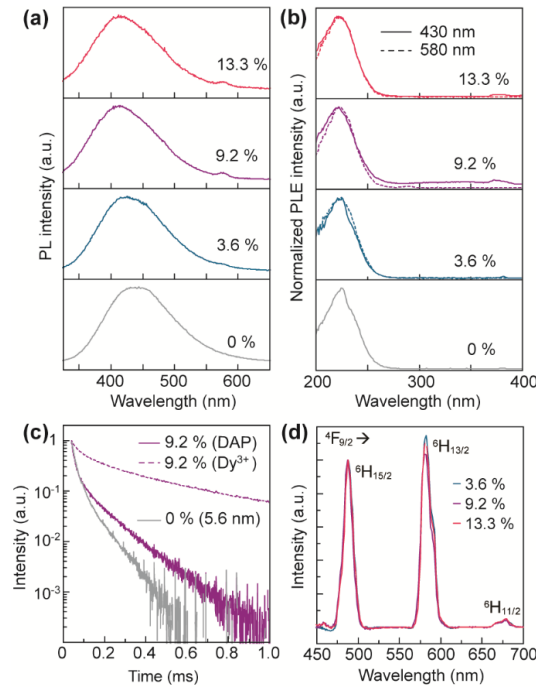
Figure 4.2. (a) PL spectra of Ga₂O₃ NCs (bottom panel) and Dy³⁺:Ga₂O₃ NCs (top three panels) having different doping concentrations, as indicated in the graph. (b) PLE spectra of NCs in (a) for Ga₂O₃ DAP emission at 430 nm (solid lines) and Dy³⁺ emission at 580 nm (dashed lines). PLE spectra for Dy³⁺ emission were collected for delayed PL. (c) Time-resolved PL intensity for 9.2 % Dy³⁺:Ga₂O₃ NCs corresponding to DAP and Dy³⁺ emission (purple lines). Time-decay DAP PL intensity for undoped Ga₂O₃ NCs having nearly identical average NC size (gray line) is shown for comparison. (d) Room temperature delayed PL spectra of Dy³⁺:Ga₂O₃ NC having different doping concentrations. Assignments of the characteristic Dy³⁺ intra-4f transitions are labeled in the graph.

To confirm these conclusions and further characterize dopant speciation in Ga_2O_3 NCs we performed X-ray absorption spectroscopy measurements (Figure C.3). Dysprosium L_3–edge X-ray absorption near-edge structure (XANES) spectra of Dy^{3+}:Ga_2O_3 NCs for different doping levels are shown in Figure 4.3a. All spectra have nearly identical structure, characteristic for Dy^{3+}, with a sharp intense peak (known as the white line) at ca. 7790 eV.[183] However, there is a significant decrease in the amplitude of the white line with increasing doping concentration. The relative intensity of the white line in L_3-edge XANES spectra has been associated with the symmetry of the absorbing ion.[184] Specifically, a decrease in the intensity of the white line has been correlated with a lower degree of local distortion. The data in Figure 4.3a suggests that increasing doping concentration results in a lower average distortion of the Dy^{3+} sites, consistent with conclusions derived from the PL spectra in Figure 4.2d. We also collected extended X-ray absorption fine structure (EXAFS) spectra of Dy^{3+}:Ga_2O_3 NCs (Figure C.4). Figure 4.3b shows the Fourier-transformed EXAFS spectra of the NC samples from Figure 4.3a. The band corresponding to the first Dy^{3+} coordination shell is shifted to larger radial distances with increasing doping concentration. These results suggest an elongation of an average Dy-O bond length due to an expansion of the NC lattice associated with the substitution of Ga^{3+} with larger Dy^{3+} cation.
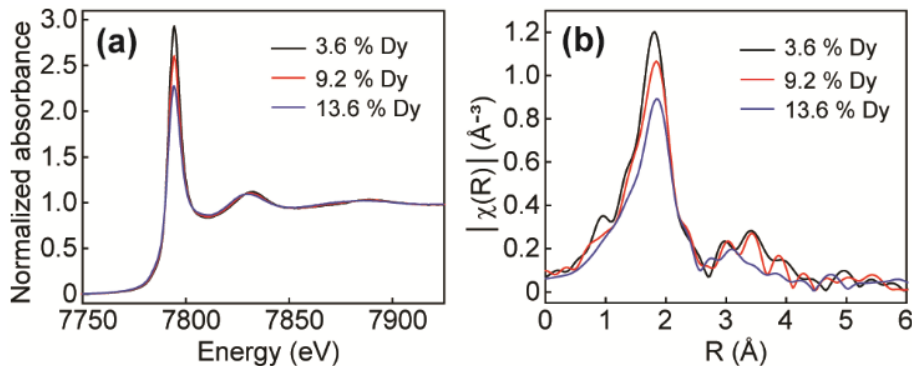
Figure 4.3. (a) XANES spectra of Dy^{3+}:Ga_2O_3 NCs having different doping concentrations, as indicated in the graph. (b) Fourier-transformed EXAFS spectra (pseudo-radial distribution functions) of Dy^{3+}:Ga_2O_3 NCs in (a).

The effect of Dy^{3+} dopants on carrier trapping and DAP afterglow was investigated by temperature-dependent PL measurements. Figure 4.4a shows PL spectra of 9.2 % Dy^{3+}:Ga_2O_3 NCs collected at different temperatures from 5 to 300 K. With increasing temperature, the DAP

band shifts to lower energy (longer wavelength) and increases in intensity. On the other hand, no shift is observed in Dy^{3+} f-f spectra, but there is a significant increase in $^4F_{9/2} \rightarrow {}^6H_{13/2}$ to $^4F_{9/2} \rightarrow {}^6H_{15/2}$ intensity ratio with increasing temperature, as evidenced from the time-gated PL spectra (Figure 4.4b). This temperature-induced change in the Dy^{3+} peak intensities is observed for other doping concentrations (Figure C.4). These results indicate a change in the local environment of Dy^{3+} dopants with increasing temperature, such that the Dy^{3+} site symmetry is effectively lowered. We believe that this is largely due to Dy^{3+} residing in the vicinity of NC surfaces. The local coordination of surface or near-surface sites is more sensitive to thermal fluctuations than the coordination of the sites buried deeper in a NC.

Figure 4.4c and d summarize the effect of temperature on the energy and intensity of the DAP luminescence (PL spectra collected at different temperatures for different Dy^{3+} doping concentrations are shown in Figure C.5). Figure 4.4c plots the DAP band maximum energy as a function of temperature ($E_{DAP}(T)$) for $Dy^{3+}:Ga_2O_3$ NC having different Dy^{3+} doping concentrations. The data are fit to Varshni's equation (solid lines in Figure 4.4c),[59] which establishes an empirical relationship between the semiconductor band gap energy and temperature:

$$E_{\mathrm{DAP}}(T) = E_{\mathrm{DAP}}(0) - \frac{\alpha T^2}{\beta + T} \qquad\qquad 4.4$$

where $E_{DAP}(0)$, α, and β are materials constants. In this case, $E_{DAP}(0)$ represents the DAP emission energy at 0 K, and is determined as a free parameter for the fits in Figure 4.4c. $E_{DAP}(0)$ increases from 3.07 to 3.23 eV by increasing the doping concentration from 0 to 9.2 %. An increase in $E_{DAP}(0)$ has been suggested to reflect a reduction in the smallest average separation between donors and acceptors in Ga_2O_3 NCs.[122] As the Dy^{3+} doping concentration increases, so does the number density of oxygen vacancies, as discussed above. Consequently, the separation between nearest donors and acceptors will also become smaller, leading to the change in $E_{DAP}(0)$.

A more intriguing and unique behavior is observed for temperature dependence of the DAP PL intensity. The DAP emission intensity dependence on temperature ($I(T)$) for $Dy^{3+}:Ga_2O_3$ NCs is related to the activation energy (ΔE) as:[21]

$$I(T) = \frac{I_0}{1 + A\exp(-\Delta E/kT)} \qquad \text{4.5}$$

where A is the pre-exponential factor and k is the Boltzmann constant. The data for undoped Ga_2O_3 NCs are fit very well with Equation 4.5 (Figure C.6). The thermal quenching of the DAP intensity is due to detrapping of the electrons bound to the donor sites. Surprisingly, upon doping a small amount of Dy^{3+} into Ga_2O_3 NCs, the thermal quenching becomes less pronounced (blue spheres in Figure 4.4d), and when doped with 9.2 % Dy, the DAP intensity even increases with temperature (purple spheres in Figure 4.4d). This phenomenon can be explained by thermal reactivation of carriers trapped in shallow Dy^{3+} states. With increasing temperature electrons trapped on Dy^{3+} can be thermally promoted to the conduction band, forcing their subsequent trapping on the oxygen vacancies and eventual radiative relaxation through the DAP mechanism. These results also suggest that Dy^{3+} trap states are shallower than the trap states originating from oxygen vacancies, allowing for a slow transfer of electrons from Dy^{3+} to the donor sites via conduction band delocalization. Importantly, it should be mentioned that this delay in electron trapping on the donor sites has a larger effect on the afterglow than the above mentioned decrease in the average donor-acceptor separation induced by Dy^{3+} dopants.
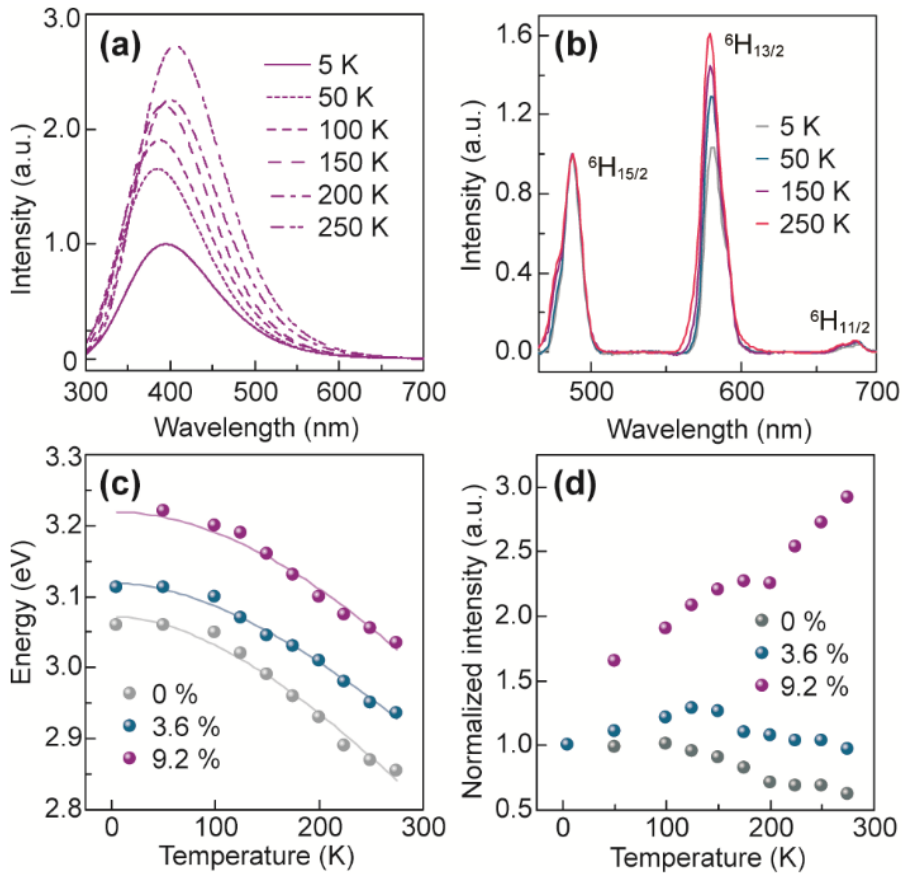
Figure 4.4. (a) PL spectra of 9.2 % Dy^{3+}: Ga_2O_3 NCs collected at different temperatures, as shown in the inset. (b) Delayed PL spectra of 9.2 % Dy^{3+}:Ga_2O_3 NCs collected at different temperatures, as shown in the inset. The spectra were normalized to the Dy^{3+} $^4F_{9/2} \rightarrow ^6H_{15/2}$ transition. (c) Temperature dependence of the relative PL intensity for Dy^{3+}: Ga_2O_3 NCs having different doping concentrations, as shown in the inset. (d) Temperature dependence of the DAP PL band maximum energy for Dy^{3+}: Ga_2O_3 NCs having different doping concentration, as shown in the inset.

Figure 4.5 compares the PL lifetime data for Ga_2O_3 and Dy^{3+}:Ga_2O_3 NCs at 5 K (Figure 4.5a) and 300 K (Figure 4.5b). At low temperatures Dy^{3+}:Ga_2O_3 NCs have a shorter PL lifetime, indicating a smaller electron tunneling distance, which is consistent with a smaller average separation between donors and acceptors. However, at room temperature, the presence of Dy^{3+} dopant centers extends significantly the DAP afterglow. These results suggest that excited electrons in the conduction band are trapped in metastable long-lived Dy^{3+} states, delaying their trapping on the donor sites and a subsequent DAP recombination.
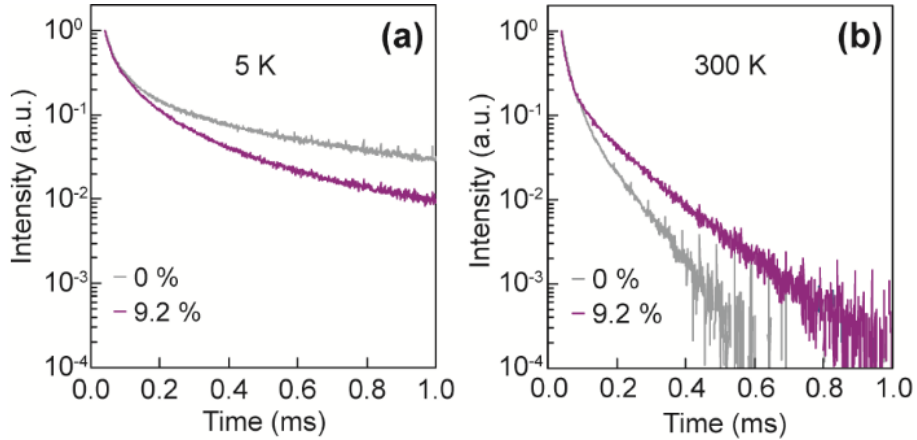
Figure 4.5. Time-resolved DAP PL intensity data for typical Ga₂O₃ NCs and 9.2 % Dy³⁺:Ga₂O₃ NCs having similar average NC sizes, collected at (a) 5 K and (b) 300 K.

To test this hypothesis we designed a Monte Carlo simulation based on a simple kinetic model (see Experimental and Theoretical Methods, and Appendix C for details). In this model an electron generated in the conduction band upon NC excitation could be trapped in the Dy^{3+} excited state (Dy*) or an oxygen-vacancy-based donor state (D), relax non-radiatively to the valance band, or remain in the conduction band. Electrons in Dy* and D states could relax radiatively, be excited back to the conduction band or remain in the excited state (Figure 4.6a).

The probability of thermal activation of the electrons in trap states (Dy* and D (V_O^x)) is determined by trap depth (i.e., probability that an electron can overcome the energy gap between the trap state and the conduction band minimum), and the probability of the temperature dependent DAP tunnel transfer is described by Equation 3 (Figure C.6 and the associated discussion in Appendix C). Comparative simulation of the relative DAP PL intensities with respect to temperature for Ga_2O_3 and $Dy^{3+}:Ga_2O_3$ is shown in Figure 4.6b. Even though this is a relatively simplistic model, the simulation results and the experimental data are in a very good agreement. The results of Figure 4.6 further suggest that a smaller depth of Dy* relative to the depth of Ga_2O_3 donor states ($V_O^{\bullet}$) causes an increase in electron flow to $V_O^{\bullet}$ as the primary trap. This process results in an increase in DAP emission intensity with increasing temperature (see also Figure 4.4d) until detrapping of the electrons from the deeper primary trap states becomes significant. Further increase in temperature causes a decrease in DAP emission intensity.
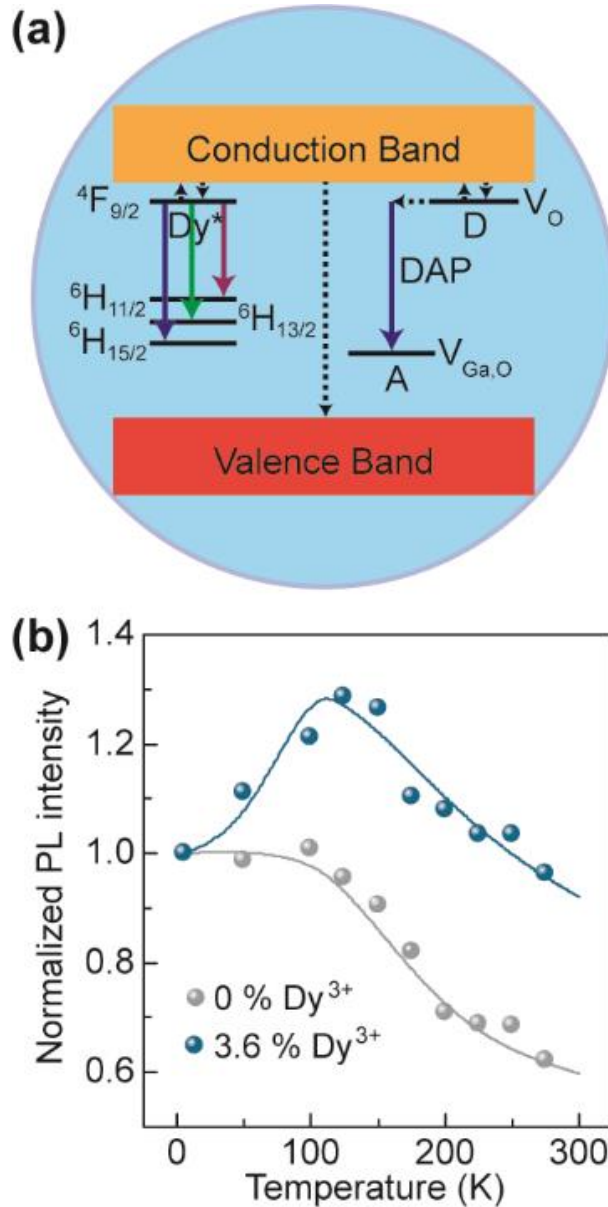
Figure 4.6. (a) Schematic presentation of the electron pathways in $Dy^{3+}:Ga_2O_3$ NCs used in Monte Carlo simulations. Dashed lines indicate non-radiative electron pathways (relaxation, trapping, or transfer), and solid lines indicate observed PL processes. (b) Temperature dependent PL intensities for 0 % and 3.6 % $Dy^{3+}:Ga_2O_3$ NCs. Solid lines represent Monte Carlo simulated results.

4.4. Conclusions

In summary, we synthesized colloidal Dy^{3+}-doped Ga_2O_3 NCs, and explored the effect of Dy^{3+} dopants on the PL properties of the NC host lattice. Based on structural characterization and steady-state PL measurements we proposed that a majority of Dy^{3+} dopants are located on NC surfaces and lead to an increased concentration of oxygen vacancies relative to undoped Ga_2O_3

NCs. Surprisingly, in contrast to undoped Ga_2O_3 NCs, Dy^{3+}-doped Ga_2O_3 NCs exhibit an enhancement in the DAP PL intensity with temperature upon NC excitation into the band gap, which is attributed to the thermal reactivation of electrons kinetically trapped in shallow Dy^{3+} states. This trapping is also responsible for an extension of the Ga_2O_3 DAP emission lifetime at room temperature. Using a kinetic Monte Carlo simulation based on the probability of different electron pathways, we demonstrated that a smaller activation energy of Dy^{3+} trap states relative to oxygen-vacancy-based donor states in Ga_2O_3 NCs leads to a controlled release of electrons from Dy^{3+} and their subsequent capture by $V_O^{\bullet}$ sites. This process results in a delayed DAP emission, despite a decrease in the average donor-acceptor separation caused by the Dy^{3+} incorporation. The results of this work demonstrate the mechanism of generating or extending afterglow in luminescent NCs that are only a few nanometers in size, and could allow for the design and preparation of nanophosphors with persistent luminescence.

Chapter 5. Inorganic Phosphors for Teaching a Holistic Approach to Functional Materials Investigation[3]

Inorganic phosphors are the main component of light emitting diodes which have caused the revolution in lighting industry as an energy-efficient and long-lasting replacement of traditional incandescent light bulbs and fluorescent tubes. They are also used in various consumer products and displays and can potentially find applications in photocatalysis, solar cells, optical thermometers, and stress indicators. Long-afterglow phosphors provide an opportunity to visually observe and test different phenomena in solid-state materials and can be used as an effective teaching tool at the undergraduate level. We developed an upper-level undergraduate laboratory experiment that integrates the synthesis, processing, structural and spectroscopic characterization, and applications of strontium–aluminate-based phosphors. Observation of the intensity and duration of the phosphor afterglow under different conditions reinforces students' learning of various concepts related to materials structure and properties, and spectroscopic principles, in an engaging and impactful way. The phenomena of thermoluminescence and mechanoluminescence, and their potential applications in thermal sensors and ballistics, respectively, are also introduced. Depending on the instructor's goals, the described laboratory experiment can be used in a modified form in inorganic or physical chemistry laboratory courses, but we believe it is particularly well-suited as a module for advanced laboratory courses in interdisciplinary programs.

5.1. Introduction

Functional optical materials have become an important part of different industries and a focus of significant fundamental research.[185] Incorporation of the topics on functional optical materials into chemistry curriculum requires an interdisciplinary approach and the development

---

of laboratory experiments and demonstrations that are both engaging and educational. Luminescent materials offer an opportunity to introduce undergraduate students to this broad class of functional materials, while providing a vehicle for hands-on learning about materials synthesis and characterization, electronic structure and spectroscopy, and surface chemistry, as well as relevant "real world" applications. Solid-state inorganic phosphors are widely used in our daily lives, with the applications ranging from consumer products such as decorating stickers, glow-in-the-dark toys, and wristwatch displays, to safety and security signs, optical thermometers, probes in bioimaging and molecular sensing, and general lighting sources (compact fluorescent lamps and light emitting diodes).[135,142] Phosphors are often characterized by long afterglow, which allows the students to visualize the performance of these materials in real time and gain an intuitive understanding of their properties, while offering the instructors an opportunity to be creative in designing the laboratory experiments.

The phenomenon of luminescence, i.e., the emission of a photon of light, occurs when an electron in an excited electronic state relaxes to a lower state.[96] Typically, at room temperature, electrons of most compounds are in their ground state. However, these electrons can be promoted to the excited state upon absorption of photons of specific energies. Strictly speaking, there are two types of luminescent materials: (i) fluorescent materials, which emit almost immediately (typically a few nanoseconds) after excitation, and (ii) phosphorescent materials, which continue to emit for a long time (milliseconds to hours) after initial excitation. In typical phosphorescent molecules, the slow relaxation of the excited states is associated with the transformation of the excited electron to a triplet state by a process known as intersystem crossing, which can then return to the ground state only via a quantum mechanically "spin-forbidden" transition.[96] By contrast, in solid-state phosphors which are a subject of this Laboratory Experiment, the afterglow occurs because charge carriers become trapped in a state that energetically prevents (or delays) its immediate relaxation to a lower energy state.[151]

The electronic structure of solid-state materials is typically represented by the valence and conduction bands separated by a band gap. Dopants are small amounts of impurity elements that, depending on their nature, can introduce energy levels into the band gap. Excited electrons in the conduction band are mobile and can relax into a trap state created by a dopant. From there, electrons may be re-excited into the conduction band, or relaxed into a lower energy trap or back

70

into the valence band. Photons produced by the electrons relaxing from a trap within the band gap into the valence band are red-shifted relative to the initial excitation wavelength of light. Traditionally, afterglow phosphors have been primarily based on zinc sulfide.[186,187] Although widely used, zinc sulfide phosphors have some significant drawbacks such as being sensitive to moisture, as well as only maintaining its glow for relatively short periods of time (tens of minutes) in the dark. A class of materials that promises major improvements over zinc-sulfide-based phosphors are metal aluminates doped with lanthanide ions. Of these doped metal aluminates, a particularly popular phosphor is strontium aluminate ($SrAl_2O_4$) doped with europium and dysprosium ($SrAl_2O_4$:Eu,Dy or SAED).[48] The advantages that SAED has over other phosphor materials are that it is chemically inert, maintains its glow for tens of hours in the dark, and is relatively nontoxic.

In the $SrAl_2O_4$:Eu,Dy system, Eu^{2+} and Dy^{3+} dopants substitute Sr^{2+} sites in the crystal structure and become traps for excited electrons.[151] Eu^{2+} dopants form traps from which electrons can relax and which are responsible for the phosphor emission, while Dy^{3+} dopants provide traps that hold excited electrons, thereby delaying luminescence. The various pathways of excited electrons in $SrAl_2O_4$:Eu and $SrAl_2O_4$:Eu,Dy phosphors are illustrated in Figure 5.1. Upon excitation by an appropriate wavelength of light, an electron is promoted from the valence band to the conduction band. In the wake of the excitation, a positively charged hole is created in the valence band. Once in the conduction band, the electron is free to migrate throughout the crystal lattice, thus allowing it to encounter a dopant trap. Upon falling into a Eu^{2+} trap, the electron can recombine with a hole, thereby emitting a photon of light resulting from parity-allowed (or Laporte-allowed) Eu^{2+} $4f_6^5d_1 \rightarrow {}^4f_7$ intraionic transition (Figure 5.1, left panel). The Laporte selection rule for electric-dipole transitions states that in centrosymmetric molecules formally allowed transitions are those that involve a change in parity (g↔u). For lanthanide ions it practically means that in ideally octahedral coordination f–f transitions do not change parity and thus are formally forbidden, while d–f transitions are g↔u, giving rise to strong emission intensity. More details regarding the spectroscopy selection rules relevant for this Laboratory Experiment are given in the Appendix D instructor materials.
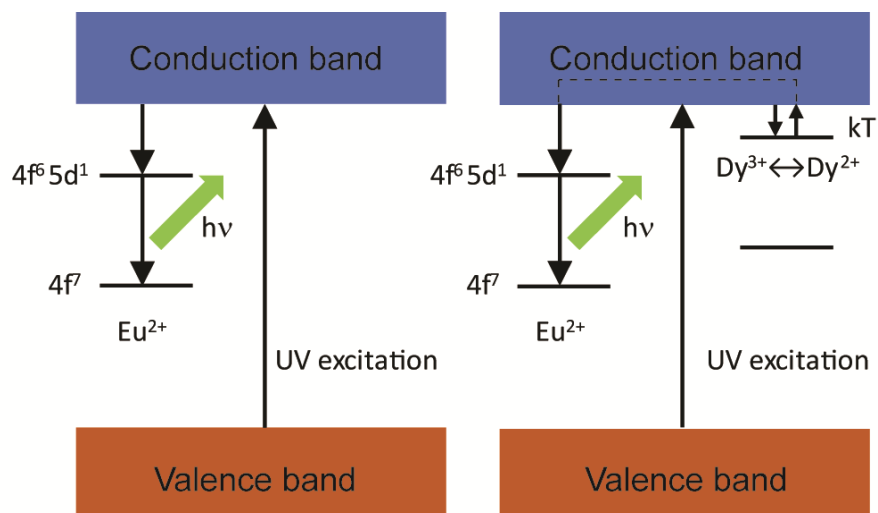
Figure 5.1. Schematic representation of the energy levels and electron trapping pathways (dynamics) in SrAl$_2$O$_4$ doped with Eu^{2+} (left panel) and SrAl$_2$O$_4$ co-doped with Eu^{2+} and Dy^{3+} (right panel).

Other electrons in the conduction band can encounter Dy^{3+} traps, which hold the electrons and prevent them from further movement or relaxation. An electron locked in a Dy^{3+} trap can only escape by being re-excited thermally back into the conduction band. From there, the electron can be trapped by an Eu^{2+} and finally recombine with its counterpart hole (Figure 5.1, right panel). Thus, it is the presence of Dy^{3+} in SAED that facilitates the delayed photoluminescence (or afterglow) effect. The ability of SrAl$_2$O$_4$:Eu,Dy to store energy and release it over a long period of time in the form of light emission has found many interesting applications beyond glow-in-the-dark displays.[142] Examples include solar cells and photocatalysis, in which SrAl$_2$O$_4$:Eu,Dy can continue to provide a source of lighting to an active component (light converter or photocatalyst) even when sunlight is not available due to the weather conditions or time of day. One of the lesser known properties of SrAl$_2$O$_4$:Eu,Dy phosphors is that their emission can also be caused by a mechanical force as a source of excitation, a phenomenon known as mechanoluminescence. Upon subjecting a SAED phosphor to a mechanical stress force, the trap depth is reduced such that the rate of electron detrapping increases. Empirically, this was found to result in a linear relationship between mechanluminescence intensity and impact force per unit area (pressure).[188]

Previously reported undergraduate educational activities involving phosphor materials have focused mostly on copper-doped zinc sulfide,[186,189,190] with the goal of visually demonstrating luminescence mechanism or teaching the kinetic models using afterglow. The

72

laboratory experiments on $SrAl_2O_4$:Eu,Dy phosphors reported in J. Chem. Educ. are based on the synthesis and structural characterization of the obtained products,[191] and basic photoluminescence measurements.[192] We designed and implemented a new laboratory experiment that encompasses the synthesis of $SrAl_2O_4$:Eu,Dy phosphor using a range of materials synthesis and processing techniques, comprehensive materials characterization, spectroscopy, and application in ballistics and thermal imaging. The purpose of this Laboratory Experiment is to enable students to develop a comprehensive approach to materials chemistry research that would stimulate their interest, creativity, and engagement, and enhance learning outcomes.

5.2. Learning Outcomes

This Laboratory Experiment was designed to maximize the impact on students' knowledge and skills, while simultaneously providing students with a comprehensive and enjoyable laboratory experience. The pedagogical goals of this Laboratory Experiment are as follows:

- To develop conceptual understanding of different methods used for the synthesis of inorganic solid-state materials, including solution-phase preparation and processing, high-temperature combustion, and solid-state reactions in a controlled atmosphere;
- To become familiar with standard materials characterization tools and develop the ability to critically evaluate materials structure and properties;
- To improve practical understanding of the electronic structure of solid-state materials and the experimental techniques used for its investigation;
- To understand the role of dopants in modifying the electronic structure and photoluminescence properties of solid-state materials and to be able to distinguish the luminescence mechanisms in different systems;
- To gain the concept of carrier dynamics in solid-state materials and its importance in defining the optical and/or electrical properties of materials;
- To learn about thermoluminescence and mechanoluminescence, as lesser known properties of phosphor materials, and gain exposure to interesting practical applications of these phenomena.

5.3. Experimental Overview

This Laboratory Experiment has been run as one of the modules in the third-year undergraduate Materials Laboratory course in the Nanotechnology Engineering program at the University of Waterloo (NE 320L). It is also suitable for solid-state materials chemistry, physical chemistry, or even inorganic chemistry laboratory courses. Approximately 90 students are enrolled in the course each year. The experiment is performed in groups of four students, who are in the same session with two other groups doing different experiments. Each group of four students is supervised by one Teaching Assistant (TA) and receives on average a third of the instructor's time during the session. In this organization, two TAs and the instructor are involved in running this Laboratory Experiment for 90 students. The experiment is divided into two 3 h weekly sessions. The first session is dedicated to the $SrAl_2O_4$:Eu,Dy synthesis, processing, and observation of photoluminescence, and the second session, to materials characterization and quantitative measurements of the ballistic force using the samples prepared in the first session (see Appendix D files for more detail). Because the topics investigated in this experiment are likely to receive limited attention in courses preceding this lab, the in-lab discussions in the first session focused on the theory behind thermoluminescence and mechanoluminescence followed by the students applying that knowledge to their analysis during the second session. Template reports (see Appendix D instructor materials) were filled out individually by each student and submitted electronically 3 days after the second lab session.

5.4. Experimental

5.4.1. Procedures

All precursors and solvents for this Laboratory Experiment were used as received without further purification. Two samples were prepared in parallel by students, one for further treatment by annealing (referred to as "annealed" sample) and the other one for comparison (referred to as "crude" sample). The experiment is organized such that one pair of students prepares the crude sample while the other prepares the annealed sample. The annealing is performed in a flow of nitrogen and hydrogen gases. The students subsequently characterized both samples by scanning electron microscopy (SEM) and powder X-ray diffraction (XRD). Proper SEM imaging technique was demonstrated for the students by the instructor, after which they were given the opportunity to capture images of their samples. The students were required to match the results

of the acquired XRD patterns and identify the obtained material. For mechanoluminescence measurements, the samples were excited using a projectile launcher, and the luminescence signal was measured with a photodetector. The experimental procedures are described in detail in the instructor notes in Appendix D.

5.4.2. Hazards

Before the laboratory session, the students must complete a prelab safety questionnaire to demonstrate the awareness of potential hazards and precautions (see Appendix D instructor materials). As with any upper-level chemistry lab, wearing standard personal protective equipment such as lab coats, safety glasses, and appropriate clothing and footwear is required. Whenever handling the precursors or products, students are required to wear impermeable gloves. In consideration of any potential exhaust fumes, both the high-temperature furnace and tube furnace were located inside the fume hoods. Insertion and removal of sample vials from the furnaces required the use of long metal tongs. Handling of the hot fused silica tube after annealing requires students to wear protective heat resistant gloves. Hydrogen gas, being in compressed form and extremely flammable, should be handled with great care. As with all gas cylinders, the hydrogen gas cylinder needs to be fixed either to the wall or a bench to prevent it from tipping over. For additional instructor notes on safety see Appendix D.

5.5. Results and Discussion

Prior to the first session, students were required to complete a prelab assignment that asks them to calculate the stoichiometric amounts of all metal nitrate precursors needed to prepare $SrAl_2O_4$ co-doped with 1% Eu^{2+} and 2% Dy^{3+}, including a 50 mol % excess of urea to ensure that the reaction proceeds to completion. In addition to calculating the amounts to be weighed, students are asked questions in the prelab assignment regarding the role of the dopants and annealing to ensure key concepts are understood prior to coming into the lab.

The prepared samples glow green or red depending on whether or not they were annealed under hydrogen. The origin of this luminescence is from the Eu^{x+} (x = 2 or 3) ions,[105,193] whose luminescence in $SrAl_2O_4$ lattice is well-documented. All annealed samples display some level of delayed luminescence from the slow release of trapped carriers. There is some disagreement in the literature about the true nature of the trap states, with Dy^{3+} originally thought to be a hole

trap.[48] More recently, trap states have been associated with oxygen vacancies, because some delayed luminescence is still observed in this system without Dy^{3+} as a dopant.[50,52,168] In this Laboratory Experiment we reference the mechanism proposed by Dorenbos (Figure 5.1),[53] where Dy^{3+} acts as an electron trap, because it provides the simplest introduction to the principles of persistent luminescence and trapping. This allows the students to focus on the broader implications of this experiment as opposed to worrying about quasi particles or oxygen vacancy states.

During the first session, students observe the photoluminescence of the crude and annealed samples under a hand-held UV lamp in a dark room (Figure 5.2). As they contrast the weak red emission of their crude samples with the strong green emission of their annealed samples (Figure 5.2b), they are asked to recall the purpose of the annealing process, i.e., the reduction of Eu^{3+} to Eu^{2+}, which they had answered in the prelab assignment. In addition to the emission color, the students are asked to comment on the time in which the glow visually disappears after the UV lamp has been switched off (Figure 5.2c). Since their annealed samples all cease to luminesce after a few minutes, the students were then led, using targeted questioning by the TA, to the conclusion that the crystal lattice structure was still less than optimal and that this product deficiency is associated with the limitations in annealing time and temperature.
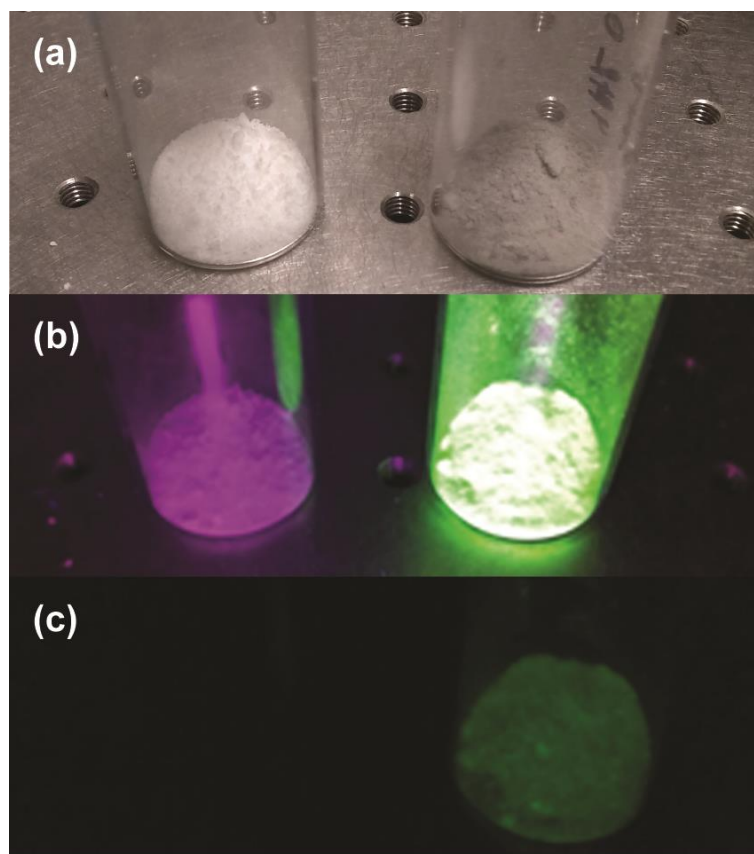
Figure 5.2. Photographs of SrAl₂O₄:Eu,Dy samples before (left vials) and after (right vials) annealing in hydrogen atmosphere. (a) Isolated samples in powder form. (b) Samples in dark under excitation by UV lamp. (c) Samples in dark 1 min after turning off the UV lamp.

Although a red emission characteristic for Eu^{3+} (f–f transitions) was observed in the crude samples, it was weak and showed no signs of afterglow. Annealed samples showed a stronger green emission that is characteristic for Eu^{2+} (d–f transitions). This observation serves as an excellent vehicle to remind students about the spectroscopic selection rules, and particularly that allowed transitions must involve a change in parity (Laporte selection rule).[105,193] The annealed samples retained their emission for well over 1 min. The lifetime of emission follows the Arrhenius-type equation:

$$\tau = s^{-1}e^{-E/k_BT} \qquad\qquad 5.1$$

where (E) is the trap depth, (kB) and (T) are the Boltzmann constant and temperature, respectively, and (s) is the frequency factor. According to Matsuzawa et al.,[48] the trap depth for SrAl₂O₄:Eu,Dy is 0.65 eV, which is considered ideal for room temperature delayed luminescence

applications. The most intuitive way to explain the frequency factor to the students is that it represents a number of times per second that a trapped electron will attempt to escape the trapping site. Consequently, the students come to the realization that Equation 3.1 represents a product of the electron escape (detrapping) time and the probability that an escape event will be successful. The frequency factor depends on the environment of the trapping site. Poorer crystal quality, higher doping concentration, or both yield a larger frequency factor. Combustion synthesis is a high-throughput method, which yields the best crystal quality when annealed at 1400 °C for at least 4 h. Since the samples made in this lab are not annealed to this extent (1000 °C for 1 h, because of the equipment and time constraints), the frequency factor will be significantly higher than for commercial SAED made through the combustion or solid-state syntheses. Crystal quality will also have a direct effect on the brightness of the emission due to the presence of nonradiative defects in the crystal lattice. These issues are discussed with the students in the prelab and during the lab session.

Luminescent intensity of these $SrAl_2O_4$:Eu,Dy systems is strongly dependent on temperature. The thermoluminescent intensity of materials also carries an exponential dependence on temperature:

$$I = Ce^{-E/k_BT} \hspace{3cm} \textit{5.2}$$

where (*C*) is a temperature normalizing factor. At the end of the first session, the students also explored the effect of temperature on the photoluminescence. Using a vinyl sheet embedded with $SrAl_2O_4$:Eu,Dy, students induced the film to glow using a hand-held UV lamp. They subsequently placed their hands or a beaker with warm tap water onto the film to warm up a specific area. When the object was removed, they could observe its silhouette glowing brighter than the rest of the film (Figure 5.3), demonstrating the sensitivity to thermal excitation and thus introducing them to the aspect of thermoluminescence.[168]
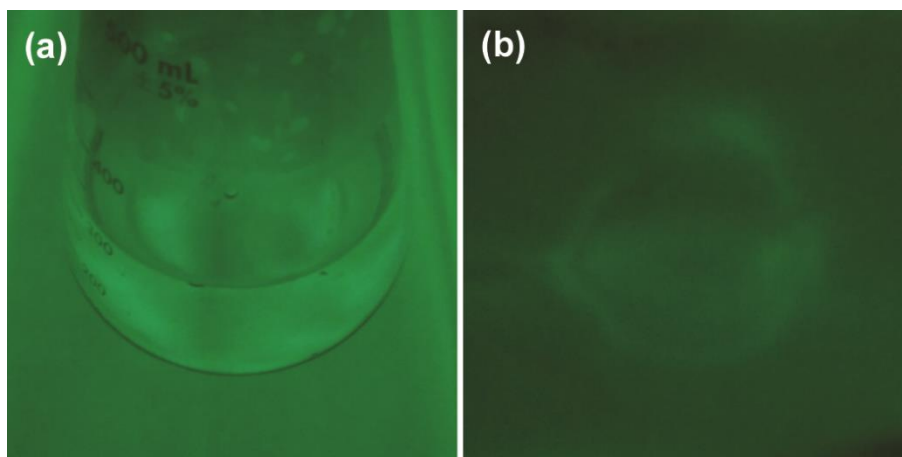
Figure 5.3. Photographs of phosphorescing vinyl sheet embedded with $SrAl_2O_4$:Eu,Dy (a) immediately upon placing a beaker with warm water onto the sheet and (b) upon removing the beaker after allowing the sheet to heat up locally.

In the second session, students prepared their crude and annealed samples for characterization by XRD and SEM. After obtaining the diffraction patterns for both samples, students were asked to search the database for matches. To refine their search, students were asked to deduce what elements should be used to search for the crystal structure match. The most common error made by students was to assume that the low concentrations of Eu and Dy would be observable in the diffraction patterns. In addition to characterizing the crystallinity of their samples, XRD measurements also allow students to gain understanding of the difference between doping, alloying, and the formation of a new compound. The crude and annealed diffraction patterns measured by students (provided in the Appendix D instructor materials) often differ significantly. Crude samples may show the presence of unreacted $Sr(NO_3)_2$, while annealed samples were mostly composed of $SrAl_2O_4$ with a secondary phase of $Sr_2Al_2O_6$. Thus, the XRD patterns enabled the students to reaffirm that the purpose of annealing was achieved.

After giving the students a 30 min re-introduction to the SEM (they would have already received some training on that exact microscope in an earlier course), covering sample preparation, troubleshooting, and fine-tuning of measurement parameters, they were given free rein to collect images of their samples (see Appendix D instructor materials for representative images). Students found that both crude and annealed samples had a large degree of agglomeration, but they were able to isolate and image individual particles at the nanoscale.

The mechanoluminescence experiment was subsequently added to the second session of this Laboratory Experiment and has so far been successfully performed by 50 students who have taken this course. The setup for this experiment is shown in Figure 5.4. In this class of materials mechanoluminescence occurs because of the piezoelectric bending of the band structure of $SrAl_2O_4$.[188] When a ball bearing strikes a sample, the activation energy referred to in Equation s 5.1 and 5.2 is reduced, allowing thermal energy to drive the electron detrapping at a noticeably higher rate. Owing to the nature of a projectile, the pressure felt by the samples is alleviated within 0.1 s, and the sample showed a brief flash as opposed to a long-lasting glow. The mechanoluminescence intensity (I) has been empirically shown to be linearly dependent on projectile velocity (v):[53]

$$I = I_0 + kv \hspace{4cm} 5.3$$

where the kinetic energy can be determined using Newton's laws. In this experiment ball bearings used as projectiles were approximately 20 g and fired at a speed between 3.5 and 7 m/s. The observed mechanoluminescent emission typically shows a strong linear dependence ($\langle R^2 \rangle =$ 0.91 ± 0.08) on the projectile velocity (Figure 5.5). The standard deviation of the slope (k) of the detector response versus muzzle velocity of the projectile was 8%, which can be explained by minor differences in compound stoichiometry and crystal quality. It should be noted that a number of student groups found a negative y-axis intercept (I_0) for many of these fitting lines (Figure 5.5). With some guidance, the students were able to reason that this was likely due to a ball-bearing speed threshold required to induce sufficient band distortion to observe emission. A linear increase is only seen once a certain minimum band displacement is experienced by a sample. It is more intuitive to consider the x-axis intercept in Figure 5.5, which reveals the amount of energy required to reach the limit of detection. The standard deviation of this intercept is ca. 21%.
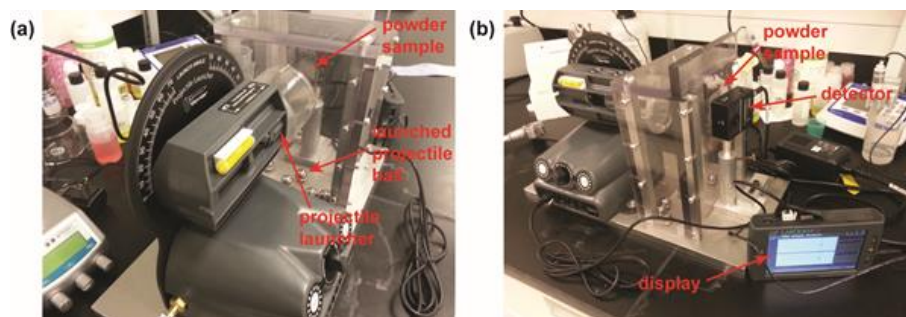
Figure 5.4. Photographs of the mechanoluminescence setup showing views from two different angles: (a) facing the powder SrAl$_2$O$_4$:Eu,Dy sample attached to the transparent screen and (b) behind the screen. The key components of the setup are shown with red arrows.
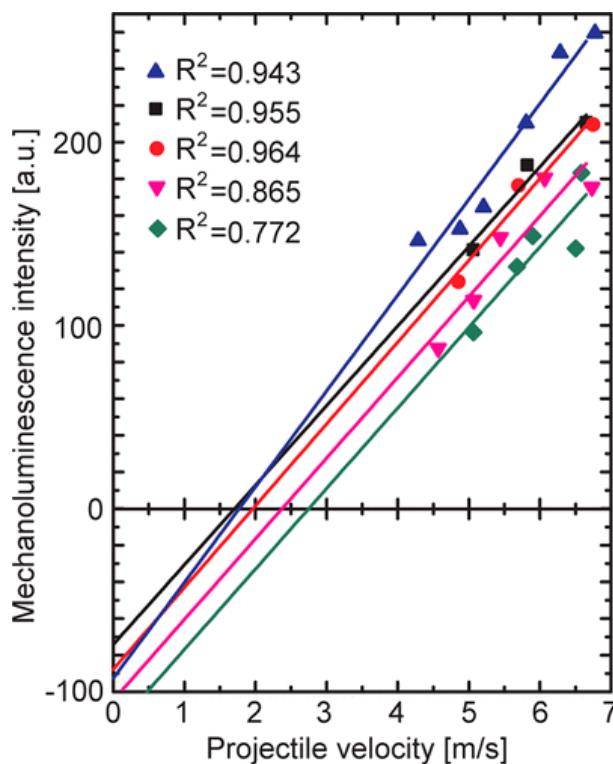
Figure 5.5. Dependence of the mechanoluminescence intensity on the projectile velocity. Different symbols show experimental data collected by different student groups, demonstrating measurement reproducibility. Coefficients of determination (R^2) for the linear fits are shown in the inset.

5.6. Assessment of Teaching Objectives

After the second lab session is completed, students were required to fill out and submit a lab report template within 3 days thenceforth. The questions asked in the report were based on the observations and analyses gained from the two sessions. Specifically, many of the concepts that they needed to reason out during the sessions, such as the differences in composition between crude and annealed samples, the effect of temperature on the photoluminescence, and so

on, were asked in the template report. This helped further reinforce the concepts learned. The lab report was graded by the assigned TA. Depending on the focus of a particular laboratory course, the versatility of this exercise allows for testing of a variety of other concepts in the lab report, including general spectroscopic principles and selection rules, point defects and discrete electronic states in solid-state materials, or even the use of mechanoluminescence to investigate classical mechanics and object velocity. The experiment garnered significant attention from students, who would often enter the lab excited from their peers' description of the content and results. A feedback from the students in the program suggests that they generally like laboratory experiments where fast-occurring dynamic processes can be observed and measured. In that context, the introduction of mechanoluminescence and its practical application for pressure sensors and ballistics increased the students' interest, learning motivation, and appreciation of this laboratory exercise.

Although the brightness of the prepared phosphors can vary among the groups, all students over the 2 year period obtained an observable afterglow. The average score for all students on the prelab exercise is 80%, and on the final report 72%, which are reasonable scores given the overall complexity of this Laboratory Experiment.

5.7. Conclusion

In summary, we designed the upper-level undergraduate integrated materials chemistry Laboratory Experiment based on the synthesis, characterization, properties, and applications of $SrAl_2O_4$:Eu,Dy phosphor having prolonged afterglow. The experiment covers the full cycle of materials chemistry research, from synthesis and processing, via structural and spectroscopic characterization and evaluation, to innovative applications. The exercise is designed to allow students to build practical knowledge and gain a range of hands-on experiences in this important area of chemistry. In addition to performing materials synthesis involving both solution and solid-state methods, this Laboratory Experiment allows students to develop an intuitive connection between materials processing and their properties. By using luminescent phosphors as the focus of investigation, the structure–property correlation and the spectroscopic selection rules can be effectively demonstrated through visual observation of the glow, allowing students to review and discuss many concepts they learned in inorganic and/or physical chemistry courses. The ability to directly and visually observe the properties of the obtained product can

serve as a vehicle to introduce interesting, unique, and engaging applications. This was realized by demonstrating the use of mechanoluminescence and theromoluminescence, which are typically not covered in undergraduate laboratory courses, in ballistics and thermal imaging, respectively.

5.8. Additional Information

Additional information for isntructors provided in Appendix D to provide additional context for this experiment. This information includes a more detailed procedure, materials used to test students understanding of lab concept and safety, and some example student data for XRD and SEM.

Chapter 6. Conclusions and Perspective

Semiconducting NCs are of particular interest for many functional applications because of their intrinsic tunability. Both the emission and absorption spectra of many NCs are able to be modified because of either quantum confinement or changes in native defect structure. Gallium oxide is a large bandgap semiconductor (~4.9 eV) which typically has a broad blue-green emission resulting from oxygen vacancies, making it interesting for a variety of photonic applications explored in this thesis. Gallium oxide NCs were linked to CdSe/CdS quantum dots by an organic molecule, thioglycolic acid, to achieve FRET in solution. Building on these results, complex solutions of these nanoparticles were deposited on glass substrates by drop-casting to make a near homogeneous film that undergoes FRET by virtue of the packing density of the NCs. To further realize the usefulness of Ga_2O_3 as a primary fluorophore, Ga_2O_3 was doped with Dy^{3+}, which resulted in the extension of the luminescent lifetime at room temperature and an increase in the emission intensity of Ga_2O_3 between 50 K and 200 K. Meanwhile, the expertise gained through these experiments was practically applied in the classroom of NE 320L laboratory course, where students synthesized $SrAl_2O_4$ nanoparticles, which were analyzed visually, by SEM, XRD and by a mechanoluminescence set-up that was built in house.

In this thesis I built upon the research that has previously been performed in this lab in which gallium oxide NCs were functionalized with organic dyes such as rhodamine B or Atto 590. In these cases when a hybrid nanoparticle conjugate was deposited on a glass substrate or a UV LED used to excite the remote phosphor, the dye emission could be impacted by its thermal stability. In my work, I used CdSe/CdS core-shell quantum dots as the orange-red component to generate white light with a comparable color rendering index to the previously formed nanocrystal-organic dye complexes, but with lower FRET efficiency (max ~30 % vs. max ~50 %) because of the exceptionally strong emission of CdSe/CdS QDs. Unfortunately, as can be seen in Figure 2.4 there was some issue with the quenching of our gallium oxide and cadmium selenide that was not seen in the previous dye samples. This is likely caused by the nature of ligand that we use in this study.

Combining nanoparticles in a film also proved to make the creation of these LED type devices easier and brighter. Our lab is not well prepared to perform high-quality device fabrication, but the robustness of the materials used was showcased in Chapter 3. The framework

explored in Chapter 3 has the possibility to produce high-quality white light with targeted characteristics, but it would best to attempt this approach with materials that are naturally more emissive than Ga_2O_3. Zinc oxide has been shown to have a similarly strong, broad, blue-green emission, and excitation that occurs in the mid-to-near-UV as opposed to being optimally excited at 230-250 nm. That being said, ZnO was the first material that we attempted to use for conjugation, but its emission was strongly quenched by the thiol in our linkers, while Ga_2O_3 immediately showed promising results. While Ga_2O_3 LEDs may not yet be commercially viable, the design of all-inorganic quasi-single white light emitting nanophosphors with tunable lighting parameters has significant fundamental and practical importance. The results of this research are generally applicable and can serve as a guideline for the preparation of other composite systems with optimal properties for various niche applications, including health and agricultural lighting.

Donor-acceptor pair recombination in Ga_2O_3 has a long photoluminescent lifetime compared other emissive NCs because trapped electrons must tunnel to the acceptor for recombination to occur, however, on an absolute scale, a lifetime of 20 µs is shorter than humans can perceive. Gallium oxide NCs were doped with Dy^{3+} in an attempt to further extend the lifetime of these NCs to a range where we would be able to develop additional uses for this material. The introduction of Dy^{3+} into the Ga_2O_3 lattice resulted in a decrease of the average donor acceptor separation which caused a blueshift of the DAP emission. The decrease in donor acceptor separation is usually associated with a decrease in luminescent lifetime, however, we observed an extension of the lifetime of doped NCs at room temperature. This counterintuitive effect of doping makes this lifetime extension more significant.

The most valuable insight of this work is that we can control the emission intensity of semiconductor as a function of temperature by introducing a secondary trap site. Typically, semiconductors have the highest PL quantum yield at lowest temperatures, and the quantum yield will decrease with temperature because of increased non-radiative quenching. In all Dy^{3+}-doped Ga_2O_3, we observed an increase in PL quantum yield with temperature, reaching the maximum at around 100 K. A simple kinetic model was made and validated based on Monte Carlo simulation, showing that this phenomenon occurs because the Dy^{3+} dopants form much shallower trapping states that the donor states associated with Ga_2O_3 DAP emission. These insights are also general and can aid in the design of new nanophosphors.

$SrAl_2O_4$ is an insulating oxide with a great deal of commercial appeal because of its ability to be doped with many rare earth elements to impart interesting properties. In this thesis, I designed an upper-level undergraduate chemistry or engineering lab involving the synthesis, processing, and analysis of phosphorescent nanomaterials. In this experiment, students synthesized $Eu,Dy:SrAl_2O_4$ particles by combustion, and then annealed them in a reducing environment containing hydrogen, well above the temperature at which the initial synthesis was performed. Students compared the two samples excited in a dark room (shown in Figure 4.2) and remarked that reduction from Eu^{3+} to Eu^{2+} caused a qualitative change in emission intensity and color. When the excitation source was removed the annealed sample retained its emission indicating an improvement in crystal quality, which students confirmed by XRD analysis.

This experiment has all the characteristics to make a successful undergraduate teaching lab. Students get to see and manipulate physical and chemical principles that are otherwise difficult to visualize; when the annealed samples are removed from the furnace, students can immediately see the difference in emission and, in some cases, their samples even glowed green in a sunlit room. The effect of annealing is made even more clear when the students examine their samples by SEM and XRD. Finally, the incorporation of mechanoluminescence into this lab shows students lesser know physical properties, and demonstrates the importance outside the box thinking. All of this combines to provide a valuable teaching experience for students studying inorganic chemistry, nanoscience, material science, and engineering.

Letters of Copyright Permission

Copyright Clearance Center   RightsLink®

Home	Account Info	Help	LIVE CHAT

ACS Publications
Most Trusted. Most Cited. Most Read.

Title: Surface-Enabled Energy Transfer in Ga2O3–CdSe/CdS Nanocrystal Composite Films: Tunable All-Inorganic Rare Earth Element-Free White-Emitting Phosphor

Author: Paul C. Stanish, Pavle V. Radovanovic

Publication: The Journal of Physical Chemistry C

Publisher: American Chemical Society

Date: Sep 1, 2016

Copyright © 2016, American Chemical Society

Logged in as:
Paul Stanish
University of Waterloo

LOGOUT

PERMISSION/LICENSE IS GRANTED FOR YOUR ORDER AT NO CHARGE

This type of permission/license, instead of the standard Terms & Conditions, is sent to you because no fee is being charged for your order. Please note the following:

- Permission is granted for your request in both print and electronic formats, and translations.
- If figures and/or tables were requested, they may be adapted or used in part.
- Please print this page for your records and send a copy of it to your publisher/graduate school.
- Appropriate credit for the requested material should be given as follows: "Reprinted (adapted) with permission from (COMPLETE REFERENCE CITATION). Copyright (YEAR) American Chemical Society." Insert appropriate information in place of the capitalized words.
- One-time permission is granted only for the use specified in your request. No additional uses are granted (such as derivative works or other editions). For any other uses, please submit a new request.

BACK   CLOSE WINDOW

Copyright Clearance Center

RightsLink®

Home   Account Info   Help   LIVE CHAT

ACS Publications
Most Trusted. Most Cited. Most Read.

Title: Inorganic Phosphors for Teaching a Holistic Approach to Functional Materials Investigation: From Synthesis and Characterization to Applications of Thermo- and Mechanoluminescence

Author: Paul C. Stanish, Howard Siu, Pavle V. Radovanovic

Publication: Journal of Chemical Education

Publisher: American Chemical Society

Date: May 1, 2019

Copyright © 2019, American Chemical Society

Logged in as:
Paul Stanish
University of Waterloo

LOGOUT

PERMISSION/LICENSE IS GRANTED FOR YOUR ORDER AT NO CHARGE

This type of permission/license, instead of the standard Terms & Conditions, is sent to you because no fee is being charged for your order. Please note the following:

- Permission is granted for your request in both print and electronic formats, and translations.
- If figures and/or tables were requested, they may be adapted or used in part.
- Please print this page for your records and send a copy of it to your publisher/graduate school.
- Appropriate credit for the requested material should be given as follows: "Reprinted (adapted) with permission from (COMPLETE REFERENCE CITATION). Copyright (YEAR) American Chemical Society." Insert appropriate information in place of the capitalized words.
- One-time permission is granted only for the use specified in your request. No additional uses are granted (such as derivative works or other editions). For any other uses, please submit a new request.

BACK   CLOSE WINDOW

88

References

(1)   Liu, L.; Keoleian, G. A.; Saitou, K. Replacement Policy of Residential Lighting Optimized for Cost, Energy, and Greenhouse Gas Emissions. *Environ. Res. Lett.* **2017**, *12*, 114034.

(2)   Gago, E. J.; Muneer, T.; Knez, M.; Köster, H. Natural Light Controls and Guides in Buildings. Energy Saving for Electrical Lighting, Reduction of Cooling Load. *Renew. Sustain. Energy Rev.* **2015**, *41*, 1–13.

(3)   Pust, P.; Schmidt, P. J.; Schnick, W. A Revolution in Lighting. *Nat. Mater.* **2015**, *14*, 454–458.

(4)   Schubert, E. F. Solid-State Light Sources Getting Smart. *Science* **2005**, *308*, 1274–1278.

(5)   Lux. LED breakthrough promises ultra efficient luminaires http://luxreview.com/article/2018/01/led-breakthrough-promises-ultra-efficient-luminaires (accessed Jun 7, 2018).

(6)   Today, S. Samsung achieves 220lm/W luminous efficacy with new mid-power LED package http://www.semiconductor-today.com/news_items/2017/jun/samsung_160617.shtml (accessed Jun 7, 2018).

(7)   Smith, T.; Guild, J. The C.I.E. Colorimetric Standards and Their Use. *Trans. Opt. Soc.* **1931**, *33*, 73–134.

(8)   Choudhury, K. R. *Principles of Colour and Appearance Measurement: Object Appearance, Colour Perception and Instrumental Measurement*; Woodhead Publishing, 2014.

(9)   Sivaji, A.; Shopian, S.; Nor, Z. M.; Chuan, N.-K.; Bahri, S. Lighting Does Matter: Preliminary Assessment on Office Workers. *Procedia - Soc. Behav. Sci.* **2013**, *97*, 638–647.

(10)   Mills, P. R.; Tomkins, S. C.; Schlangen, L. J. The Effect of High Correlated Colour Temperature Office Lighting on Employee Wellbeing and Work Performance. *J. Circadian Rhythms* **2007**, *5*, 2.

(11)   Hunt, R. W. G.; Pointer, M. R. *Measuring Colour*; John Wiley & Sons, Ltd: Chichester, UK, 2011.

(12)   Hsiao, S.-W.; Hsiao, Y.-T.; Chen, S.-K.; Hsu, C.-F.; Lee, C.-H.; Chiang, Y.-H. An Ergonomic Study of Visual Optimization by Light Color Managements. *Color Res. Appl.* **2016**, *41*, 72–84.

(13)   Anderson, J. L.; Glod, C. A.; Dai, J.; Cao, Y.; Lockley, S. W. Lux vs. Wavelength in Light Treatment of Seasonal Affective Disorder. *Acta Psychiatr. Scand.* **2009**, *120*, 203–212.

(14)   Partonen, T. Effects of Morning Light Treatment on Subjective Sleepiness and Mood in Winter Depression. *J. Affect. Disord.* **1994**, *30*, 47–56.

(15)   Eastman, C. I.; Young, M. A.; Fogg, L. F.; Liu, L.; Meaden, P. M. Bright Light Treatment of Winter Depression. *Arch. Gen. Psychiatry* **1998**, *55*, 883–889.

(16)   Hye Oh, J.; Ji Yang, S.; Rag Do, Y. Healthy, Natural, Efficient and Tunable Lighting: Four-Package White LEDs for Optimizing the Circadian Effect, Color Quality and Vision Performance. *Light Sci. Appl.* **2014**, *3*, e141–e141.

(17)   601, T. File:Metamerie.jpg https://commons.wikimedia.org/wiki/File:Metamerie.jpg.

(18)   Drabold, D. A.; Estreicher, S. K. Defect Theory: An Armchair History. In *Theory of Defects in Semiconductors*; Springer Berlin Heidelberg; pp 11–28.

(19)   Queisser, H. J. Defects in Semiconductors: Some Fatal, Some Vital. *Science* **1998**, *281*, 945–950.

(20)   Lorenz, M. R.; Woods, J. F.; Gambino, R. J. Some Electrical Properties of the Semiconductor β-Ga_2O_3. *J. Phys. Chem. Solids* **1967**, *28*, 403–404.

(21)   Binet, L.; Gourier, D. Origin of the Blue Luminescence of β-Ga_2O_3. *J. Phys. Chem. Solids* **1998**, *59*, 1241–1249.

(22)   Ueda, N.; Hosono, H.; Waseda, R.; Kawazoe, H. Synthesis and Control of Conductivity of Ultraviolet Transmitting β-Ga_2O_3 Single Crystals. *Appl. Phys. Lett.* **1997**, *70*, 3561–3563.

(23)   Kılıç, Ç.; Zunger, A. Origins of Coexistence of Conductivity and Transparency in SnO_2.

Phys. Rev. Lett. **2002**, *88*, 095501.

(24) Wang, T.; Farvid, S. S.; Abulikemu, M.; Radovanovic, P. V. Size-Tunable Phosphorescence in Colloidal Metastable γ-Ga$_2$O$_3$ Nanocrystals. *J. Am. Chem. Soc.* **2010**, *132*, 9250–9252.

(25) Xiao, W.-Z.; Wang, L.-L.; Xu, L.; Wan, Q.; Pan, A.-L. Electronic Structure and Magnetic Properties in Nitrogen-Doped from Density Functional Calculations. *Solid State Commun.* **2010**, *150*, 852–856.

(26) Stanish, P. C.; Radovanovic, P. V. Surface-Enabled Energy Transfer in Ga$_2$O$_3$–CdSe/CdS Nanocrystal Composite Films: Tunable All-Inorganic Rare Earth Element-Free White-Emitting Phosphor. *J. Phys. Chem. C* **2016**, *120*, 19566–19573.

(27) Wang, T.; Chirmanov, V.; Chiu, W. H. M.; Radovanovic, P. V. Generating Tunable White Light by Resonance Energy Transfer in Transparent Dye-Conjugated Metal Oxide Nanocrystals. *J. Am. Chem. Soc.* **2013**, *135*, 14520–14523.

(28) Maximenko, S. I.; Mazeina, L.; Picard, Y. N.; Freitas, J. A.; Bermudez, V. M.; Prokes, S. M. Cathodoluminescence Studies of the Inhomogeneities in Sn-Doped Ga$_2$O$_3$ Nanowires. *Nano Lett.* **2009**, *9*, 3245–3251.

(29) Zhao, X.; Wu, Z.; Cui, W.; Zhi, Y.; Guo, D.; Li, L.; Tang, W. Impurity Compensation Effect Induced by Tin Valence Change in α-Ga$_{1.4}$Sn$_{0.6}$O$_3$ Thin Films. *ACS Appl. Mater. Interfaces* **2017**, *9*, 983–988.

(30) Ghodsi, V.; Jin, S.; Byers, J. C.; Pan, Y.; Radovanovic, P. V. Anomalous Photocatalytic Activity of Nanocrystalline γ-Phase Ga$_2$O$_3$ Enabled by Long-Lived Defect Trap States. *J. Phys. Chem. C* **2017**, *121*, 9433–9441.

(31) Zheng, B.; Hua, W.; Yue, Y.; Gao, Z. Dehydrogenation of Propane to Propene over Different Polymorphs of Gallium Oxide. *J. Catal.* **2005**, *232*, 143–151.

(32) Yoshioka, S.; Hayashi, H.; Kuwabara, A.; Oba, F.; Matsunaga, K.; Tanaka, I. Structures and Energetics of Ga$_2$O$_3$ Polymorphs. *J. Phys. Condens. Matter* **2007**, *19*, 346211.

(33) Nishi, K.; Shimizu, K.; Takamatsu, M.; Yoshida, H.; Satsuma, A.; Tanaka, T.; Yoshida,

S.; Hattori, T. Deconvolution Analysis of Ga K-Edge XANES for Quantification of Gallium Coordinations in Oxide Environments. *J. Phys. Chem. B* **1998**, *102*, 10190–10195.

(34) Collins, S. E.; Baltanás, M. A.; Bonivardi, A. L. Hydrogen Chemisorption on Gallium Oxide Polymorphs. *Langmuir* **2005**, *21*, 962–970.

(35) Playford, H. Y.; Hannon, A. C.; Tucker, M. G.; Dawson, D. M.; Ashbrook, S. E.; Kastiban, R. J.; Sloan, J.; Walton, R. I. Characterization of Structural Disorder in γ-Ga$_2$O$_3$. *J. Phys. Chem. C* **2014**, *118*, 16188–16198.

(36) Ghodsi, V. Modulating Optical and Photocatalytic Properties of Transparent Metal Oxide Nanostructures via Defect Engineering, University of Waterloo, 2018.

(37) Blasse, G.; Bril, A. Some Observations on the Luminescence of β-Ga$_2$O$_3$. *J. Phys. Chem. Solids* **1970**, *31*, 707–711.

(38) Harwig, T.; Kellendonk, F. Some Observations on the Photoluminescence of Doped β-Galliumsesquioxide. *J. Solid State Chem.* **1978**, *24*, 255–263.

(39) Chen, T.; Tang, K. γ-Ga$_2$O$_3$ Quantum Dots with Visible Blue-Green Light Emission Property. *Appl. Phys. Lett.* **2007**, *90*, 053104.

(40) Thomas, D. G.; Hopfield, J. J.; Augustyniak, W. M. Kinetics of Radiative Recombination at Randomly Distributed Donors and Acceptors. *Phys. Rev.* **1965**, *140*, A202–A220.

(41) Hegde, M.; Wang, T.; Mišković, Z. L.; Radovanovic, P. V. Origin of Size-Dependent Photoluminescence Decay Dynamics in Colloidal γ-Ga$_2$O$_3$ Nanocrystals. *Appl. Phys. Lett.* **2012**, *100*, 141903.

(42) Fernandes, B.; Hegde, M.; Stanish, P. C.; Mišković, Z. L.; Radovanovic, P. V. Photoluminescence Decay Dynamics in γ-Ga$_2$O$_3$ Nanocrystals: The Role of Exclusion Distance at Short Time Scales. *Chem. Phys. Lett.* **2017**, *684*, 135–140.

(43) Simmons, R. O.; Balluffi, R. W. Measurements of Equilibrium Vacancy Concentrations in Aluminum. *Phys. Rev.* **1960**, *117*, 52–61.

(44) Freysoldt, C.; Grabowski, B.; Hickel, T.; Neugebauer, J.; Kresse, G.; Janotti, A.; Van de

Walle, C. G. First-Principles Calculations for Point Defects in Solids. *Rev. Mod. Phys.* **2014**, *86*, 253–305.

(45)   Harvey, E. N. *A History of Luminescence from the Earliest Times until 1900*; American Philosophical Society, 1957; Vol. 44.

(46)   Van den Eeckhout, K.; Smet, P. F.; Poelman, D. Persistent Luminescence in Eu^{2+}-Doped Compounds: A Review. *Materials* **2010**, *3*, 2536–2566.

(47)   Abbruscato, V. Optical and Electrical Properties of $SrAl_2O_4$:Eu^{2+}. *J. Electrochem. Soc.* **1971**, *118*, 930–933.

(48)   Matsuzawa, T.; Aoki, Y.; Takeuchi, N.; Murayama, Y. A New Long Phosphorescent Phosphor with High Brightness, $SrAl_2O_4$:Eu^{2+},Dy^{3+}. *J. Electrochem. Soc.* **1996**, *143*, 2670–2673.

(49)   Lan, Z.; Chengyu, L.; Qiang, S. Long Lasting Phosphorescence in Eu^{2+} and Ce^{3+} Co-Doped Strontium Borate Glasses. *J. Rare Earths* **2006**, *24*, 196–198.

(50)   Aitasalo, T.; Dereń, P.; Hölsä, J.; Jungner, H.; Krupa, J.-C.; Lastusaari, M.; Legendziewicz, J.; Niittykoski, J.; Stręk, W. Persistent Luminescence Phenomena in Materials Doped with Rare Earth Ions. *J. Solid State Chem.* **2003**, *171*, 114–122.

(51)   Dorenbos, P. Locating Lanthanide Impurity Levels in the Forbidden Band of Host Crystals. *J. Lumin.* **2004**, *108*, 301–305.

(52)   Clabau, F.; Rocquefelte, X.; Jobic, S.; Deniard, P.; Whangbo, M.-H.; Garcia, A.; Le Mercier, T. Mechanism of Phosphorescence Appropriate for the Long-Lasting Phosphors Eu^{2+} -Doped $SrAl_2O_4$ with Codopants Dy^{3+} and B^{3+}. *Chem. Mater.* **2005**, *17*, 3904–3912.

(53)   Dorenbos, P. Mechanism of Persistent Luminescence in Eu^{2+} and Dy^{3+} Codoped Aluminate and Silicate Compounds. *J. Electrochem. Soc.* **2005**, *152*, H107–H110.

(54)   Bube, R. H. Luminescence and Trapping in Zinc Sulfide Phosphors with and without Copper Activator. *Phys. Rev.* **1950**, *80*, 655–666.

(55)   McKeever, S. W. S. *Thermoluminescence of Solids*; Cambridge University Press, 1985.

(56)   Sahu, I. P.; Bisen, D. P.; Brahme, N. Dysprosium Doped Di-Strontium Magnesium Di-

Silicate White Light Emitting Phosphor by Solid State Reaction Method. *Displays* **2014**, *35*, 279–286.

(57) Shi, C.; Fu, Y.; Liu, B.; Zhang, G.; Chen, Y.; Qi, Z.; Luo, X. The Roles of Eu^{2+} and Dy^{3+} in the Blue Long-Lasting Phosphor $Sr_2MgSi_2O_7$: Eu^{2+}, Dy^{3+}. *J. Lumin.* **2007**, *122–123*, 11–13.

(58) Dean, P. J. Inter-Impurity Recombinations in Semiconductors. *Prog. Solid State Chem.* **1973**, *8*, 1–126.

(59) Varshni, Y. P. Temperature Dependence of the Energy Gap in Semiconductors. *Physica* **1967**, *34*, 149–154.

(60) Li, Z.-F.; Zhou, L.; Yu, J.-B.; Zhang, H.-J.; Deng, R.-P.; Peng, Z.-P.; Guo, Z.-Y. Synthesis, Structure, Photoluminescence, and Electroluminescence Properties of a New Dysprosium Complex. *J. Phys. Chem. C* **2007**, *111*, 2295–2300.

(61) Aggarwal, N.; Vasishth, A.; Kaur, K.; Verma, N. K. Role of Dysprosium Doping on Structural, Optical, Magnetic and Electrical Properties of ZnO Nanorods. *J. Supercond. Nov. Magn.* **2018**, *32*, 685–691.

(62) Katsumata, T.; Sasajima, K.; Nabae, T.; Komuro, S.; Morikawa, T. Characteristics of Strontium Aluminate Crystals Used for Long-Duration Phosphors. *J. Am. Ceram. Soc.* **2005**, *81*, 413–416.

(63) Seltzer, M. D.; Wright, A. O.; Morrison, C. A.; Wortman, D. E.; Gruber, J. B.; Filer, E. D. Optical Spectra, Energy Levels and Branching Ratios of Trivalent Dysprosium-Doped Yttrium Scandium Gallium Garnet. *J. Phys. Chem. Solids* **1996**, *57*, 1175–1182.

(64) Ruan, C.; Zhang, Y.; Lu, M.; Ji, C.; Sun, C.; Chen, X.; Chen, H.; Colvin, V.; Yu, W. White Light-Emitting Diodes Based on $AgInS_2$/ZnS Quantum Dots with Improved Bandwidth in Visible Light Communication. *Nanomaterials* **2016**, *6*, 13.

(65) Lim, S. Y.; Shen, W.; Gao, Z. Carbon Quantum Dots and Their Applications. *Chem. Soc. Rev.* **2015**, *44*, 362–381.

(66) Dai, X.; Zhang, Z.; Jin, Y.; Niu, Y.; Cao, H.; Liang, X.; Chen, L.; Wang, J.; Peng, X.

Solution-Processed, High-Performance Light-Emitting Diodes Based on Quantum Dots. *Nature* **2014**, *515*, 96–99.

(67)   Yang, Y.; Zheng, Y.; Cao, W.; Titov, A.; Hyvonen, J.; Manders, J. R.; Xue, J.; Holloway, P. H.; Qian, L. High-Efficiency Light-Emitting Devices Based on Quantum Dots with Tailored Nanostructures. *Nat. Photonics* **2015**, *9*, 259–266.

(68)   Shirasaki, Y.; Supran, G. J.; Bawendi, M. G.; Bulović, V. Emergence of Colloidal Quantum-Dot Light-Emitting Technologies. *Nat. Photonics* **2013**, *7*, 13–23.

(69)   Rühle, S.; Shalom, M.; Zaban, A. Quantum-Dot-Sensitized Solar Cells. *ChemPhysChem* **2010**, *11*, 2290–2304.

(70)   Nozik, A. . Quantum Dot Solar Cells. *Phys. E Low-dimensional Syst. Nanostructures* **2002**, *14*, 115–120.

(71)   Shi, L.; De Paoli, V.; Rosenzweig, N.; Rosenzweig, Z. Synthesis and Application of Quantum Dots FRET-Based Protease Sensors. *J. Am. Chem. Soc.* **2006**, *128*, 10378–10379.

(72)   Dabbousi, B. O.; Rodriguez-Viejo, J.; Mikulec, F. V.; Heine, J. R.; Mattoussi, H.; Ober, R.; Jensen, K. F.; Bawendi, M. G. (CdSe)ZnS Core−Shell Quantum Dots: Synthesis and Characterization of a Size Series of Highly Luminescent Nanocrystallites. *J. Phys. Chem. B* **1997**, *101*, 9463–9475.

(73)   Alivisatos, A. P. Semiconductor Clusters, Nanocrystals, and Quantum Dots. *Science* **1996**, *271*, 933–937.

(74)   Efros, A. L.; Efros, A. L. Interband Absorption of Light in a Semiconductor Sphere. *Sov. Phys. - Semicond.* **1982**, *16*, 772–775.

(75)   Brus, L. E. A Simple Model for the Ionization Potential, Electron Affinity, and Aqueous Redox Potentials of Small Semiconductor Crystallites. *J. Chem. Phys.* **1983**, *79*, 5566–5571.

(76)   Brus, L. Electronic Wave Functions in Semiconductor Clusters: Experiment and Theory. *J. Phys. Chem.* **1986**, *90*, 2555–2560.

(77)   Wang, Y.; Herron, N. Nanometer-Sized Semiconductor Clusters: Materials Synthesis, Quantum Size Effects, and Photophysical Properties. *J. Phys. Chem.* **1991**, *95*, 525–532.

(78)   Murray, C. B.; Norris, D. J.; Bawendi, M. G. Synthesis and Characterization of Nearly Monodisperse CdE (E = Sulfur, Selenium, Tellurium) Semiconductor Nanocrystallites. *J. Am. Chem. Soc.* **1993**, *115*, 8706–8715.

(79)   Yu, W. W.; Qu, L.; Guo, W.; Peng, X. Experimental Determination of the Extinction Coefficient of CdTe, CdSe, and CdS Nanocrystals. *Chem. Mater.* **2003**, *15*, 2854–2860.

(80)   Alivisatos, A. P. Perspectives on the Physical Chemistry of Semiconductor Nanocrystals. *J. Phys. Chem.* **1996**, *100*, 13226–13239.

(81)   Bera, D.; Qian, L.; Tseng, T.-K.; Holloway, P. H. Quantum Dots and Their Multimodal Applications: A Review. *Materials* **2010**, *3*, 2260–2345.

(82)   Hawrylak, P.; Narvaez, G. A.; Bayer, M.; Forchel, A. Excitonic Absorption in a Quantum Dot. *Phys. Rev. Lett.* **2000**, *85*, 389–392.

(83)   Norris, D. J.; Bawendi, M. G. Structure in the Lowest Absorption Feature of CdSe Quantum Dots. *J. Chem. Phys.* **1995**, *103*, 5260–5268.

(84)   Bang, J.; Yang, H.; Holloway, P. H. Enhanced and Stable Green Emission of ZnO Nanoparticles by Surface Segregation of Mg. *Nanotechnology* **2006**, *17*, 973–978.

(85)   Kuçur, E.; Bücking, W.; Giernoth, R.; Nann, T. Determination of Defect States in Semiconductor Nanocrystals by Cyclic Voltammetry. *J. Phys. Chem. B* **2005**, *109*, 20355–20360.

(86)   Colvin, V. L.; Goldstein, A. N.; Alivisatos, A. P. Semiconductor Nanocrystals Covalently Bound to Metal Surfaces with Self-Assembled Monolayers. *J. Am. Chem. Soc.* **1992**, *114*, 5221–5230.

(87)   Chen, X.; Lou, Y.; Samia, A. C.; Burda, C. Coherency Strain Effects on the Optical Response of Core/Shell Heteronanostructures. *Nano Lett.* **2003**, *3*, 799–803.

(88)   Grabolle, M.; Ziegler, J.; Merkulov, A.; Nann, T.; Resch-Genger, U. Stability and Fluorescence Quantum Yield of CdSe-ZnS Quantum Dots-Influence of the Thickness of

the ZnS Shell. *Ann. N. Y. Acad. Sci.* **2008**, *1130*, 235–241.

(89)   Chen, O.; Zhao, J.; Chauhan, V. P.; Cui, J.; Wong, C.; Harris, D. K.; Wei, H.; Han, H.-S.; Fukumura, D.; Jain, R. K.; et al. Compact High-Quality CdSe–CdS Core–Shell Nanocrystals with Narrow Emission Linewidths and Suppressed Blinking. *Nat. Mater.* **2013**, *12*, 445–451.

(90)   Xie, R.; Kolb, U.; Li, J.; Basché, T.; Mews, A. Synthesis and Characterization of Highly Luminescent CdSe−Core CdS/$Zn_{0.5}Cd_{0.5}$ S/ZnS Multishell Nanocrystals. *J. Am. Chem. Soc.* **2005**, *127*, 7480–7488.

(91)   Kundu, J.; Ghosh, Y.; Dennis, A. M.; Htoon, H.; Hollingsworth, J. A. Giant Nanocrystal Quantum Dots: Stable Down-Conversion Phosphors That Exploit a Large Stokes Shift and Efficient Shell-to-Core Energy Relaxation. *Nano Lett.* **2012**, *12*, 3031–3037.

(92)   Chen, Y.; Vela, J.; Htoon, H.; Casson, J. L.; Werder, D. J.; Bussian, D. A.; Klimov, V. I.; Hollingsworth, J. A. "Giant" Multishell CdSe Nanocrystal Quantum Dots with Suppressed Blinking. *J. Am. Chem. Soc.* **2008**, *130*, 5026–5027.

(93)   Meinardi, F.; Colombo, A.; Velizhanin, K. A.; Simonutti, R.; Lorenzon, M.; Beverina, L.; Viswanatha, R.; Klimov, V. I.; Brovelli, S. Large-Area Luminescent Solar Concentrators Based on 'Stokes-Shift-Engineered' Nanocrystals in a Mass-Polymerized PMMA Matrix. *Nat. Photonics* **2014**, *8*, 392–399.

(94)   Förster, T. Zwischenmolekulare Energiewanderung Und Fluoreszenz. *Ann. Phys.* **1948**, *437*, 55–75.

(95)   Főrster, T. 10th Spiers Memorial Lecture. Transfer Mechanisms of Electronic Excitation. *Discuss. Faraday Soc.* **1959**, *27*, 7–17.

(96)   Lakowicz, J. R. *Principles of Fluorescence Spectroscopy*, 3rd ed.; Springer: Boston, 2006.

(97)   Tsien, R. Y. The Green Fluorescent Protein. *Annu. Rev. Biochem.* **1998**, *67*, 509–544.

(98)   Miyawaki, A.; Llopis, J.; Heim, R.; McCaffery, J. M.; Adams, J. A.; Ikura, M.; Tsien, R. Y. Fluorescent Indicators for Ca^{2+} Based on Green Fluorescent Proteins and Calmodulin. *Nature* **1997**, *388*, 882–887.

(99)   Chan, F. K.-M.; Siegel, R. M.; Zacharias, D.; Swofford, R.; Holmes, K. L.; Tsien, R. Y.; Lenardo, M. J. Fluorescence Resonance Energy Transfer Analysis of Cell Surface Receptor Interactions and Signaling Using Spectral Variants of the Green Fluorescent Protein. *Cytometry* **2001**, *44*, 361–368.

(100) Jones, J.; Heim, R.; Hare, E.; Stack, J.; Pollok, B. A. Development and Application of a GFP-FRET Intracellular Caspase Assay for Drug Screening. *J. Biomol. Screen.* **2000**, *5*, 307–317.

(101) Khrenova, M.; Topol, I.; Collins, J.; Nemukhin, A. Estimating Orientation Factors in the FRET Theory of Fluorescent Proteins: The TagRFP-KFP Pair and Beyond. *Biophys. J.* **2015**, *108*, 126–132.

(102) Xu, Q.-H.; Wang, S.; Korystov, D.; Mikhailovsky, A.; Bazan, G. C.; Moses, D.; Heeger, A. J. The Fluorescence Resonance Energy Transfer (FRET) Gate: A Time-Resolved Study. *Proc. Natl. Acad. Sci.* **2005**, *102*, 530–535.

(103) Clapp, A. R.; Medintz, I. L.; Mauro, J. M.; Fisher, B. R.; Bawendi, M. G.; Mattoussi, H. Fluorescence Resonance Energy Transfer Between Quantum Dot Donors and Dye-Labeled Protein Acceptors. *J. Am. Chem. Soc.* **2004**, *126*, 301–310.

(104) Kang, J. S.; Piszczek, G.; Lakowicz, J. R. Enhanced Emission Induced by FRET from a Long- Lifetime , Low Quantum Yield Donor to a Long- Wavelength , High Quantum Yield Acceptor. *J. Fluoresc.* **2002**, *12*, 97–103.

(105) Layek, A.; Stanish, P. C.; Chirmanov, V.; Radovanovic, P. V. Hybrid ZnO-Based Nanoconjugate for Efficient and Sustainable White Light Generation. *Chem. Mater.* **2015**, *27*, 1021–1030.

(106) Chirmanov, V.; Stanish, P. C.; Layek, A.; Radovanovic, P. V. Distance-Dependent Energy Transfer between Ga_2O_3 Nanocrystal Defect States and Conjugated Organic Fluorophores in Hybrid White-Light-Emitting Nanophosphors. *J. Phys. Chem. C* **2015**, *119*, 5687–5696.

(107) Dworak, L.; Matylitsky, V. V.; Ren, T.; Basché, T.; Wachtveitl, J. Acceptor Concentration Dependence of Förster Resonance Energy Transfer Dynamics in Dye–Quantum Dot Complexes. *J. Phys. Chem. C* **2014**, *118*, 4396–4402.

(108) Funston, A. M.; Jasieniak, J. J.; Mulvaney, P. Complete Quenching of CdSe Nanocrystal Photoluminescence by Single Dye Molecules. *Adv. Mater.* **2008**, *20*, 4274–4280.

(109) Chen, O.; Wei, H.; Maurice, A.; Bawendi, M.; Reiss, P. Pure Colors from Core–Shell Quantum Dots. *MRS Bull.* **2013**, *38*, 696–702.

(110) Peng, X.; Wickham, J.; Alivisatos, A. P. Kinetics of II-VI and III-V Colloidal Semiconductor Nanocrystal Growth: "Focusing" of Size Distributions. *J. Am. Chem. Soc.* **1998**, *120*, 5343–5344.

(111) Medintz, I. L.; Uyeda, H. T.; Goldman, E. R.; Mattoussi, H. Quantum Dot Bioconjugates for Imaging, Labelling and Sensing. *Nat. Mater.* **2005**, *4*, 435–446.

(112) Yao, W.-T.; Yu, S.-H. Synthesis of Semiconducting Functional Materials in Solution: From II-VI Semiconductor to Inorganic-Organic Hybrid Semiconductor Nanomaterials. *Adv. Funct. Mater.* **2008**, *18*, 3357–3366.

(113) Agranovich, V. M.; Gartstein, Y. N.; Litinskaya, M. Hybrid Resonant Organic–Inorganic Nanostructures for Optoelectronic Applications. *Chem. Rev.* **2011**, *111*, 5179–5214.

(114) Brown, L. R. *World On the Edge: How To Prevent Environmental And Economic Collapse*, 1st ed.; W.W. Norton & Company: New York, 2010.

(115) Khan, N.; Abas, N. Comparative Study of Energy Saving Light Sources. *Renew. Sustain. Energy Rev.* **2011**, *15*, 296–309.

(116) Pimputkar, S.; Speck, J. S.; DenBaars, S. P.; Nakamura, S. Prospects for LED Lighting. *Nat. Photonics* **2009**, *3*, 180–182.

(117) Ye, S.; Xiao, F.; Pan, Y. X.; Ma, Y. Y.; Zhang, Q. Y. Phosphors in Phosphor-Converted White Light-Emitting Diodes: Recent Advances in Materials, Techniques and Properties. *Mater. Sci. Eng. R Reports* **2010**, *71*, 1–34.

(118) Krames, M. R.; Shchekin, O. B.; Mueller-Mach, R.; Mueller, G. O.; Zhou, L.; Harbers, G.; Craford, M. G. Status and Future of High-Power Light-Emitting Diodes for Solid-State Lighting. *J. Disp. Technol.* **2007**, *3*, 160–175.

(119) Xie, R.-J.; Hirosaki, N.; Suehiro, T.; Xu, F.-F.; Mitomo, M. A Simple, Efficient Synthetic

Route to $Sr_2Si_5N_8$:Eu^{2+} -Based Red Phosphors for White Light-Emitting Diodes. *Chem. Mater.* **2006**, *18*, 5578–5583.

(120) Korthout, K.; Smet, P. F.; Poelman, D. Rare Earth Doped Core-Shell Particles as Phosphor for Warm-White Light-Emitting Diodes. *Appl. Phys. Lett.* **2011**, *98*, 261919.

(121) Chang, Y.; Sun, D.; Zhang, Z.; Zhang, Y.; Yao, X.; Jiang, D.; Yu, Y.; Mi, L.; Chen, L.; Zhong, H.; et al. High Color-Rendering-Index Hybrid White LEDs Employing CdSe/ZnS Core/Shell Quantum Dots. *J. Nanosci. Nanotechnol.* **2016**, *16*, 670–676.

(122) Wang, T.; Radovanovic, P. V. Size-Dependent Electron Transfer and Trapping in Strongly Luminescent Colloidal Gallium Oxide Nanocrystals. *J. Phys. Chem. C* **2011**, *115*, 18473–18478.

(123) Wang, T.; Radovanovic, P. V. In Situ Enhancement of the Blue Photoluminescence of Colloidal Ga_2O_3 Nanocrystals by Promotion of Defect Formation in Reducing Conditions. *Chem. Commun.* **2011**, *47*, 7161–7163.

(124) Farvid, S. S.; Wang, T.; Radovanovic, P. V. Colloidal Gallium Indium Oxide Nanocrystals: A Multifunctional Light-Emitting Phosphor Broadly Tunable by Alloy Composition. *J. Am. Chem. Soc.* **2011**, *133*, 6711–6719.

(125) Peng, Z. A.; Peng, X. Formation of High-Quality CdTe, CdSe, and CdS Nanocrystals Using CdO as Precursor. *J. Am. Chem. Soc.* **2001**, *123*, 183–184.

(126) Dibbell, R. S.; Watson, D. F. Distance-Dependent Electron Transfer in Tethered Assemblies of CdS Quantum Dots and TiO_2 Nanoparticles. *J. Phys. Chem. C* **2009**, *113*, 3139–3149.

(127) Zhu, H.; Hu, M. Z.; Shao, L.; Yu, K.; Dabestani, R.; Zaman, M. B.; Liao, S. Synthesis and Optical Properties of Thiol Functionalized CdSe/ZnS (Core/Shell) Quantum Dots by Ligand Exchange. *J. Nanomater.* **2014**, *2014*, 1–14.

(128) Jeong, S.; Achermann, M.; Nanda, J.; Ivanov, S.; Klimov, V. I.; Hollingsworth, J. A. Effect of the Thiol−Thiolate Equilibrium on the Photophysical Properties of Aqueous CdSe/ZnS Nanocrystal Quantum Dots. *J. Am. Chem. Soc.* **2005**, *127*, 10126–10127.

(129) Reiss, P.; Protière, M.; Li, L. Core/Shell Semiconductor Nanocrystals. *Small* **2009**, *5*, 154–168.

(130) Cantor, C. R.; Pechukas, P. Determination of Distance Distribution Functions by Singlet-Singlet Energy Transfer. *Proc. Natl. Acad. Sci.* **1971**, *68*, 2099–2101.

(131) Clapp, A. R.; Medintz, I. L.; Mattoussi, H. Förster Resonance Energy Transfer Investigations Using Quantum-Dot Fluorophores. *ChemPhysChem* **2006**, *7*, 47–57.

(132) Chen, L.; Lin, C.-C.; Yeh, C.-W.; Liu, R.-S. Light Converting Inorganic Phosphors for White Light-Emitting Diodes. *Materials* **2010**, *3*, 2172–2195.

(133) Inc., N. C. *Energy Savings Potential of Solid-State Lighting in General Illumination Applications*; 2012.

(134) Steigerwald, D. A.; Bhat, J. C.; Collins, D.; Fletcher, R. M.; Holcomb, M. O.; Ludowise, M. J.; Martin, P. S.; Rudaz, S. L. Illumination with Solid State Lighting Technology. *IEEE J. Sel. Top. Quantum Electron.* **2002**, *8*, 310–320.

(135) George, N. C.; Denault, K. A.; Seshadri, R. Phosphors for Solid-State White Lighting. *Annu. Rev. Mater. Res.* **2013**, *43*, 481–501.

(136) Setlur, A. A.; Heward, W. J.; Gao, Y.; Srivastava, A. M.; Chandran, R. G.; Shankar, M. V. Crystal Chemistry and Luminescence of Ce^{3+}-Doped $Lu_2CaMg_2(Si,Ge)_3O_{12}$ and Its Use in LED Based Lighting. *Chem. Mater.* **2006**, *18*, 3314–3322.

(137) Alonso, E.; Sherman, A. M.; Wallington, T. J.; Everson, M. P.; Field, F. R.; Roth, R.; Kirchain, R. E. Evaluating Rare Earth Element Availability: A Case with Revolutionary Demand from Clean Technologies. *Environ. Sci. Technol.* **2012**, *46*, 3406–3414.

(138) Li, Y. Q.; Rizzo, A.; Cingolani, R.; Gigli, G. Bright White-Light-Emitting Device from Ternary Nanocrystal Composites. *Adv. Mater.* **2006**, *18*, 2545–2548.

(139) Lita, A.; Washington, A. L.; van de Burgt, L.; Strouse, G. F.; Stiegman, A. E. Stable Efficient Solid-State White-Light-Emitting Phosphor with a High Scotopic/Photopic Ratio Fabricated from Fused CdSe-Silica Nanocomposites. *Adv. Mater.* **2010**, *22*, 3987–3991.

(140) Villa, I.; Vedda, A.; Fasoli, M.; Lorenzi, R.; Kränzlin, N.; Rechberger, F.; Ilari, G.; Primc,

D.; Hattendorf, B.; Heiligtag, F. J.; et al. Size-Dependent Luminescence in HfO_2 Nanocrystals: Toward White Emission from Intrinsic Surface Defects. *Chem. Mater.* **2016**, *28*, 3245–3253.

(141) Bowers, M. J.; McBride, J. R.; Rosenthal, S. J. White-Light Emission from Magic-Sized Cadmium Selenide Nanocrystals. *J. Am. Chem. Soc.* **2005**, *127*, 15378–15379.

(142) Wu, S.; Pan, Z.; Chen, R.; Liu, X. Applications of Inorganic Afterglow Phosphors. In *Long Afterglow Phosphorescent Materials*; Springer, Cham, 2017; pp 101–116.

(143) Nag, A.; Sarma, D. D. White Light from Mn^{2+}-Doped CdS Nanocrystals: A New Approach. *J. Phys. Chem. C* **2007**, *111*, 13641–13644.

(144) Panda, S. K.; Hickey, S. G.; Demir, H. V.; Eychmüller, A. Bright White-Light Emitting Manganese and Copper Co-Doped ZnSe Quantum Dots. *Angew. Chemie Int. Ed.* **2011**, *50*, 4432–4436.

(145) Stanish, P.; Radovanovic, P. Energy Transfer between Conjugated Colloidal Ga_2O_3 and CdSe/CdS Core/Shell Nanocrystals for White Light Emitting Applications. *Nanomaterials* **2016**, *6*, 32.

(146) Smith, A. M.; Nie, S. Semiconductor Nanocrystals: Structure, Properties, and Band Gap Engineering. *Acc. Chem. Res.* **2010**, *43*, 190–200.

(147) Zhong, H.; Bai, Z.; Zou, B. Tuning the Luminescence Properties of Colloidal I–III–VI Semiconductor Nanocrystals for Optoelectronics and Biotechnology Applications. *J. Phys. Chem. Lett.* **2012**, *3*, 3167–3175.

(148) Chou, K.; Dennis, A. Förster Resonance Energy Transfer between Quantum Dot Donors and Quantum Dot Acceptors. *Sensors* **2015**, *15*, 13288–13325.

(149) Achermann, M.; Petruska, M. A.; Kos, S.; Smith, D. L.; Koleske, D. D.; Klimov, V. I. Energy-Transfer Pumping of Semiconductor Nanocrystals Using an Epitaxial Quantum Well. *Nature* **2004**, *429*, 642–646.

(150) Kagan, C. R.; Murray, C. B.; Nirmal, M.; Bawendi, M. G. Electronic Energy Transfer in CdSe Quantum Dot Solids. *Phys. Rev. Lett.* **1996**, *76*, 1517–1520.

(151) Li, Y.; Gecevicius, M.; Qiu, J. Long Persistent Phosphors—from Fundamentals to Applications. *Chem. Soc. Rev.* **2016**, *45*, 2090–2136.

(152) Yen, W. M.; Yamamoto, H.; Shionoya, S. *Phosphor Handbook*; CRC Press: Boca Raton, 2006.

(153) Eikmeier, M.; Lohmann, P.; Koops, A. Long-Afterglow Adhesive Tape. US patent 5858495, 1999.

(154) Schäfer, K.; Wang, H.; Pich, A.; MoÏler, M.; Damm, C.; Peukert, W.; Wilms, C.; Seide, G.; Gries, T. Novel Luminescent Composite Polymer Fibers for Warning and Security Systems. *Chem. Fibers Int.* **2012**, *62*, 130–132.

(155) Zhang, J.-C.; Xu, C.-N.; Kamimura, S.; Terasawa, Y.; Yamada, H.; Wang, X. An Intense Elastico-Mechanoluminescence Material $CaZnOS:Mn^{2+}$ for Sensing and Imaging Multiple Mechanical Stresses. *Opt. Express* **2013**, *21*, 12976–12986.

(156) Timilsina, S.; Lee, K. H.; Kwon, Y. N.; Kim, J. S. Optical Evaluation of In Situ Crack Propagation by Using Mechanoluminescence of $SrAl_2O_4:Eu^{2+},Dy^{3+}$. *J. Am. Ceram. Soc.* **2015**, *98*, 2197–2204.

(157) Wu, B.-Y.; Wang, H.-F.; Chen, J.-T.; Yan, X.-P. Fluorescence Resonance Energy Transfer Inhibition Assay for α-Fetoprotein Excreted during Cancer Cell Growth Using Functionalized Persistent Luminescence Nanoparticles. *J. Am. Chem. Soc.* **2011**, *133*, 686–688.

(158) Jia, F.; Li, G.; Yang, B.; Yu, B.; Shen, Y.; Cong, H. Investigation of Rare Earth Upconversion Fluorescent Nanoparticles in Biomedical Field. *Nanotechnol. Rev.* **2019**, *8*, 1–17.

(159) Li, Z.; Zhang, Y.; Wu, X.; Huang, L.; Li, D.; Fan, W.; Han, G. Direct Aqueous-Phase Synthesis of Sub-10 Nm "Luminous Pearls" with Enhanced in Vivo Renewable Near-Infrared Persistent Luminescence. *J. Am. Chem. Soc.* **2015**, *137*, 5304–5307.

(160) Nakauchi, D.; Okada, G.; Koshimizu, M.; Yanagida, T. Scintillation and Thermally-Stimulated Luminescence Properties of Pr-Doped $SrAl_2O_4$ Single Crystals. *Radiat. Meas.* **2017**, *106*, 170–174.

(161) Yanagida, T.; Fujimoto, Y.; Ito, T.; Uchiyama, K.; Mori, K. Development of X-Ray-Induced Afterglow Characterization System. *Appl. Phys. Express* **2014**, *7*, 062401.

(162) Wang, C.; Xuan, T.; Liu, J.; Li, H.; Sun, Z. Long Afterglow $SrAl_2O_4:Eu^{2+},Dy^{3+}$ Phosphors as Luminescent Down-Shifting Layer for Crystalline Silicon Solar Cells. *Int. J. Appl. Ceram. Technol.* **2015**, *12*, 722–727.

(163) Terraschke, H.; Wickleder, C. UV, Blue, Green, Yellow, Red, and Small: Newest Developments on Eu^{2+}-Doped Nanophosphors. *Chem. Rev.* **2015**, *115*, 11352–11378.

(164) Van den Eeckhout, K.; Smet, P. F.; Poelman, D. Persistent Luminescence in Rare-Earth Codoped $Ca_2Si_5N_8:Eu^{2+}$. *J. Lumin.* **2009**, *129*, 1140–1143.

(165) Smet, P. F.; Moreels, I.; Hens, Z.; Poelman, D. Luminescence in Sulfides: A Rich History and a Bright Future. *Materials* **2010**, *3*, 2834–2883.

(166) Pérez Salas, R.; Meléndrez, R.; Aceves, R.; Barboza-Flores, M. Nonthermoluminescent Dosimetry Based on the Afterglow Response of Europium-doped Alkali Halides. *Appl. Phys. Lett.* **1993**, *63*, 3017–3019.

(167) Rojas-Hernandez, R. E.; Rubio-Marcos, F.; Rodriguez, M. Á.; Fernandez, J. F. Long Lasting Phosphors: $SrAl_2O_4:Eu$, Dy as the Most Studied Material. *Renew. Sustain. Energy Rev.* **2018**, *81*, 2759–2770.

(168) Aitasalo, T.; Hölsä, J.; Jungner, H.; Lastusaari, M.; Niittykoski, J. Thermoluminescence Study of Persistent Luminescence Materials: Eu^{2+}- and R^{3+}-Doped Calcium Aluminates, $CaAl_2O_4:Eu^{2+},R^{3+}$. *J. Phys. Chem. B* **2006**, *110*, 4589–4598.

(169) Aitasalo, T.; Hölsä, J.; Jungner, H.; Lastusaari, M.; Niittykoski, J.; Parkkinen, M.; Valtonen, R. Eu^{2+} Doped Calcium Aluminates Prepared by Alternative Low Temperature Routes. *Opt. Mater. (Amst).* **2004**, *26*, 113–116.

(170) Chen, R.; Wang, Y.; Hu, Y.; Hu, Z.; Liu, C. Modification on Luminescent Properties of $SrAl_2O_4:Eu^{2+}$, Dy^{3+} Phosphor by Yb^{3+} Ions Doping. *J. Lumin.* **2008**, *128*, 1180–1184.

(171) Peng, T.; Yang, H.; Pu, X.; Hu, B.; Jiang, Z.; Yan, C. Combustion Synthesis and Photoluminescence of $SrAl_2O_4:Eu,Dy$ Phosphor Nanoparticles. *Mater. Lett.* **2004**, *58*,

352–356.

(172) Qiu, Z.; Zhou, Y.; Lü, M.; Zhang, A.; Ma, Q. Combustion Synthesis of Three-Dimensional Reticular-Structured Luminescence $SrAl_2O_4$:Eu,Dy Nanocrystals. *Solid State Sci.* **2008**, *10*, 629–633.

(173) Zhao, C.; Chen, D. Synthesis of $CaAl_2O_3$:Eu,Nd Long Persistent Phosphor by Combustion Processes and Its Optical Properties. *Mater. Lett.* **2007**, *61*, 3673–3675.

(174) Ghodsi, V.; Radovanovic, P. V. Turning Weakly Luminescent SnO_2 Nanocrystals into Tunable and Efficient Light Emitters by Aliovalent Alloying. *Chem. Mater.* **2018**, *30*, 3578–3587.

(175) Simmons, J. G. Generalized Thermal J-V Characteristic for the Electric Tunnel Effect. *J. Appl. Phys.* **1964**, *35*, 2655–2658.

(176) Norris, D. J.; Efros, A. L.; Erwin, S. C. Doped Nanocrystals. *Science* **2008**, *319*, 1776–1779.

(177) Bryan, J. D.; Gamelin, D. R. Doped Semiconductor Nanocrystals: Synthesis, Characterization, Physical Properties, and Applications; 2005; pp 47–126.

(178) Farvid, S. S.; Dave, N.; Wang, T.; Radovanovic, P. V. Dopant-Induced Manipulation of the Growth and Structural Metastability of Colloidal Indium Oxide Nanocrystals. *J. Phys. Chem. C* **2009**, *113*, 15928–15933.

(179) Layek, A.; Yildirim, B.; Ghodsi, V.; Hutfluss, L. N.; Hegde, M.; Wang, T.; Radovanovic, P. V. Dual Europium Luminescence Centers in Colloidal Ga_2O_3 Nanocrystals: Controlled in Situ Reduction of Eu(III) and Stabilization of Eu(II). *Chem. Mater.* **2015**, *27*, 6030–6037.

(180) Wang, T.; Layek, A.; Hosein, I. D.; Chirmanov, V.; Radovanovic, P. V. Correlation between Native Defects and Dopants in Colloidal Lanthanide-Doped Ga_2O_3 Nanocrystals: A Path to Enhance Functionality and Control Optical Properties. *J. Mater. Chem. C* **2014**, *2*, 3212–3222.

(181) Playford, H. Y.; Hannon, A. C.; Barney, E. R.; Walton, R. I. Structures of Uncharacterised

Polymorphs of Gallium Oxide from Total Neutron Diffraction. *Chem. - A Eur. J.* **2013**, *19*, 2803–2813.

(182) Clabau, F.; Rocquefelte, X.; Le Mercier, T.; Deniard, P.; Jobic, S.; Whangbo, M.-H. Formulation of Phosphorescence Mechanisms in Inorganic Solids Based on a New Model of Defect Conglomeration. *Chem. Mater.* **2006**, *18*, 3212–3220.

(183) Kaewjaeng, S.; Kaewkhao, J.; Chanthima, N.; Ruangtawep, Y.; Klysubun, W.; Kothan, S.; Kim, H. J. XANES and Luminescence Studies of M_2O_3-CaO-SiO_2-B_2O_3 ($M_2O_3 = Y_2O_3$ and La_2O_3) Glasses Doped with Dy^{3+} Ions. *Key Eng. Mater.* **2018**, *780*, 37–42.

(184) Balerna, A.; Bernieri, E.; Burattini, E.; Kuzmin, A.; Lusis, A.; Purans, J.; Cikmach, P. XANES Studies of MeO_{3-x} (Me = W, Re, Ir) Crystalline and Amorphous Oxides. *Nucl. Instruments Methods Phys. Res. Sect. A Accel. Spectrometers, Detect. Assoc. Equip.* **1991**, *308*, 240–242.

(185) Sudarsan, V. Optical Materials: Fundamentals and Applications. In *Functional Materials*; Banerjee, S., Tyagi, A. K., Eds.; Elsevier, 2012; pp 285–322.

(186) Suib, S. L.; Tauaka, J. Preparation of a Phosphor, $ZnA:Cu^{2+}$. *J. Chem. Educ.* **1984**, *61*, 1099–1101.

(187) Hoogenstraaten, W.; Klasens, H. A. Some Properties of Zinc Sulfide Activated with Copper and Cobalt. *J. Electrochem. Soc.* **1953**, *100*, 366–375.

(188) Sahu, I. P.; Bisen, D. P.; Brahme, N.; Tamrakar, R. K.; Shrivastava, R. Luminescence Studies of Dysprosium Doped Strontium Aluminate White Light Emitting Phosphor by Combustion Route. *J. Mater. Sci. Mater. Electron.* **2015**, *26*, 8824–8839.

(189) Lisensky, G. C.; Patel, M. N.; Reich, M. L. Experiments with Glow-in-the-Dark Toys: Kinetics of Doped ZnS Phosphorescence. *J. Chem. Educ.* **1996**, *73*, 1048–1051.

(190) Getz, W. A.; Wentzel, D. A.; Palmer, M. J.; Campbell, D. J. Erasing the Glow in the Dark: Controlling the Trap and Release of Electrons in Phosphorescent Materials. *J. Chem. Educ.* **2018**, *95*, 295–299.

(191) Zitoun, D.; Bernaud, L.; Manteghetti, A.; Filhol, J.-S. Microwave Synthesis of a Long-

Lasting Phosphor. *J. Chem. Educ.* **2009**, *86*, 72–75.

(192) Ma, Y.-Z.; Jia, L.; Ma, K.-G.; Wang, H.-H.; Jing, X.-P. Preparing, Characterizing, and Investigating Luminescent Properties of a Series of Long-Lasting Phosphors in a SrO–Al$_2$O$_3$ System: An Integrated and Inquiry-Based Experiment in Solid State Chemistry for the Undergraduate Laboratory. *J. Chem. Educ.* **2017**, *94*, 1157–1162.

(193) Ghodsi, V.; Layek, A.; Hegde, M.; Yildirim, B.; Radovanovic, P. V. Native Defects Determine Phase-Dependent Photoluminescence Behavior of Eu^{2+} and Eu^{3+} in In$_2$O$_3$ Nanocrystals. *Chem. Commun.* **2016**, *52*, 4353–4356.

Appendix A.   Additional Data from Chapter 2
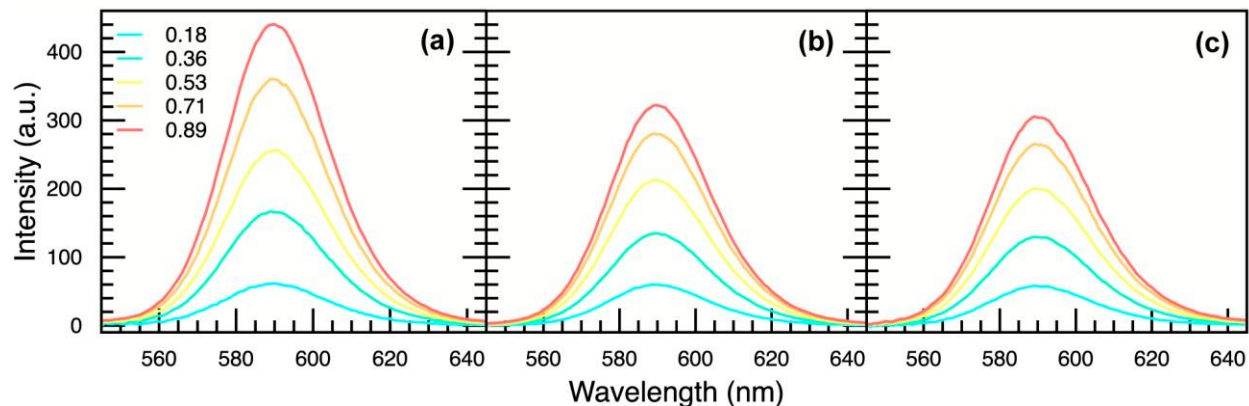
Figure A.1. Photoluminescence spectra of CdSe/CdS nanocrystals (NCs) in (a) nanocrystal conjugate, linked with thioglycolic acid (TGA), upon correction for the contribution from Ga_2O_3 NC emission, (b) pure CdSe/CdS nanocrystal suspension, and (c) mixture of Ga_2O_3 and CdSe/CdS NCs without the TGA linker. The concentrations of CdSe/CdS NCs are identical in all panels, and are expressed in (a) as a [CdSe/CdS]/[Ga_2O_3] ratio. The excitation wavelength is 250 nm for all spectra.
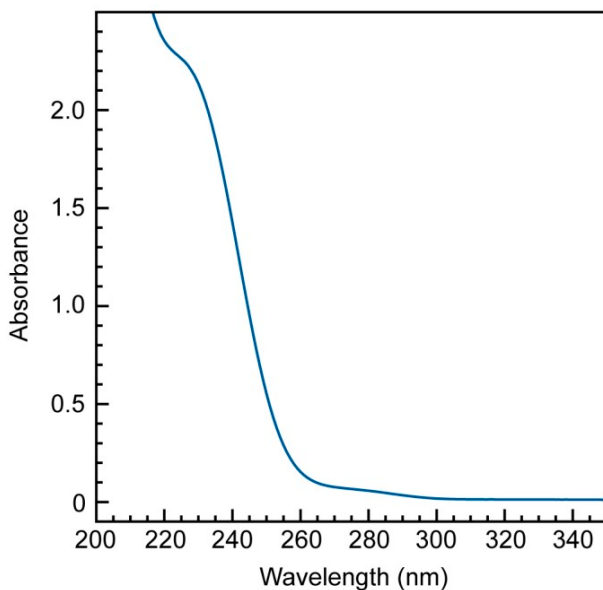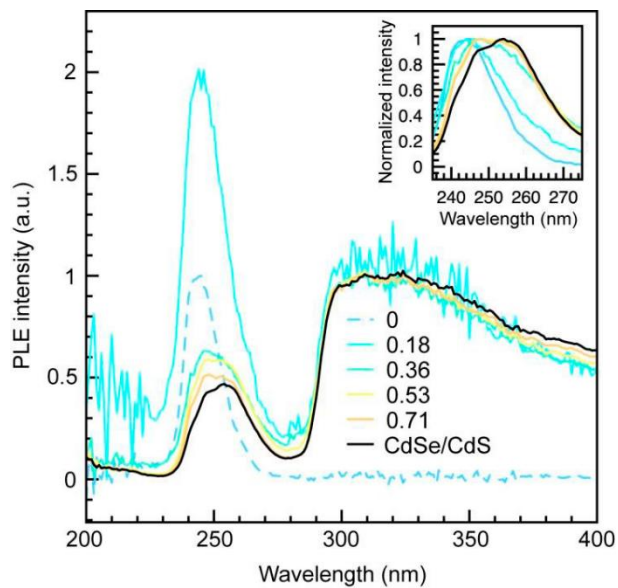

Figure A.2. Photoluminescence excitation (PLE) spectra of CdSe/CdS-Ga_2O_3 NC conjugates having different acceptor to donor ratio, as indicated in the graph (λ_{em} = 590 nm). PLE spectra of Ga_2O_3 and CdSe/CdS NCs are shown with dashed blue and solid black lines, respectively. Inset: Normalized PLE spectra in the region corresponding to Ga_2O_3 NC excitation. The dip in the excitation spectra at ca. 280 nm is due to absorption of tetrahydrofuran (THF) in that region.

Figure A.3. Photoluminescence excitation (PLE) spectra of CdSe/CdS-Ga$_2$O$_3$ NC conjugates having different acceptor to donor ratio, as indicated in the graph (λ_{em} = 590 nm). PLE spectra of Ga$_2$O$_3$ and CdSe/CdS NCs are shown with dashed blue and solid black lines, respectively. Inset: Normalized PLE spectra in the region corresponding to Ga$_2$O$_3$ NC excitation. The dip in the excitation spectra at ca. 280 nm is due to absorption of tetrahydrofuran (THF) in that region.
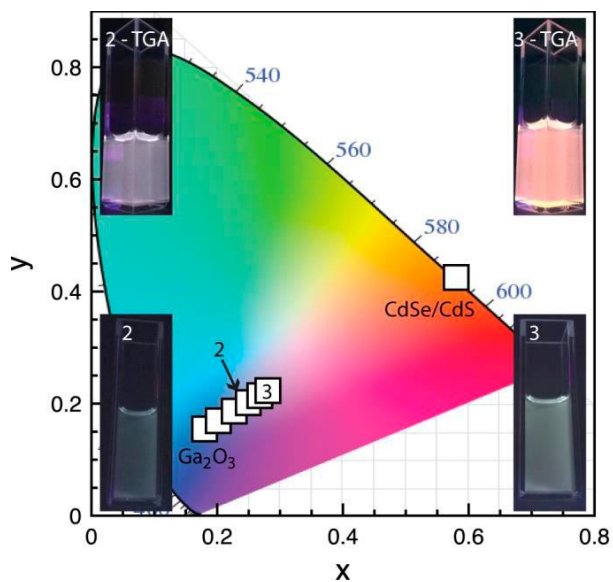
Figure A.4. International Commission on Illumination 1931 (CIE 1931) color space diagram for suspensions containing a mixture of CdSe/CdS and Ga$_2$O$_3$ NCs. The mixtures are prepared in an identical way to the samples shown in Figure 2.7 in Chapter 2, but without the TGA linker. Bottom insets show photographs corresponding to points 2 and 3 in the graph. The photographs of analogous samples for the NC conjugates are shown as top insets for comparison.

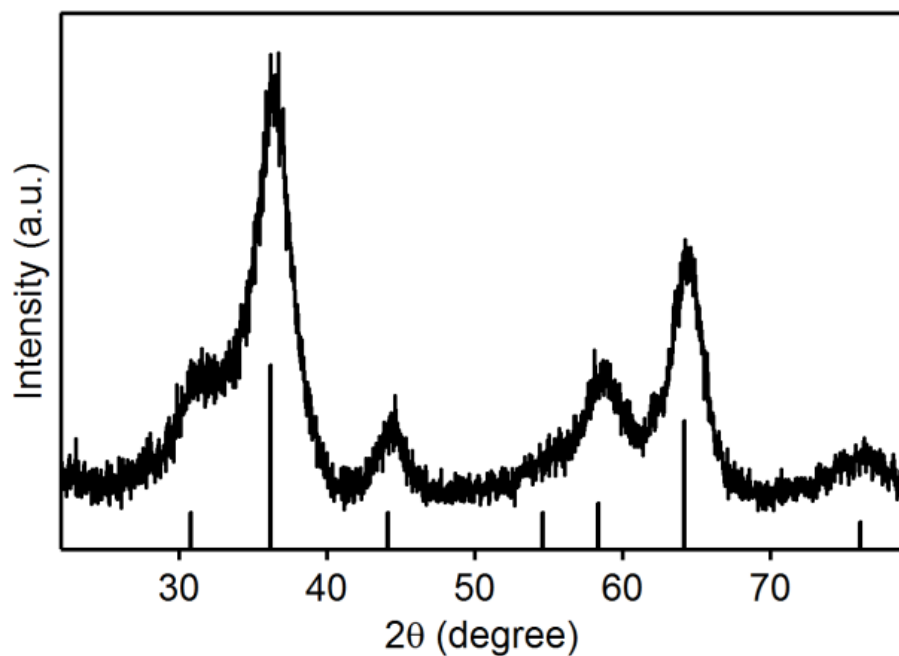# Appendix B.　　Additional Data from Chapter 3

Figure B.1. XRD pattern of Ga₂O₃ NCs used for the preparation of composite NC films. Vertical lines indicate the XRD pattern of bulk γ-Ga₂O₃ (JCPDS 20-0426).
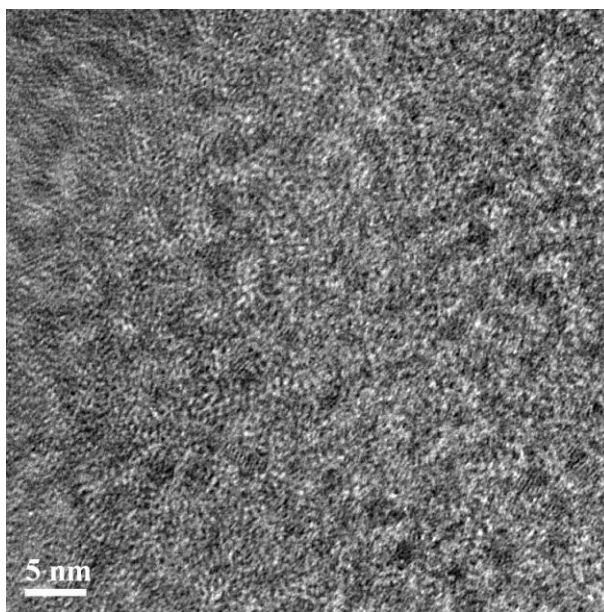

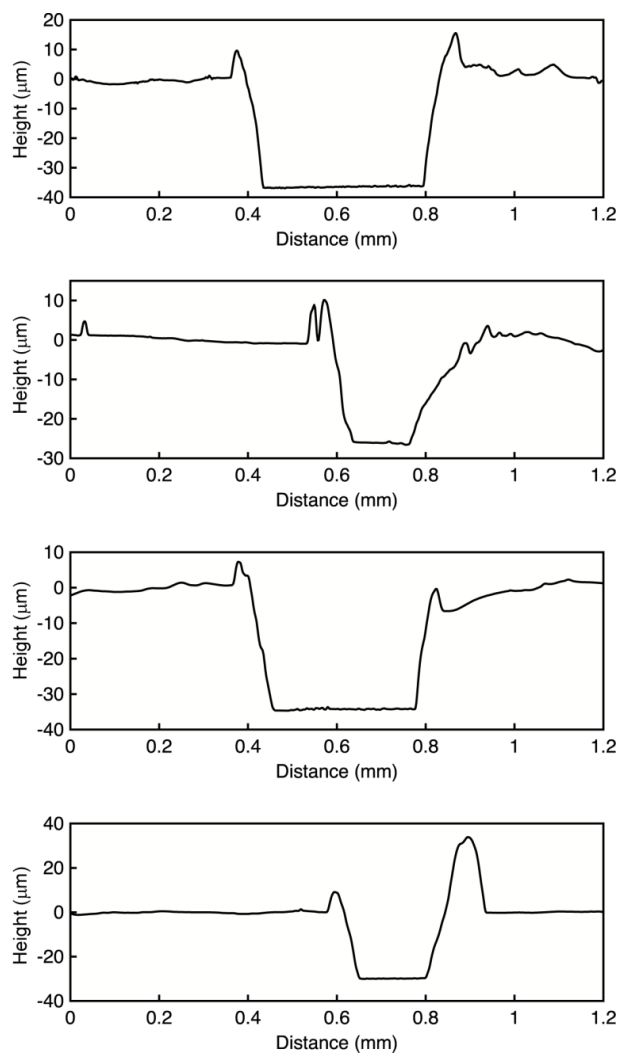*Figure B.2. TEM image of CdSe NCs used as cores for the preparation of CdSe/CdS core/shell NCs.*

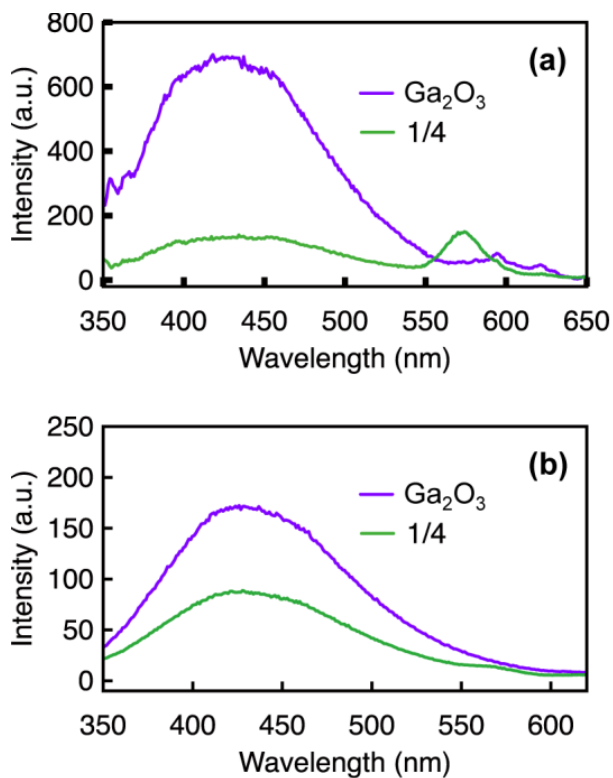*Figure B.3. Thickness profiles of Ga₂O₃-CdSe/CdS composite NC films for different regions on the substrate.*

Figure B.4. (a) PL spectrum of composite NC film having acceptor to donor concentration ratio of 1/4 ([CdSe/CdS]/[Ga₂O₃]=1/4). The spectrum of a NC film prepared solely with Ga₂O₃ NCs is shown for comparison. (b) PL spectrum of a colloidal NC mixture used to prepare the composite film in (a) ([CdSe/CdS]/[Ga₂O₃]=1/4). PL spectrum of colloidal Ga₂O₃ NCs containing the same amount of Ga₂O₃ NCs is shown for comparison. Codeposition of Ga₂O₃ and CdSe/CdS NCs on a substrate leads to quenching of Ga₂O₃ DAP emission together with an increase in CdSe/CdS NC emission intensity.

Appendix C. Additional Information for Chapter 4
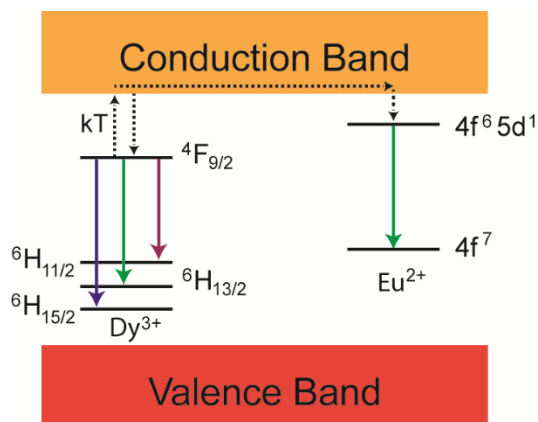
C.1. Supporting Figures

Figure C.1. Schematic representation of the electronic structure, electron trapping/detrapping processes (dashed arrows), and photoluminescence transitions (solid arrows) in SrAl$_2$O$_4$ codoped with Eu^{2+} and Dy^{3+}.
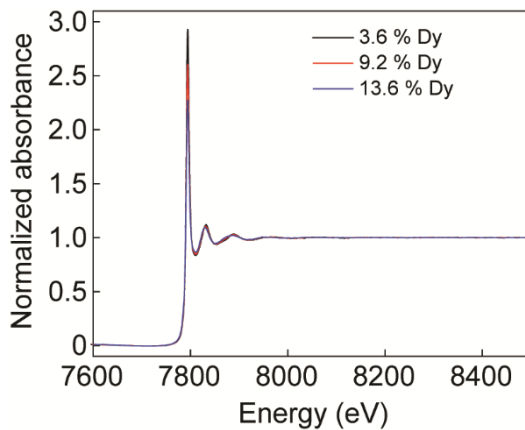

Figure C.2. Overview Dy L$_3$-edge X-ray absorption spectrum of Dy^{3+}-doped Ga$_2$O$_3$ nanocrystals having different doping concentrations, as indicated in the graph.

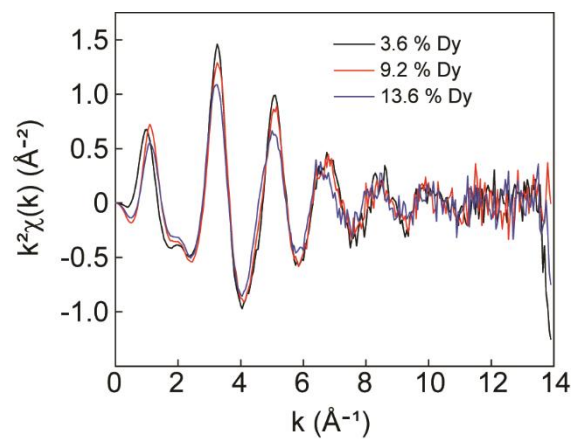*Figure C.3. Background-corrected Dy L₃-edge EXAFS spectra of Dy³⁺-doped Ga₂O₃ nanocrystals having different doping concentrations, as indicated in the graph.*

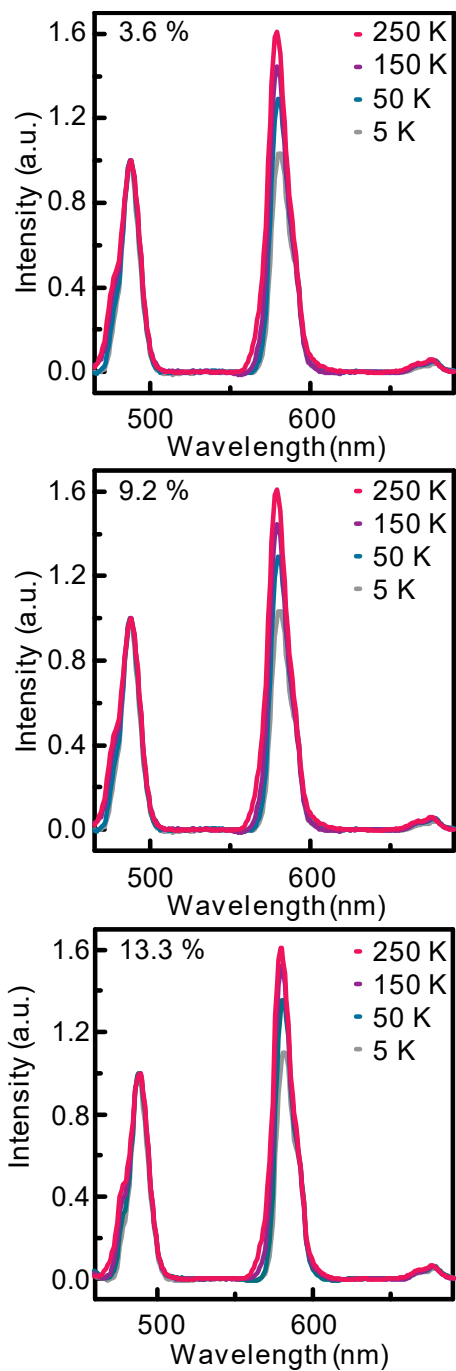*Figure C.4. Time-gated PL spectra of Dy^{3+}-doped Ga$_2$O$_3$ nanocrystals having doping concentrations of (a) 3.6 %, (b) 9.2 %, and (c) 13.3 %. The spectra were collected at different temperatures, as indicated in the graphs. Assignment of the characteristic Dy^{3+} intra-4f transitions are shown in Figure 4.2d in the main text. The spectra were collected for a delay time of 0.2 ms and detection window of 5 ms.*
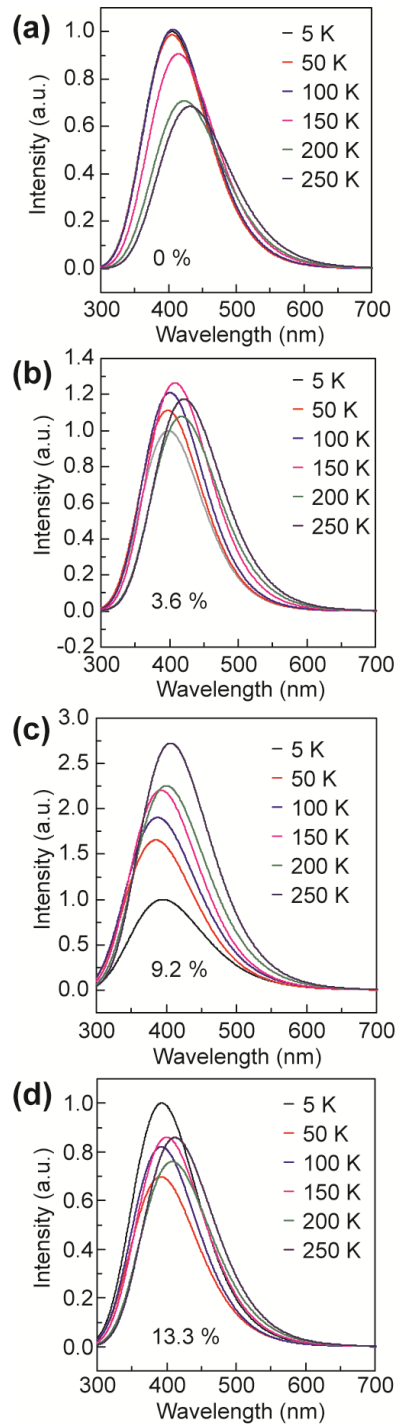
Figure C.5. PL spectra of Dy^{3+}-doped Ga$_2$O$_3$ nanocrystals having different doping concentrations, and collected at different temperatures from 5 to 250 K, as indicated in the graphs. The spectra are dominated by Ga$_2$O$_3$ DAP PL band.

117

Figure C.6. DAP emission intensity dependence on temperature for Ga_2O_3 nanocrystals. Solid line represented best fit of Equation 4.5 in the main text.

Figure C.7. (a) Experimental data and (b) Monte Carlo simulation for Ga_2O_3 nanocrystal time-resolved DAP PL intensity.

C.2.   Supporting Tables
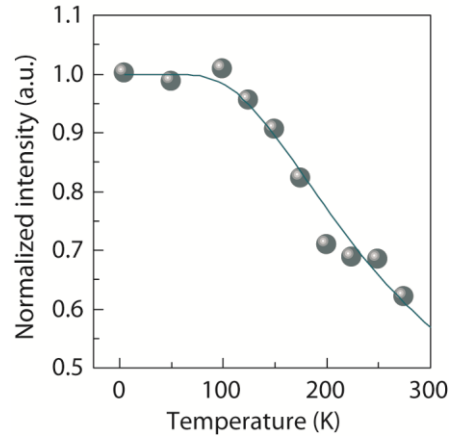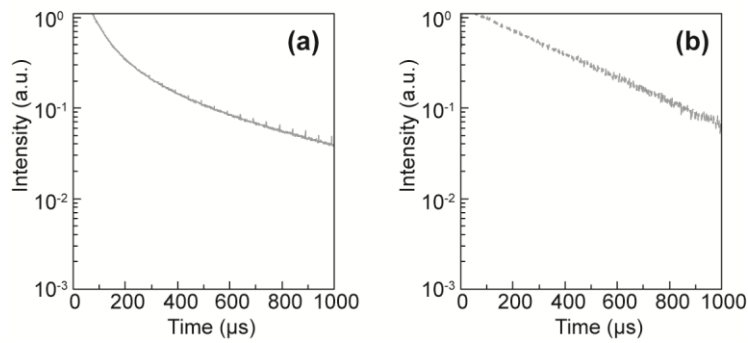
Table C.1. Parameters Obtained by Fitting Varshni's Law to the Experimental Data.

Doping conc. (%)	α ($\times 10^3$ eV/K)	β (K)	E (eV)
0	-2.2386	457	3.07
3.6	-1.972	507	3.11
9.2	-3.7730	1190	3.21

Table C.2. Ga_2O_3 nanocrystal size as determined by TEM.

Doping conc. (%)	Average Size (nm)
0	5.5±0.4
3.6	5.1±0.4
9.2	4.5±0.4
13.2	4.1±0.4

C.3.   Additional Discussion

Monte Carlo simulations were performed by considering the probability (or rate) of all possible electron transitions shown in Figure 4.6a in the main text. Undoped Ga_2O_3 NCs were used to assess the validity of the simulation, which was then run for a 3.6 % Dy^{3+} doping concentration.

In the simulation, one million electrons were excited from the valence to the conduction band. The probability that an excited electron in the conduction band relaxed to an oxygen vacancy site was empirically determined based on the Monte Carlo simulated PL intensity at high temperatures. When the probability that an electron is trapped on a donor site is too low, thermal quenching of the DAP emission becomes more pronounced, because more thermally reactivated electrons in the conduction band recombine non-radiatively (Figure C.8a). On the other hand, when the probability of trapping an electron on a donor site is too high (Figure C.8b), thermal quenching of the DAP emission is underestimated.
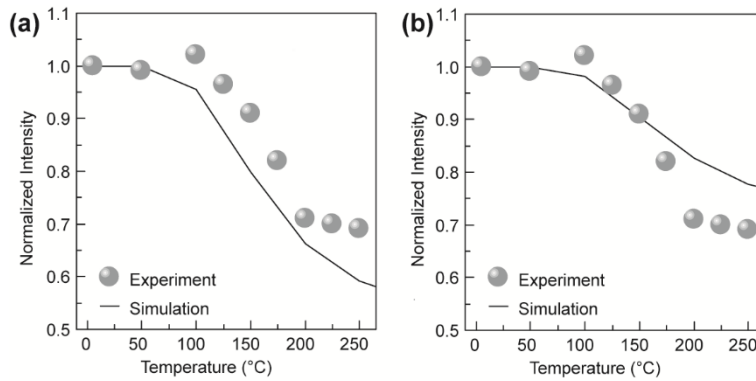

Figure C.8. Comparison of the temperature-dependent DAP PL intensity data with the results of the Monte Carlo simulation when the probability of trapping a conduction band electron at a donor site (i.e., oxygen vacancy) is (a) too low, and (b) too high.

The 0 K tunneling probability (J_{V_0}) described by Equation 4.3 in the main text was determined by matching the predicted DAP PL time-decay profile with the experimental data for 5 K. This is a reasonable approximation because there is little change in the predicted decay rate between 5 and 50 K, and there should be even less from 5 to 0 K. The temperature dependence of this rate (J_{V_T}) was set by matching the predicted lifetime range to the experimental data (an example is shown in Figure C.7). It should be noted that even though these two parameters (J_{V_0} and J_{V_T}) were set based on kinetic properties, they still affect thermal quenching. When the DAP

120

tunnel transfer probability is reduced, the optimal PL quenching is stronger than experimentally

observed, and the decrease in PL intensity with temperature occurs more sharply because trapped

electrons have more time to be reactivated to the conduction band. When the DAP probability is

higher than achievable for a given trap depth, there is very little quenching over this temperature
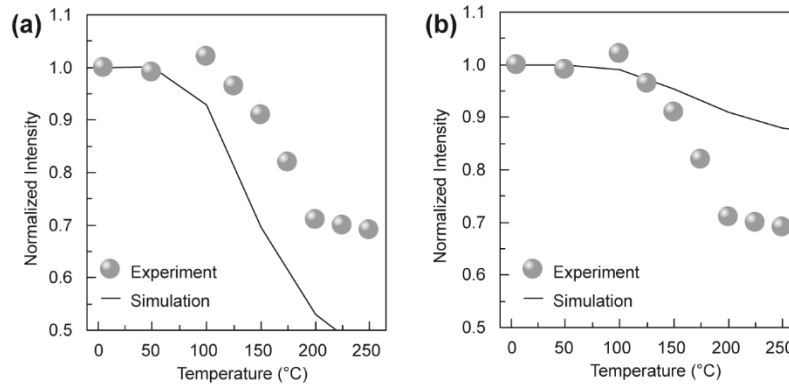
range.

Figure C.9. Comparison of the temperature-dependent DAP PL intensity data with the results of the Monte Carlo simulation when the 0 K tunneling rate (J_{V_0}) is (a) too low, and (b) too high.

Our model assumes that the non-radiative relaxation of excited electrons in the conduction

band is the only mechanism that competes with their trapping in the donor states and subsequent

DAP emission. Hence, when this non-radiative relaxation is low, electrons are more likely to relax

radiatively through the DAP recombination. As the temperature is increased, the electrons

originally trapped on oxygen vacancies are thermally excited back to the conduction band and

have an additional opportunity to relax non-radiatively. This is manifested through plateauing of

the DAP emission intensity with increasing temperature (Figure C.10). The relative DAP PL

intensity at which plateauing occurs is overestimated (underestimated) when the likelihood of

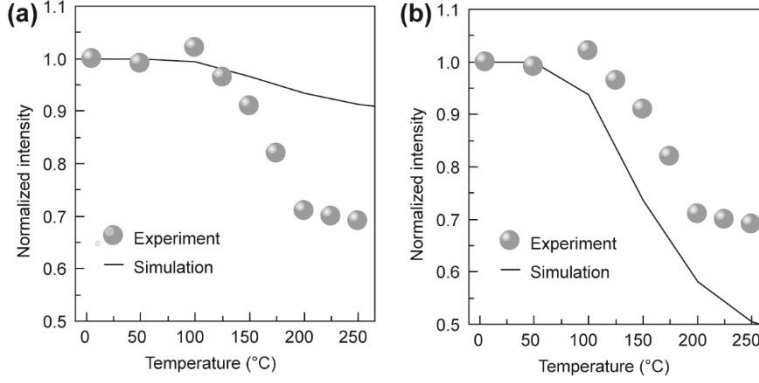conduction band electron non-radiative relaxation is too low (too high).

Figure C.10. Comparison of the temperature-dependent DAP PL intensity data with the results of the Monte Carlo simulation when the non-raditative relaxation rate is (a) too low, and (b) too high.

Once all these parameters are found and the simulation for undoped Ga_2O_3 was in good agreement with the experimental results, the possibility of electron trapping to Dy^{3+} was incorporated into the model. The concentration of Dy^{3+} was determined by EDX, and the probability of electron trapping on a Dy^{3+} site was treated in the same way as the probability of electron trapping on an oxygen vacancy. Therefore, the fraction of electrons trapped on Dy^{3+} is simply proportional to the doping concentration. The total amount of electrons relaxing to the trap states was held constant despite doping, so the amount of electrons relaxing from the conduction band to an oxygen vacancy (n_{V_O}) in doped NCs was:

$$n_{V_O} = n_{tot} - n_{Dy*}$$

where n_{tot} is the amount of excited electrons, and n_{Dy*} is the amount of electrons relaxing to Dy^{3+} excited state ($Dy*$).

The trap depth of Dy^{3+} was set empirically based on the temperature at which DAP emission started increasing. If the Dy^{3+} trap was too shallow, the increase in the DAP PL intensity was sharper at lower temperatures. On the other hand, if the trap was set too deep, reactivation

122

from Dy^{3+} occurred at the same temperature as that from oxygen vacancy, so the repopulation of oxygen vacancies was partially offset.
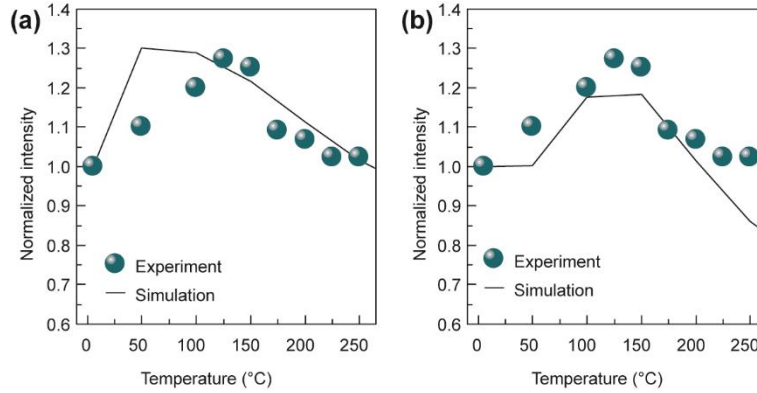

Figure C.11. Comparison of the temperature-dependent DAP PL intensity data with the results of the Monte Carlo simulation when Dy^{3+} trap is (a) too shallow, and (b) too deep.

Since the lifetime of Dy^{3+} emission is significantly longer than that of DAP emission, Dy* population was treated as a Boltzmann distribution having a high internal relaxation barrier. If the internal relaxation barrier is smaller than the binding energy of electrons of Dy^{3+}, the thermal behavior of DAP appeared the same as for undoped NCs (Figure C.12a). When the internal relaxation barrier is approximately equal to the Dy^{3+} trap depth there is a small increase in DAP emission, however, this increase is smaller than that found experimentally because there are still fewer electrons reaching the donor trap state. When the internal relaxation barrier was significantly larger than the Dy^{3+} trap depth the Monte Carlo simulation was in agreement with the experimental results. After a critical point there is very little additional effect on the thermal behavior of Ga$_2$O$_3$.
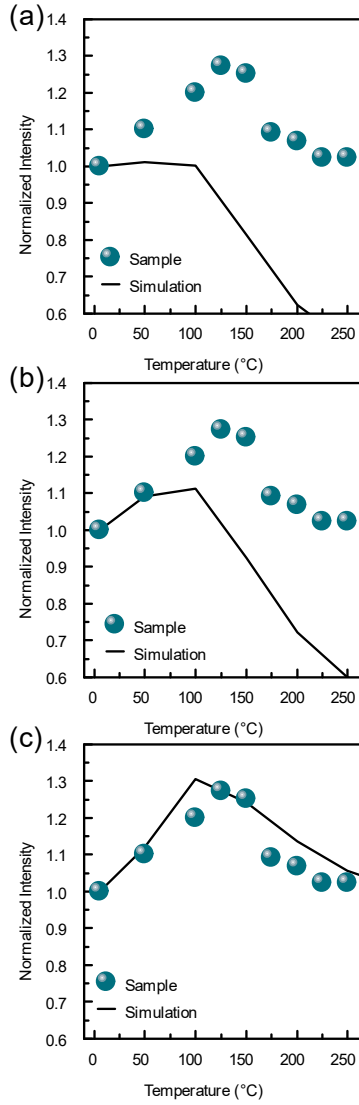
Figure C.12. Experimental temperature dependent photoluminencent data with the results of Monte Carlo simulations when (a) the Dy^{3+} internal relaxation barrier is less than the trap depth, (b) equal to the trap depth, (c) and significantly higher than the trap depth and the
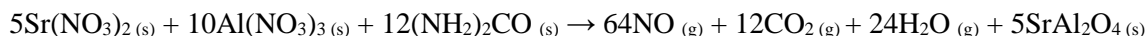
Appendix D. Instructor Note for the Evaluation of Students on the Synthesis and Characterization of Eu,Dy:SrAl$_2$O$_4$

NE 320L Strontium Aluminate Doped with Europium and Dysprosium: Prelaboratory Questions
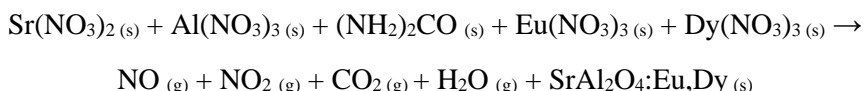
* You will need to retain a copy of the prelab calculations for yourself to know the amounts of each the various reactants to weigh out.

1. Given the balanced chemical reaction of strontium aluminate from Equation 1 from the manual:
2.

$$5Sr(NO_3)_{2\,(s)} + 10Al(NO_3)_{3\,(s)} + 12(NH_2)_2CO_{\,(s)} \rightarrow 64NO_{\,(g)} + 12CO_{2\,(g)} + 24H_2O_{\,(g)} + 5SrAl_2O_{4\,(s)}$$

Balance the following chemical reaction taking into account that the end goal is to have 2% Dy and 1 % Eu substituting Sr. *Hint: The rare earth metals have the same charge as aluminum and can be treated as such until you give your final answer.* **(6 marks)**

$$Sr(NO_3)_{2\,(s)} + Al(NO_3)_{3\,(s)} + (NH_2)_2CO_{\,(s)} + Eu(NO_3)_{3\,(s)} + Dy(NO_3)_{3\,(s)} \rightarrow$$

$$NO_{\,(g)} + NO_{2\,(g)} + CO_{2\,(g)} + H_2O_{\,(g)} + SrAl_2O_4{:}Eu,Dy_{\,(s)}$$

3. In this laboratory experiment, we will using be one gram total of the metallic (not including urea) precursors and a 50% excess of urea. Calculate the mass of all materials needed for this experiment and enter them into the table below: *Note: only the entries in the last column will be marked, the others are just to assist in your calculations* **(10 marks)**

Compound	# Moles	Molar Mass (g/mol)	Mass for Lab (g)
Sr(NO$_3$)$_2$ anhydrous			
Al(NO$_3$)$_3$ • 9H$_2$O			
Eu(NO$_3$)$_3$ • 6H$_2$O			
Dy(NO$_3$)$_3$ • 5H$_2$O			

(NH$_2$)$_2$CO			

4. Distinguish the difference in the roles of the two dopants, europium and dysprosium in the SAED phosphorescence compound? **(2 marks)**

5. Explain the purpose of annealing the SAED product at 1000 °C in the presence of hydrogen gas. **(2 marks)**

NE 320L Strontium Aluminate Doped with Europium and Dysprosium: Prelaboratory Safety Questions

1. Students can take their vials in and out of the furnace with their bare hands True/False

 2. Shorts and/or sandals are sufficient attire for the laboratory period.

True/False

3. Any student who is late and misses the pre-laboratory discussion or who does not perform the safety quiz prior to 8:30am on the day of the laboratory period will not be permitted to carry out the laboratory exercise, and will receive a grade of zero for that laboratory exercise.

True/False

4. Gloves must be worn at all times during this laboratory exercise when handling the materials and samples to be investigated.

True/False

5. Wearing safety glasses and proper safety attire (especially not sandals and shorts) is required at all times in the laboratory setting, with noncompliance having the consequence of students not being admitted into the laboratory plus the receipt of a grade of zero.

True/False

NE 320L Laboratory Characterization Methods

Laboratory Exercise 1
Strontium Aluminate Doped with Europium and Dysprosium

By:
Student Number:
Laboratory Partner:

Laboratory Performed

Submission date:

Submitted to:

Give the SEM images of the SAED sample. Give an approximate particle size based on these images. (4 marks)

Plot out the powder XRD pattern for your SAED sample. Compare your pattern to the diffraction pattern of $SrAl_2O_4$ given on LEARN. Discuss whether there should or should not be any differences between these two patterns. (6 marks)

Give a reason why the rare earth metals replace strontium as opposed to aluminum. (2 marks)

How would the lifetime of these nanoparticles be affected if their lifetimes were measured at a) higher temperature; b) lower temperature. If these nanoparticles were excited near 0 K, what would they look like? What would happen as they were brought back to room temperature? (8 marks)

Representative Student Data

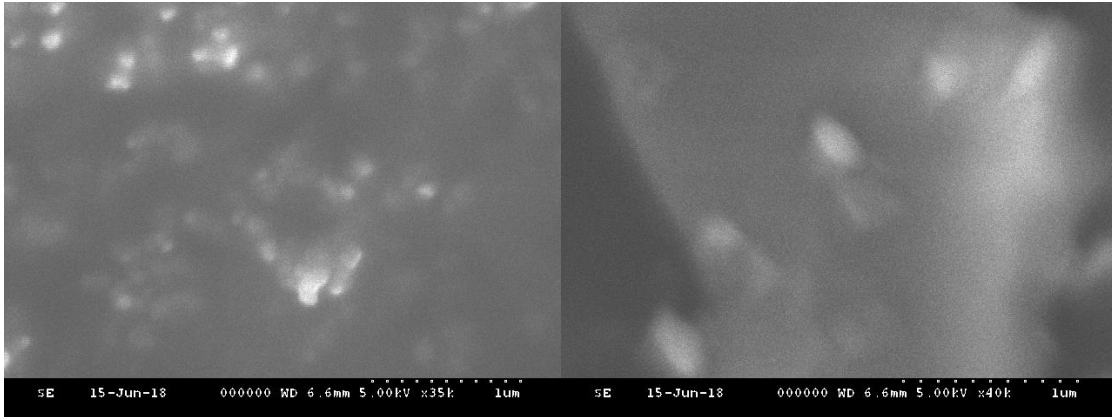**Scanning electron microscopy (SEM) images**

Figure D.1. SEM images of "crude" SAED samples (before annealing) collected from different areas of the specimen.
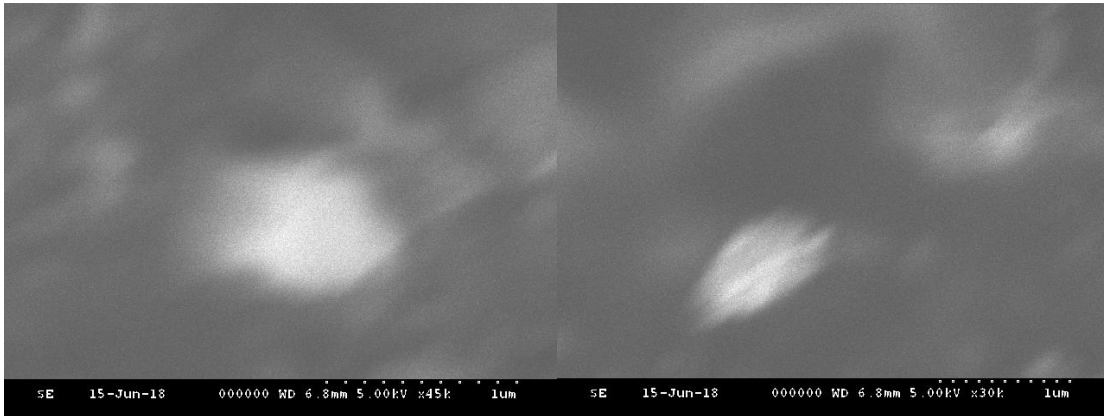

Figure D.2. SEM images of the annealed SAED sample collected at different ares of the specimen.

Table D.1. Particle diameters measured from SEM images.

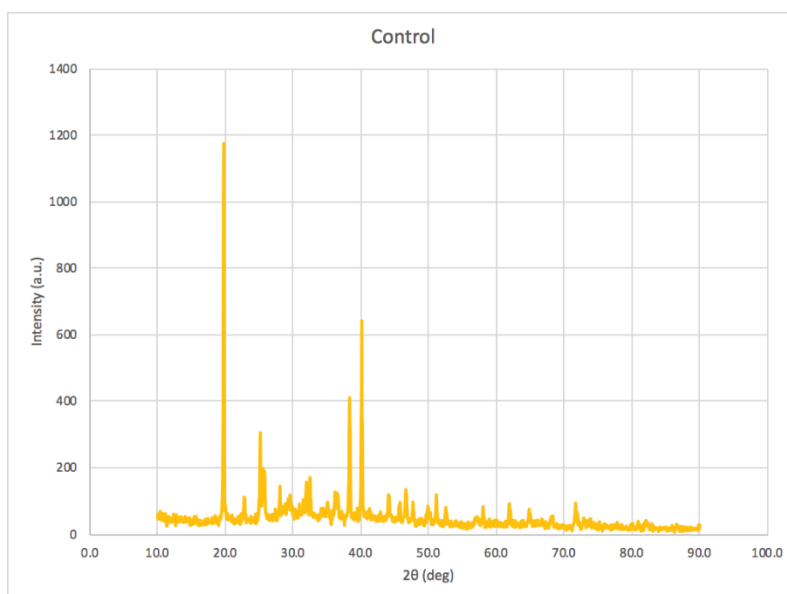| Sample	Measured Particle Diameter (nm)	Average Particle Diameter (nm)	Particle Diameter Standard Deviation (nm)
Crude	104, 141, 135, 101, 49, 99, 49, 67, 47, 62, 79, 67, 49, 58, 49, 53, 67, 126, 61, 77, 78, 86, 88, 142, 212, 133, 149, 88, 147	92	41
Annealed	113, 69, 94, 97, 133	101	24

X-ray diffraction (XRD) Patterns

Figure D.3. XRD pattern of crude SEAD sample.

131
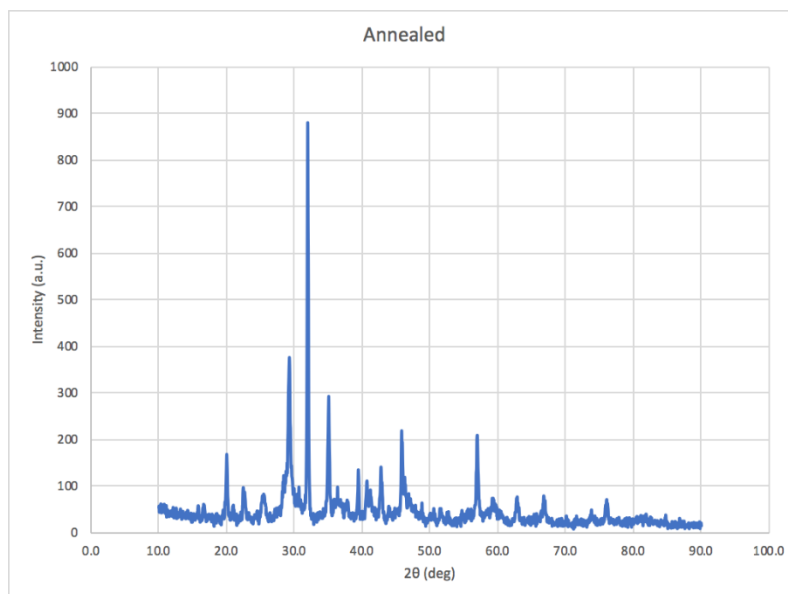
Figure D.4. XRD pattern of annealed SAED sample.

Representative data for mechanoluminescence measurements as well as observed thermoluminescence and phosphorescence are given in the main article.

"Idealized" Author Data

SEM images
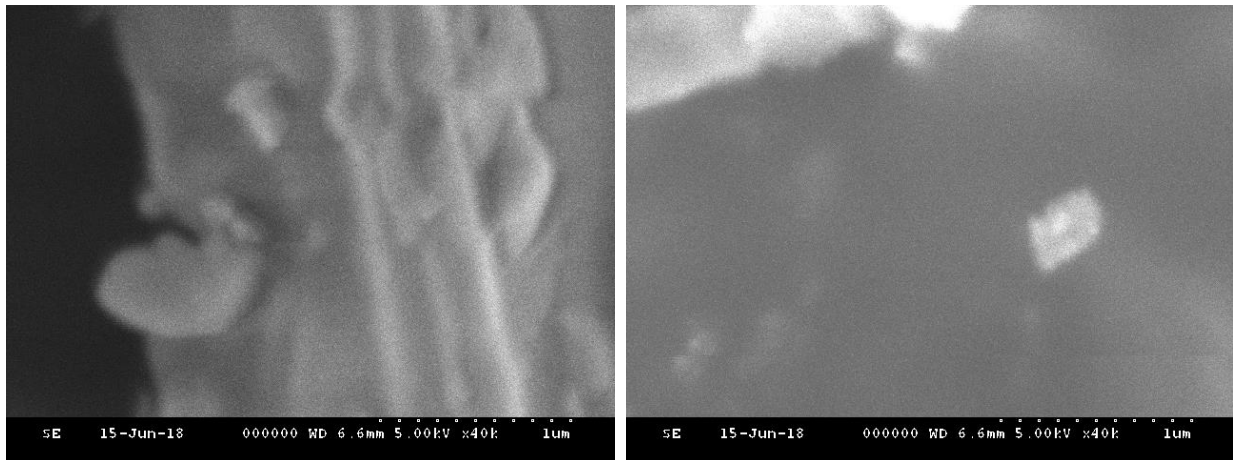
Figure D.5. SEM images of "crude" SAED samples (before annealing) collected from different areas of the specimen.
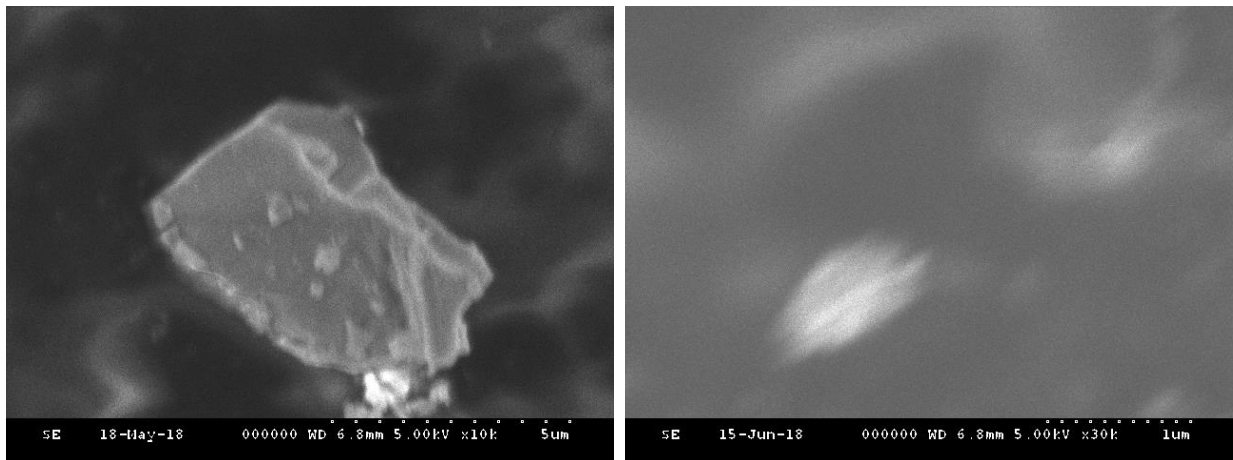
.

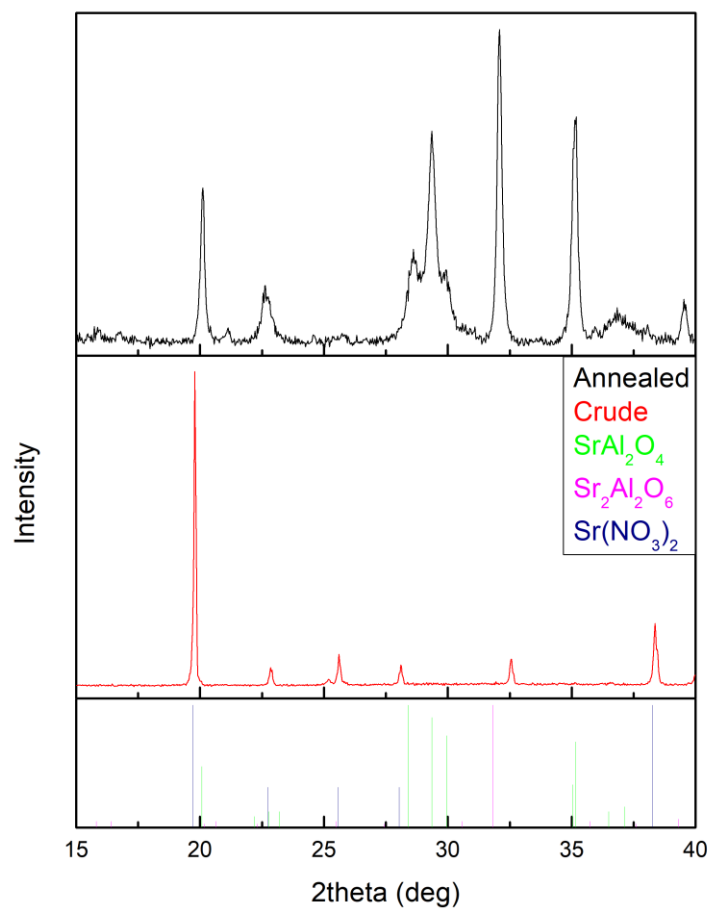*Figure D.6. SEM images of the annealed SAED sample collected at different ares of the specimen.*

Figure D.7 XRD patterns of crude (bottom) and annealed (top) SAED samples. The markers for bulk patterns for different phases relevant for this material and synthesis/processing method are shown with vertical colored lines as indicated in the inset.

Additional Instructor Notes

Experimental Notes

Materials. Aluminum nitrate nonahydrate (99.9 %) and anhydrous strontium nitrate (99.9 %) were purchased from Fisher Chemical. Dysprosium(III) nitrate pentahydrate (99.9 %) and europium(III) nitrate hexahydrate (99.9 %) were purchased from Alfa Aesar. Urea (reagent grade) was purchased from Merck. All reagents were used as received, without further purification.

SrAl$_2$O$_4$:Eu,Dy (SAED) Phosphor Synthesis. Stoichiometric amounts of all metal precursors totalling 1 g of sample were combined in a 20 mL glass vial with a 50 mol% excess of urea and dissolved in a minimum amount of water. Typically, two samples were prepared in parallel, one for further treatment by annealing and the other one for comparison. The vials were placed in a muffle furnace preheated to 500 °C using long metal tongs and left for ca. 10 min until the reaction was completed. The vials were then removed from the furnace using tongs and allowed to cool to room temperature on a metal plate, after which the contents were transferred to a mortar. Using the mortar and pestle, the ash-like products were ground into a fine powder with one sample being placed in an alumina crucible for annealing and the other stored in a separate vial labeled "crude". The product in the alumina boat was then heated to 1000 °C over 15 min, where it was held for an hour under a gentle gas flow of a mixture of N$_2$ (flow rate of 520 sccm) and H$_2$ (flow rate of 60 sccm). After annealing, the sample was allowed to cool before once again grinding with a mortar and pestle. This product was placed in another glass vial labelled "annealed". Both "crude" and "annealed" samples were then stored until the characterization session.

Sample Characterization. Scanning electron microscopy (SEM) imaging was performed using a Hitachi S-3500M microscope. The specimens were prepared by sprinkling a minimum amount of the dry sample on conductive carbon tape affixed to an aluminum SEM sample mount. Powder X-ray diffraction (XRD) measurements were performed with a Panalytical

X'Pert PRO diffractometer. A thin layer of the remaining amount of sample was pressed onto an aluminum sample holder using a glass slide. The glass slide was then held fixed to the aluminum plate with the sample sandwiched in-between to prevent a loss during transport, before being removed during XRD measurement. Proper SEM imaging technique was demonstrated for each group of students by the course instructor for ca. 30 mins, after which they split into two pairs. Two students were given the opportunity to capture SEM images of their samples, while the other two students were shown how to collect XRD data by their Teaching Assistant, and were subsequently required to match the results of the acquired patterns to native X'Pert HighScoreXRD library and identify the obtained material. After 30 minutes, the two pairs of students rotated in order to gain experience with both SEM and XRD measurements and analyses.

   Thermoluminescence and Mechanoluminescence Experiments. For thermoluminescence experiment, a SAED-embedded polymer film was illuminated for a few minutes with a UVP UVL-18EL Series UV lamp at 365 nm which was subsequently turned off. A warm object (e.g., a hand or a beaker of hot water) is then placed on the glowing polymer film, and the difference between areas that were heated and those that were not heated was observed and recorded. An alternative way of performing this experiment could be using commercially available products, such as decorating glowing stickers.

   The set-up for mechanolumoescence measurements was homebuilt from commercially available components, as shown in Figure 5.4. The set-up was used by a group of 4 students in any given session, and the organization of the Laboratory Experiment described in the main text (Experimental Overview) allowed for using only one set-up for the entire class. The set-up consists of a fully transparent chamber made from ½" polycarbonate panels, a projectile launcher (Vanier Project Launcher; Vernier Software and Technology, LLC), and a photodetector (APD120A Avalanche Photodetector; Thorlabs, Inc.). The samples for mechanoluminescence experiment were prepared by pressing clear packing tape against the powdered phosphor, removing any excess powder, and affixing it to the surface of the polycarbonate chamber facing the launcher. A ~20 g stainless steel ball bearing was fired at the sample target using the projectile launcher with exit velocities ranging from 4 to 6.5 m/s. The luminescence of the

samples was measured by students using the avalanche photodetector mounted behind the target and connected to an oscilloscope set in the roll mode. Only the first maximum was recorded, as rebounding of the ball bearings after the initial impact sometimes caused erratic results.

Instructors could evaluate students' work by allowing them to create a calibration curve for the mechanoluminescence intensity vs projectile velocity for their samples, within the linear range of the detector (in our case above 3 m/s). After the students collect at least 4 data points for calibration, the instructor should set the launch velocity and record it without telling the students. Students should then use the signal from this trial to determine the launch velocity according to their calibration.

Safety Notes

Tube Furnace. Even when wearing protective heat resistant gloves, students should never touch any part that has been heated (*i.e.*, the ceramic insulation, heating elements, and middle of fused silica tube).

High Pressure Hydrogen Gas Cylinder. An appropriate low-flow gas regulator should be attached to the hydrogen gas cylinder to prevent over pressurizing of the lines. After the instructor sets up the appropriate level of gas flow on the regulator, students should not touch the regulator any more. Ideally, permanent copper piping, tested for leaks prior to use, should be used to transport the hydrogen gas to the tube furnace.

Notes on the Spectroscopy Selection Rules

This Laboratory Experiment provides an opportunity to teach or revisit fundamental spectroscopic principles, particularly spectroscopy selection rules, and the origin of long-lifetime emission (phosphorescence) and luminescence intensity in different materials. The students who have taken a quantum mechanics or a spectroscopy course would likely associate

137

phosphorescence with spin-forbidden transitions arising from the change in spin multiplicity, or intersystem crossing, in luminescent molecules or complexes (see ref. 4 in the main text). However, in solid-state inorganic phosphors the long-lifetime emission does not generally involve the change from the single to the triplet state, but rather trapping of charge carriers in defect electronic states and their delayed release, as discussed in Chapter 5 and illustrated in Figure 5.1 (right panel). This Laboratory Experiment can be used by instructors to practically demonstrate the difference between these two distinct mechanisms that have very similar manifestation.

Another important spectroscopy selection rule applicable to this experiment is parity or Laporte selection rule. This selection rule defines the change in parity that accompanies an electronic transition. Specifically, Laporte selection rule states that electronic transitions that do not change the parity (gerade (even) to gerade; g↔g) or ungerade (odd) to ungerade; u↔u) are formally forbidden. As a well-know and often cited example in inorganic coordination chemistry, d-d ligand field transitions in ideally centrosymmetric complexes of transition metal ions are g↔g, and thus parity-forbidden. In this Laboratory experiment, Laporte rule is evident by comparing the photoluminescence intensity of Eu^{2+} and Eu^{3+} in $SrAl_2O_4$:Eu,Dy. For crude samples, only a week red emission characteristic for Eu^{3+} is observed arising from f-f transitions which are inherently Laporte forbidden. Upon annealing the samples in hydrogen, Eu^{3+} is reduced to Eu^{2+} resulting in intense Eu^{2+} emission involving d-f transitions (g↔u). This aspect of the experiment can be an excellent teaching opportunity to visually demonstrate Laporte selection rule and establish a connection with students' previously acquired knowledge.

Additional Notes

This Laboratory Experiments is highly flexible and can be adjusted to emphasize different topics depending on the type of the program (chemistry, physics, materials science, nanotechnology etc.), specific goals of the instructor, and available laboratory time. For instance, for solid-state inorganic chemistry or materials science labs, more time could be spent on sample preparation and processing, and measuring luminescence properties for different preparation conditions and annealing temperatures; for physical chemistry or physics labs, the emphasis

could be on spectroscopic principles and selection rules; for nanotechnology or engineering labs attention could be focused on the application of thermoluminescence and/or mechanoluminescence.